NOTE TO USERS

Page(s) missing in number only; text follows. Page(s) were scanned as received.

Pg. 142

This reproduction is the best copy available.

UMI®

DISSERTATION

STUDY OF CARRIER AND GAIN DYNAMICS IN InGaAsN QUANTUM WELL LASERS

Submitted by

Lifang Xu

Department of Electrical & Computer Engineering

In partial fulfillment of the requirements

For the Degree of Doctor of Philosophy

Colorado State University

Fort Collins, Colorado

Spring 2007

COLORADO STATE UNIVERSITY

April 2, 2007

WE HEREBY RECOMMEND THAT THE DISSERTATION PREPARED UNDER OUR SUPERVISION BY LIFANG XU ENTITLED "STUDY OF CARRIER AND GAIN DYNAMICS IN INGAASN QUANTUM WELL LASERS" BE ACCEPTED AS FULFILLING IN PART REQUIREMENTS FOR THE DEGREE OF DOCTOR OF PHILOSOPHY.

Committee on Graduate Work

Advisor

Co-Advisor

Department Head

ABSTRACT OF DISSERTATION

STUDY OF CARRIER AND GAIN DYNAMICS IN InGaAsN QUANTUM WELL LASERS

The goal of this dissertation is to unveil the role of nitrogen incorporation on important processes that shape the high-speed device performance of InGaAsN laser diodes. This is done through the investigation of the carrier recombination dynamics, nonlinear gain dynamics and carrier capture and escape processes in InGaAsN quantum well lasers. The carrier dynamics is investigated through a comprehensive temperature dependent steady state photoluminescence (PL) and time evolution of PL spectra. The gain dynamics is obtained from the analysis of ultrafast pump-probe transmission measurement with selective pump and probe wavelengths. The experiments are complemented with theoretical model simulations of the gain spectra.

The analysis of the steady state and time dependent PL measurements provided insightful understanding on the effect of nitrogen incorporation on the conduction band effective mass, the electronic structure of the quantum well and the main carrier recombination channels. A detailed lineshape analysis of the temperature dependent PL spectra was carried out. The analysis extracts the binding energy of the e_1-hh_1 ground-state exciton which equals 10±1 meV and 18±1 meV for InGaAs and InGaAsN (N=0.5%) single QW sample, respectively. By using a fractional dimension exciton binding energy model, an electron effective mass of $m_e^*=(0.11\pm0.015)m_0$ is determined for the highly strained $In_{0.4}Ga_{0.6}As_{0.995}N_{0.005}$/GaAs QW. We show by simulation of the gain model analysis that the enhanced m_e^* increases the transparency carrier density. It

also affects the differential gain dG/dN through the Fermi factor and the momentum matrix element. The former leads to an increase in dG/dN while the latter to a decrease.

From the time evolution of the PL, two recombination channels are present at early stages of carrier recombination. These two transitions are identified as the first quantized electron state to heavy-hole state (e1-hh1) and electron to light-hole state (e1-lh1) from the analysis of polarized photocurrent measurements. At longer time delays, the dilute nitride QW exhibits carrier localization at low temperatures and dominant nonradiative recombination at higher temperatures. This behavior contrast with that of the host matrix InGaAs in which the carrier lifetime behavior indicates radiative recombination dominates.

Through single color pump-probe experiments, carrier heating, two photon absorption (TPA) are found to be the two main factors contributing processes to the nonlinear gain compression. In InGaAsN laser carrier heating has more significant effect on gain compression in the gain regime. The relaxation time constant associated with carrier heating in both InGaAs and InGaAsN lasers have similar values, 2-3 ps.

The carrier escape times τ_{esc} is for the first time measured. τ_{esc} is dominant by hole escape and is about an order of magnitude smaller in InGaAsN than in InGaAs laser device. We show that the dependence of τ_{esc} on carrier density in dilute nitrides is only explained if tunneling through the triangular biased quantum well is considered. This mechanism is most important at low carrier densities. Exciton effects are also proven to be important in affecting the escape time. Together with time-resolved photoluminescence measurements, the carrier transport is found to be dominant over the

carrier capture process and no significant change has been found for both InGaAs and InGaAsN lasers. These experimental values allow us to understand the impact of nitrogen incorporation on the high-frequency modulation and bandwidth limitations of InGaAsN quantum-well lasers.

Lifang Xu
Department of Electrical & Computer Engineering
Colorado State University
Fort Collins, CO 80523
Spring 2007

ACKNOWLEDGMENTS

I am so thankful for many individuals that help me reach this point in my life.

First I would like to thank my advisor, Professor Carmen Menoni, for giving me the opportunity to involve with this interesting dissertation topics. Very importantly, she served as a great mentor and friend both inside and outside of the lab.

Sincere appreciation is extended to all my committee members, Professors James Sites, Mario C. Marconi, Randy Bartels and Jon M. Pikal (University of Wyoming). In addition to serving on my committee, they have provided insightful and constructive suggestions along the path to this point.

I would like to thank Dr. Jeng-Ya Yeh and Professor Luke Mawst, from University of Wisconsin-Madison, and Professor Nelson Tansu from Lehigh University, for providing the test lasers, which are very important in my research.

Among my coworkers in my lab, I can hardly give enough thanks to Dr. Dinesh Patel, whom I have had countless fruitful discussion with and a lot help in sample preparation, various experimental details to getting research results from. I am also grateful to have inherited the pioneering work in dilute nitride characterization, optical modulation and ultrafast laser alignment done by Dr. Ovidio Anton and Dr. Georgiy Vaschenko. Discussion and insightful suggestions from them are greatly appreciated.

I am also grateful to my lab neighbor, the EUV group, from where I have gained constructive suggestions, borrowed equipments and shared the enjoyable and friendly atmosphere. I thank Professor Mario Marconi for sharing his experience in ultrafast

pump-probe experiments. I appreciate the discussion on ultrafast phenomena with professor Randy Bartels and Klaus Hartinger. Gratitude is extended to Dr. Yong Wang and Dr. Brad Luther for their help with Ti-sapphire reconstruction. Although I only acknowledge a few people here, I express my greatest appreciation to all who have helped me along the way to get to this point.

Finally my deepest affection and gratitude are due to my family members including my parents, sister, my husband Qinglin Zeng and my son Forrest, ziyan, Zeng. Their love is the best support for me to finish study here.

This dissertation is dedicated to my father, Shihua Xu.

TABLE OF CONTENTS

LIST OF TABLES

LIST OF FIGURES

CHAPTER 1

Introduction

In this chapter, the advantage of the InGaAsN semiconductor alloys that offer a new platform for the fabrication of 1.3 μm lasers on GaAs substrates is presented. This is followed by a discussion of "state of the art" growth and research on InGaAsN QW lasers. Challenges and remaining work to tame this material system to realize the full wavelength range of high performance lasers is the motivation of this thesis and will be stated. Finally, the structure of this dissertation is introduced.

1.1 1.3 and 1.55 μm laser diode Technology

With the incredible growth of the internet and data transmission, the requirement of high bandwidth for fiber networks has increased at an unprecedented pace. Low cost, long wavelength (1.3 and 1.55 μm), single mode vertical cavity surface-emitting lasers (VCSELs), which can be directly modulated, operated uncooled in ambient environments, and easily packaged and coupled to fibre, are essential elements to enable this optical revolution.

GaAs-based GaAs/AlGaAs pairs possess the highest index of refraction contrast, thus providing the most efficient Distributed Bragg Reflector (DBR) for VCSEL growth. However, conventional GaAs based system like InGaAs/GaAs, even at the highest strain limit, only allow the device to operate at the wavelengths out to about 1.2 μm [1, 2]. In contrast, InP based devices can easily operate within the desired wavelength window, unfortunately the realization of InP-VCSELs devices emitting at 1.3 or 1.55 μm are suffering from severe technological problems. This is because the index of refraction contrast of InP/InGaAsP is very small. Many layers are therefore required to produce a high-reflectivity InP-based DBR which is a growth challenge and further more introduces high series resistance, retarding the device dynamics [1, 3]. In addition, thermal issues are particularly a problem especially for InGaAsP/InP system [4] because of the high temperature sensitivity of the threshold current that results from the small conduction band offset and associated carrier leakage.

All these problems raise the demand for an alternative material system for long wavelength laser diodes. The most promising approach is thus to use active

materials which can be grown on a GaAs substrate and emit at 1.3 or 1.55μm. The search for new options in recent years have included InAs quantum-dot (QD) active regions [5-8] , GaAsSb/InGaAs type II quantum wells [9,10], as well as the InGaAsN/GaAs QW lasers. The latter are the main subject of this thesis, specifically, strain compensated high indium content dilute nitride lasers with emission wavelengths of 1.3 μm [11]. Despite recent laser successes, there is still very significant work remaining to tame this material system to realize the full wavelength range of high-performance edge emitting lasers and VCSELs.

1.2 InGaAsN compounds and band structure

Ever since InGaAsN/GaAs was introduced as a promising candidate to replace conventional InGaAsP/InP material as a long-wavelength laser emitter and detector in optical networks, it has continued to attract research interest from the semiconductor community. Contrary to the general rules of III–V alloy semiconductors where a smaller lattice constant increases the bandgap, the large electronegativity of N and its small covalent radius cause a very strong negative bowing parameter and the addition of N to GaAs or InGaAs dramatically decreases the bandgap [4,12], as shown in Figure 1.1. By combining N and In, InGaAsN produces a very rapid decrease in bandgap to reach the long-wavelength emission region with simultaneous control over bandgap and lattice match to GaAs. Such an active quantum-well material allows the fabrication of 1.3 μm

lasers, particularly VCSELs, by combining a 1.3 μm QW active region with the well-developed AlGaAs/GaAs DBR mirror technology.

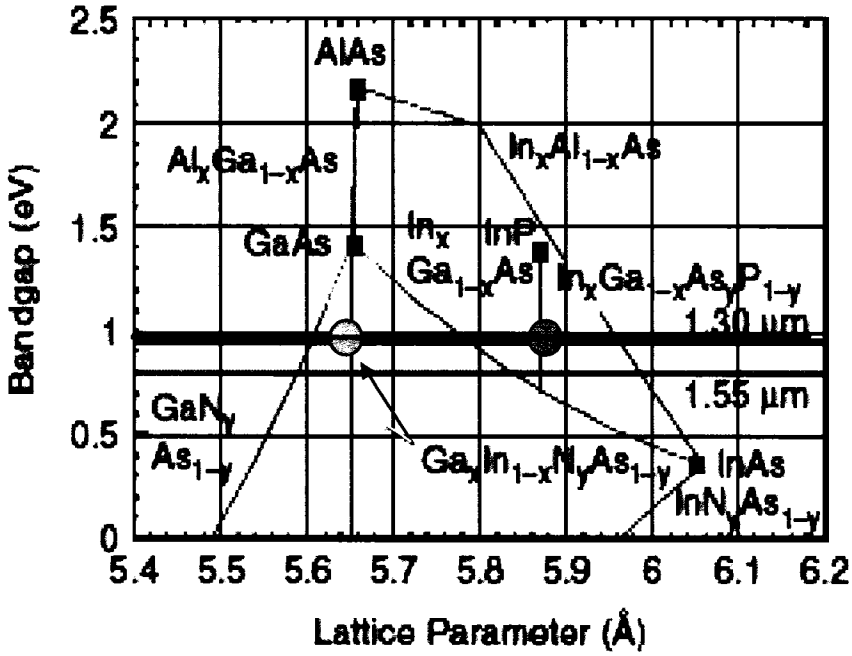

Figure 1.1 - Bandgap versus lattice constant for III-V alloys showing lines for the condition of lattice match to GaAs for Nitride-Arsenide alloys and to InP for Arsenide-Phosphide alloys in the region applicable to long-wavelength fibre system.

The most widely accepted explanation for the bandgap bowing effect has been the band-anticrossing model [12]. In this model, the reduction in the energy gap is due to the band interaction between the conduction band edge E_M and the band of nitrogen resonant defect states E_N, which lies above the conduction band

edge and remains constant. The full Hamiltonian for this mechanism can be expressed as:

$$H = \begin{pmatrix} E_M(k) & V_{MN} \\ V_{MN} & E_N \end{pmatrix} \tag{1.1}$$

In Eq.(1.1) the matrix element V_{MN} describes the coupling strength between E_M and E_N and has been found to increase with nitrogen composition x as $V_{MN} = \beta\sqrt{x}$; β is a constant reported to vary from 1.6 to 3.0, although still needs to be confirmed by experiments [13-15].

The dispersion curve of the conduction band can be solved by extracting the eigenvalue of the Hamiltonian above. This gives two possible solutions, E_+ and E-, manifested as a splitting of the conduction band into two distinct bands. E- is regarded as the new conduction band. Figure 1.2 plots a typical dilute nitride conduction band structure using the band anti-crossing approach, with parabolic assumption for E_M.

$$\begin{vmatrix} E - E_M(k) & V_{MN} \\ V_{MN} & E - E_N \end{vmatrix} = 0 \tag{1.2}$$

$$E_{\pm}(k) = \frac{E_N + E_M(k) \pm \sqrt{(E_N - E_M(k))^2 + 4V^2{}_{MN}}}{2} \tag{1.3}$$

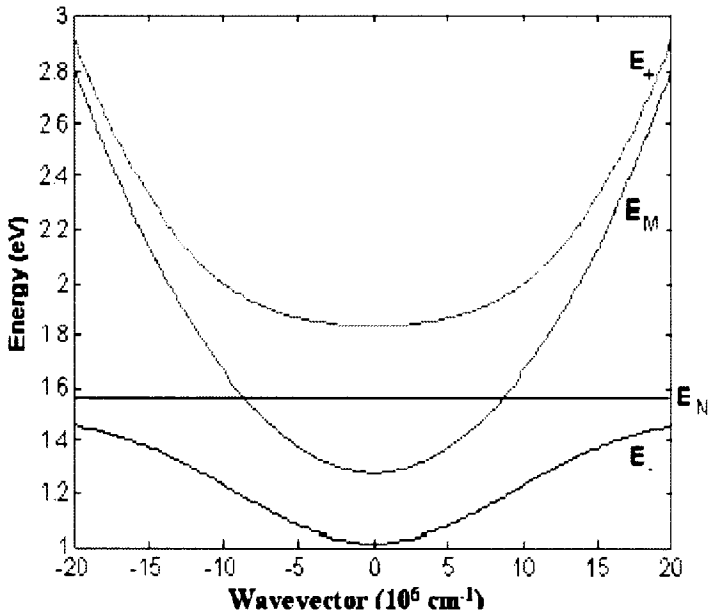

Figure 1. 2 E-k dispersion diagram of dilute nitride calculated using band anti-crossing model, with parabolic assumption.

The band anti-crossing and the parabolic assumption for the conduction band structure mentioned above are an oversimplied theory. More generally, the band structure of InGaAsN QW is obtained using a 10 band k*p simulation, where the interaction between all the energy levels: Nitrogen induced level E_N, conduction band (CB), Heavy hole (HH), Light hole (LH) and spin-orbit spit-off (SO), are considered. In this model, the Hamiltonian can be written as [16]:

$H_{\text{upper triangle}}=$

$$\begin{pmatrix} E_N & V_{Nc} & -\sqrt{3}T_{N+} & \sqrt{2}U_N & -U_N & 0 & 0 & 0 & -T_{N-} & -\sqrt{2}T_{N-} \\ & E_{CB} & -\sqrt{3}T_{+} & \sqrt{2}U & -U & 0 & 0 & 0 & -T_{-} & -\sqrt{2}T_{-} \\ & & E_{HH} & \sqrt{2}S & -S & 0 & 0 & 0 & -R & -\sqrt{2}R \\ & & & E_{LH} & Q & T_{N+}^{*} & T_{+}^{*} & R & 0 & \sqrt{3}S \\ & & & & E_{SO} & \sqrt{2}T_{N+}^{*} & \sqrt{2}T_{+}^{*} & \sqrt{2}R & -\sqrt{3}S & 0 \\ & & & & & E_N & V_{Nc} & -\sqrt{3}T_{N-} & \sqrt{2}U_N & -U_N \\ & & & & & & E_{CB} & -\sqrt{3}T_{-} & \sqrt{2}U & -U \\ & & & & & & & E_{HH} & \sqrt{2}S^{*} & -S^{*} \\ & & & & & & & & E_{LH} & Q \\ & & & & & & & & & E_{SO} \end{pmatrix} \quad (1.4)$$

Here the nondiangonal matrix elements denote the interaction between the bands, which give rise to the conduction band bowing for the dilute nitride material and the valence mixing effect.

Thus the band dispersion structure can be solved from the Schrödinger equation regarding this Hamiltonian:

$$\sum_{\upsilon\upsilon'}\left[H_{\upsilon\upsilon'}(k_{//},-i\frac{\partial}{\partial z})+V(z)\delta_{\upsilon\upsilon'}\right]G_m^{\upsilon'}(k_{//},z) = E_m G_m^{\upsilon}(k_{//},z), \quad (1.5)$$

Where $G_m^{\nu}(k//,z)$ is the envelope of the corresponding eigenfunctions.

Figure 1.3 plots the calculated energy dispersion curve with the k*p simulation, for a 1.7% nitrogen content InGaAsN/GaAs single QW. For comparison, the calculation result on a identical nitrogen free QW is also shown.

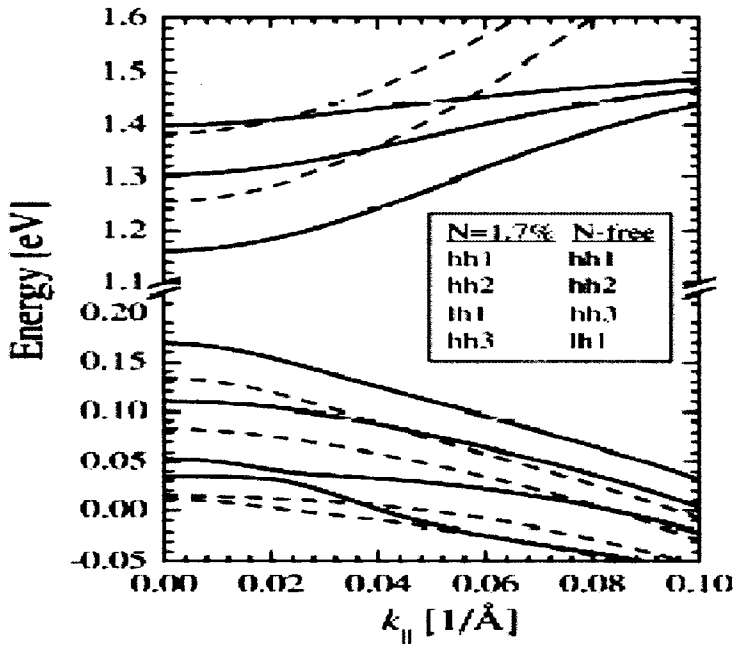

Figure 1. 3 Calculated energy dispersion curve of $In_{0.36}Ga_{0.64}As_{0.983}N_{0.017}$/GaAs SQW laser device based on 10 band k*p simulation. The same calculation is also performed on nitrogen free sample as comparison. [16]

From Figure 1.2 and 1.3, both the band-anticrossing model with parabolic assumption and the k*p simulation predict a strong influence of nitrogen on the band gap reduction, associated with an enhanced electron effective mass m_e*. The increase in m_e* is associated with an improvement of the temperature characteristic of the long-wavelength laser diodes, as compared with conventional InP-based QW laser structures. The impact of the increased m_e* on the high speed modulation bandwidth of laser diode is still under argument [16, 17].

These models provide the framework to calculate the electronic structure of QWs based on InGaAsN. In this case the most common barrier material is GaAs. For InGaAsN/GaAs the conduction band and valence band offset have yet

not been experimentally determined. But the most accepted values are 80/20, which contrast with 60/40 for the nitrogen free InGaAs/GaAs Qws.

1.3 InGaAsN/GaAs lasers: State of the Art

The above discussion on InGaAsN/GaAs QW structures highlights the factors that could prove decisive in the race to produce low cost, long wavelength VCSELs. In comparison with InP alloys of the same bandgap, the conduction band well is deeper and the electron effective mass is larger in InGaAsN, thus providing better confinement for electrons and better match of the valence and conduction-band densities of states. This can lead to a higher T_0, higher operating temperature, higher efficiency and higher output power. Second, most of the energy band engineering used to minimize heterojunction voltage drops use intermediate graded layers of AlxGa(1−x)As or AlAs/GaAs superlattices, all of which are lattice matched to GaAs and do not require difficult compositional control over both column III and column V constituents in a quaternary layer, such as InGaAsP, to maintain lattice match. Third, VCSELs can be straightforwardly fabricated using the well-developed GaAs/AlAs mirror and AlAs oxidation for current and optical aperture confinement technologies. Fourth, InGaAsN on GaAs provides easy monolithic integration with GaAs high-speed electronics that will be essential to provide low-cost, high-speed integrated electrical drivers for direct laser modulation in high-speed networks. In spite of all these advantages of the InGaAsN/GaAs system, there are still very significant

challenges for InGaAsN to produce useful, reliable lasers at 1.3 and 1.55 μm. One of the major challenges comes from the epitaxial growth techniques.

1.3.1 Epitaxial growth techniques

Both molecular beam epitaxy (MBE) [18-22] and metal organic chemical vapor deposition (MOCVD) [11, 23-25] have been used to grow InGaAsN quantum wells. Although compositional control and uniformity of InGaAsN grown by MBE is relatively easier compared to MOCVD, MOCVD is still the preferred growth technology as it can be readily adapted to current commercial optoelectronic epitaxial technology for both GaAs-based VCSELs and InP-based edge-emitting lasers. However, a great challenge exists in the growth of InGaAsN by MOCVD compared to the GaAs and InP-based systems. This is due to the different basic crystal structures of the constituent alloys and their regions of growth compatibility: InGaN is a hexagonal (wurtzite) crystal grown at relatively high temperatures while InGaAs is cubic (zincblende) grown at relatively low temperatures, creating a miscibility gap in the alloys. Thus in order to incorporate sufficient N, the growth has to be done at much lower growth temperatures and under metastable growth conditions within the miscibility gap region of the InGaAsN alloy.

In spite of much effort on the growth conditions and after-growth treatments [26], InGaAsN lasers have suffered from what has been dubbed as the

"nitrogen penalty," with high threshold currents and low efficiency as the content of nitrogen in the semiconductor is increased.

1.3.2 Threshold current, temperature sensitivity and optical quality

As mentioned in section 1.1, a low threshold current, I_{th}, and low temperature sensitivity of I_{th} are the most essential elements of a laser diode's characteristics. Materials with good optical qualities are the basic requirement to realize such high performance laser devices. Ever since InGaAsN has been introduced as a promising candidate for long wavelength operation, a great deal of research work has been devoted to study this alloy system and to understand the effect of nitrogen incorporation on defects, band structure, carrier localization, and the resulted optical quality and device performance [12, 27-39]. Generally it has been found that the incorporation of nitrogen tends to introduce large number of non-radiative centers, thus it deteriorates the optical efficiency. However, it has been difficult to obtain reliable data on the fundamental properties of InGaAsN SQW.

Recently high-performance 1.3μm InGaAsN QW lasers with very low threshold current density have been realized [11, 22, 23, and 25] both by MOCVD and MBE, by utilizing strain compensation techniques. In this band engineering approach, strain compensation layers with higher band gap are inserted close to the single QW. This approach can enhance device performance by allowing higher indium concentration to the strain limit (for longer wavelength) and

minimum nitrogen concentration (for improving luminescence efficiency) to be used in the QW active region. The utilization of larger band gap barrier materials can also lead to a suppression of thermionic carrier leakage, which in turn leads to a reduction in the temperature sensitivity of the threshold-current density of the lasers, in particular, at high temperature operation [11]. Tensile strain in the form of a GaAsP layer placed 10 nm away from InGaAsN QW also reduces the overall stress of the active region (strain compensation). Therefore, stress-related defects can be reduced in the active region.

The characteristic temperature (T_0), which is defined as:

$$I_{th} = I_0 \cdot e^{T/T_0} \tag{1.6}$$

has been determined to be in the range of 70-110 K for high-performance 1.3-μm InGaAsN single-QW (SQW) lasers[41,42], which is much lower than that of optimized 1200 nm InGaAs SQW lasers, ~200 K [43], as well as the T_0 predicted by theory [4]. But these are speculations as there is still many unknowns in the material's fundamental physical parameters of the high indium content InGaAsN are virtually unknown. To date no direct determination of the electron effective mass, m_e^*, has been reported for high indium content (~30%-40%) $In_xGa_{1-x}As_yN_{1-y}$-, due to the limitations imposed by the high strain in growing thick freestanding epilayers (typically ~1-3 μm) or QWs with different thickness. In addition, it is also debated in theoretical models on how the increase in m_e^* after incorporation of nitrogen affects the performance of the laser diodes, especially in the prediction

of the intrinsic differential peak gain dG/dN_w, which affects the modulation speed for the laser diode. More discussion about the high speed modulation characteristics follows in next section. Answering these open questions is one of the objectives in this dissertation.

1.3.3 High speed modulation

Besides the requirement for small threshold current and low temperature sensitivity, the high-speed modulation properties are also essential for laser diode applications in communications. The relaxation oscillation resonance frequency f_R and associated damping mechanisms are of paramount importance in that they set the intrinsic limit to laser diode's performance under modulation. While the actual modulation response of a laser device can be seriously degraded by electrical parasitics associated with the package and chip, it usually can be overcome with changing the package design. However, damping due to nonlinear gain can not be altered because it is material dependent. Meanwhile, differential gain dg/dN, which directly determines f_R, is also laser structure and material dependant, as it is affected by the ratio of carrier capture and escape processes $R = \tau_{cap} / \tau_{esp}$ [44].

Although high performance InGaAsN/GaAs QW lasers have been demonstrated with high speed modulation bandwidth [45], there are still distance away from the high frequency bandwidth limit of the device that theories predict [12][39]. A few experimental works have been found in studying the intrinsic modulation response of dilute nitride laser [49][50], and it was pointed out that

the bandwidth of current dilute nitride lasers is mainly limited by thermal effects which reduce the effective differential gain and cause a rapid increase of the threshold current. In addition, supportive theoretical calculations of carrier thermionic escape have suggested the existence of an increased hole leakage attributing to the thermal problem [51]. However, further direct experimental evidence is needed, which is very important because the model calculation itself relies on the assumption of a smaller hole confinement in the InGaAsN QW lasers, an issue that is still relatively controversial.

1.4 Motivation and structure of the dissertation

The motivation of this work is to study fundamental optical material properties of strain compensated InGaAsN quantum wells. More specifically, we are thriving to answer the following open questions:

(a) What processes affects the optical efficiency of InGaAsN QWs?

(b) What is the value of m_e^* and how it changes after incorporation of nitrogen and how it influences the performance of laser diodes?

(c) What is the carrier dynamics behavior, specifically nonlinear carrier heating and its relaxation, carrier capture into and escape out of the well and how these processes affect the nonlinear gain dynamics.

To answer (a) and (b), steady state photoluminescence (PL) spectroscopy and the time evolution of the PL are utilized to investigate the carrier recombination dynamics and its influence on optical quality of InGaAsN Qws. A

line shape analysis of the temperature dependent PL spectra provides a way to extract the value of m_e^* in the highly strained InGaAsN QW. Different ultrafast pump-probe techniques are employed to investigate nonlinear gain dynamics and carrier capture and escape processes. The corresponding time constants are extracted from the experimental measurements. Theoretically, a gain model is constructed to help find the current-carrier density (I-N) relationship by fitting the measured gain spectra, in order to investigate the influence of nitrogen incorporation on gain, differential gain and transparency carrier density of the InGaAsN QW devices. All the experiments and the theoretical analysis are carried out on two identical device structures that only differ in the nitrogen content in the single QW active region. The effects of nitrogen are extracted by comparison between them.

The structure of this dissertation is organized as follows:

In the next chapter (chapter 2), the materials and experimental methods used in this work are described. Chapter 3 presents the gain model based on the parabolic assumption. The temperature behavior of dg/dN_w and N_{tr} are retrieved, and the effects of exciton and enhanced m_e^* on gain and differential gain are predicted. The validity of this model is proved by testing against published k*p simulation results.

Chapter 4 presents the results of steady state and time resolved photoluminescence measurements. First the fundamental physical parameter m_e^* is extracted from the temperature dependent photoluminescence spectra at low excitation intensity. At high excitation intensity, two emission features are

observed in the PL spectra, and are characterized through polarization dependent photocurrent (PC) measurements. The impact of the additional emission at higher energy on carrier recombination dynamics is assessed through time resolved PL measurements. The influence of carrier localization and nonradiative recombination as function of temperature are also investigated.

Chapter 5 presents the results of a study of the nonlinear gain dynamics and measure of the carrier capture and escape time (τ_{cap} and τ_{esp}) versus injection conditions by employing ultrafast pump-probe transmission measurements. Both studies are of paramount importance to analyze the high speed potential of 1.3 μm InGaAsN/GaAs QW laser diodes. A theoretical model with consideration of band offset ratio, exciton and carrier tunneling effects are also discussed and used to explain the observed capture and escape time processes.

At the end of this dissertation (chapter 6), a summary of the results and guideline for future work are presented,

Reference:

[1]. K. Czotscher, E. C. Larkins, S. Weisser, W. Benz, J. Daleiden, J. Fleissner, M. Maier, J. D. Ralston, and J. Rosenzweig, "Uncooled high-temperature (130 degree C) operation of InGaAs-GaAs multiple quantum-well lasers at 20 Gb/s," IEEE PHOTONICS TECHNOLOGY LETTERS **9**: 575-577 (1997) .

[2]. N. Tansu, Y. L. Chang, T. Takeuchi, D. P. Bour, S.W. Corzing, M. R. T. Tan and L. J. Mawst, "Temperature analysis and characteristics of highly strained InGaAs-GaAsP-GaAs (lambda > 1.17 μm) quantum-well lasers", IEEE JOURNAL OF QUANTUM ELECTRONICS 38: 640-651 (2002) .

[3]. F.S.Choa, K.Tai, W.T.Tsang, SNG Chu, "High reflectivity 1.55μm InP/InGaAsP Bragg mirror grown by chemical beam epitaxy", APPLIED PHYSICS LETTERS 59 (22): 2820-2822 NOV 25 (1991).

[4]. M. Kondow, K.Uomi, A.Niwa, T.Kitatani, S.Watahiki, Y.Yazawa, " GaInNAs: A novel material for long-wavelength-range laser diodes with excellent high-temperature performance", JAPANESE JOURNAL OF APPLIED PHYSICS PART 1-REGULAR PAPERS SHORT NOTES & REVIEW PAPERS 35 (2B): 1273-1275 FEB (1996).

[5]. V.M.Ustinov, N.A.Maleev, A.E.Zhukov, etc. "InAs/InGaAs quantum dot structures on GaAs substrates emitting at 1.3 μm", APPLIED PHYSICS LETTERS 74 (19): 2815-2817 MAY 10 (1999).

[6]. K. Otsubo, N. Hatori, M. Ishida, S. Okumura, T. Akiyama, Y. Nakata, H. Ebe, M. Sugawara, and Y. Arakawa, "Temperature-insensitive eye-opening under 10-Gb/s modulation of 1.3-mu m p-doped quantum-dot lasers without current adjustments", JAPANESE JOURNAL OF APPLIED PHYSICS PART 2-LETTERS &EXPRRESS LETTERS **43:** L1124-L1126 (2004).

[7]. A. Salhi, L. Martiradonna, G. Visimberga, V. Tasco, L. Fortunato, M. T. Todaro, R. Cingolani, A. Passaseo, M. De Vittorio, "High-modal gain 1300-nm In(Ga)As-GaAs quantum-dot lasers", IEEE PHOTONICS TECHNOLOGY LETTERS **18** (13-16): 1735-1737 (2006).

[8]. H. Y. Liu, S. L. Liew, T. Badcock, D. J. Mowbray, M. S. Skolnick, S. K. Ray, T. L. Choi, K. M. Groom, B. Stevens, F. Hasbullah, C. Y. Jin, M. Hopkinson, and R. A. Hogg, "p-doped 1.3 μm InAs/GaAs quantum-dot laser with a low threshold current density and high differential efficiency", APPLIED PHYSICS LETTERS **89** (7): Art. No. 073113 (2006).

[9]. O.Blum, J.F.Klem, "Characteristics of GaAsSb single-quantum-well-lasers emitting near 1.3 μm", IEEE PHOTONICS TECHNOLOGY LETTERS **12** (7): 771-773 JUL (2000);

[10]. M. S.Noh, R. D. Dupuis, D. P. Bour, G. Walter and N.Holonyak, "Long-wavelength strain-compensated GaAsSb quantum-well heterostructures laser

grown by metalorganic chemical vapor deposition" APPLIED PHYSICS LETTERS **83** (13): 2530-2532 (2003).

[11]. N. Tansu, N.J.Kirsch, L.J. Mawst "Low-threshold-current-density 1300-nm dilute-nitride quantum well lasers," APPLIED PHYSICS LETTERS **81** (14): 2523-2525 SEP 30 (2002).

[12]. W.Shan, W.Walukiewicz, J.W.Ager etc. "Band anticrossing in GaInNAs alloys", PHYSICAL REVIEW LETTERS **82** (6): 1221-1224 FEB 8 (1999).

[13]. S.A.Choulis, S.Tomic, E.P.O'Reilly, TJC.Hosea, "Determining the band-structure of an InGaNAs/GaAs semiconductor laser structure using non-destructive photomodulated reflectance measurements and k center dot p studies", SOLID STATE COMMUNICATIONS **125** (3-4): 155-159 JAN (2003).

[14]. P.Perlin, P. Wisniewski, C.Skierbiszewski, T.Suski, etc, "Interband optical absorption in free standing layer of $Ga_{0.96}In_{0.04}As_{0.99}N_{0.01}$" APPLIED PHYSICS LETTERS **76** (10): 1279-1281 MAR 6 (2000).

[15]. I.Suemune, K.Uesugi, W.Walukiewicz, "Role of nitrogen in the reduced temperature dependence of band-gap energy in GaNAs", APPLIED PHYSICS LETTERS **77** (19): 3021-3023 NOV 6 (2000).

[16]. S.Tomic, E.P.O'Reilly, R.Feshe, etc. "Theoretical and experimental analysis of 1.3μm InGaAsN/GaAs Lasers", IEEE JOURNAL OF SELECTED TOPICS IN QUANTUM ELECTRONICS **9**(5): (2003).

[17]. S. T. Ng, W. J. Fan, Y. X. Dang, and S. F. Yoon, " Comparison of electronic band structure and optical transparency conditions of InxGa1-xAs1-yNy/GaAs quantum wells calculated by 10-band, 8-band, and 6-band k center dot p models", PHYSICAL REVIEW B **72** (11): 115341 (2005).

[18]. D.A.Livshits, A.Y.Egorov, H.Riechert, "8W continuous wave operation of InGaAsN lasers at 1.3 mu m", ELECTRONICS LETTERS **36** (16): 1381-1382 AUG 3 (2000);

[19]. C.S.Peng, T. Jouhti, P.Laukkanen, etc, "1.32-μm GaInNAs-GaAs laser with a low threshold current density", IEEE PHOTONICS TECHNOLOGY LETTERS **14** (3): 275-277 MAR (2002);

[20]. S.Sato, "Low threshold and high characteristic temperature 1.3 μm range GaInNAs lasers grown by metalorganic chemical vapor deposition", JAPANESE JOURNAL OF APPLIED PHYSICS PART 1-REGULAR PAPERS SHORT NOTES & REVIEW PAPERS **39** (6A): 3403-3405 JUN (2000);

[21]. V. Gambin, W. Ha, M. Wistey, H. Yuen, S.R. Bank, S.M. Kim, J.S. Harris, "GaInNAsSb for 1.3-1.6-μm-long wavelength lasers grown by molecular beam epitaxy", IEEE JOURNAL OF SELECTED TOPICS IN QUANTUM ELECTRONICS **8** (4): 795-800 (2002);

[22]. M. Hopkinson, C. Y. Jin, H. Y. Liu and R. Airey, " 1.34 μm GaInNAs quantum well lasers with low room-temperature threshold current density", ELECTRONICS LETTERS **42** (16): 923-924 (2006).

[23]. J.Y. Yeh, N. Tansu, L.J. Mawst, "Long wavelength MOCVD grown InGaAsN-GaAsN quantum well lasers emitting at 1.378-1.41 μm," ELECTRONICS LETTERS **40** (12): 739-741 (2004).

[24]. T. Nishida, M. Takaya, S. Kakinuma and T. Kaneko, " 4.2-mW GaInNAs long-wavelength VCSEL grown by metalorganic chemical vapor deposition", IEEE JOURNAL OF SELECTED TOPICS IN QUANTUM ELECTRONICS **11** (5): 958-961 (2005).

[25]. M. Yamada, T. Anan, H. Hatakeyama, K. Tokutome, N. Suzuki, T. Nakamura, and K. Nishi, "Lowthreshold operation of 1.34-μm GaInNAs VCSEL grown by MOVPE" , IEEE PHOTONICS TECHNOLOGY LETTER **17:** 950-952 (2005)

[26]. T. Kageyama, T. Miyamoto, S. Makino, F. Koyama, and K. Iga, "Thermal annealing of GaInNAs/GaAs quantum wells grown by chemical beam epitaxy and its effect on photoluminescence." JAPANESE JOURNAL OF APPLIED PHYSICS 2, **38** (3B): 298 – 300 (1999)

[27]. T. Hakkarainen, J. Toivonen, H. Koskenvaara, M. Sopanen, H. Lipsanen, "Structural and optical properties of GaInNAs/GaAs quantum structures", JOURNAL OF PHYSICS-CONDENSED MATTER **16** (31): S3009-S3026 (2004).

[28]. R.A.Mair, J.Y.Lin and H.X.Jiang, "Time-resolved photoluminescence studies of InGaAsN", APPLIED PHYSICS LETTERS **76**(2): 188-190 (2000);

[29]. P.J.Klar, H.Gruning, L.Chen, T.Hartmann, etc, "Unusual properties of metastable (Ga,In)(N,As) containing semiconductor structures", IEE PROC.-OPTOELECTRONICS **150**(1):28-35 (2003);

[30]. N.Tansu, J.Y.Yeh and L.J.Mawst, "improved photoluminescence of InGaAsN-(In)GaAsP quantum well by organometallic vapor phase epitaxy using growth pause annealing", APPLIED PHYSICS LETTERS **82**(18):3008-3010 (2003);

[31]. Y.H.Cho, G.H.Gainer, A.J.Fischer and J.J.Song, " "S-shaped" temperature-dependent emission shift and carrier dynamics in InGaN/GaN multiple quantum wells", APPLIED PHYSICS LETTERS 73(10):1370-1372 (1998);

[32]. X.Yang, J.B.Heroux, M.J.Jurkovic and W.I.Wang, "Photoluminescence of as-grown and thermally annealed InGaAsN/GaAs quantum wells grown by molecular beam epitaxy", JOURNAL OF VACUUM SCIENCE & TECHNOLOGY **17**(3): 1144-1146 (1999);

[33]. F.I.Lai, S.Y.Kuo, J.S.Wang, H.C.Kuo, S.C.Wang, H.S.Wang, C.T.Liang, Y.F.Chen, "Effect of nitrogen contents on the temperature dependence of photoluminescence in InGaAsN/GaAs single quantum wells", JOURNAL OF

VACUUM SCIENCE & TECHNOLOGY A **24** (4): 1223-1227 JUL-AUG (2006)

[34]. R.Kudrawiec, G.Sek, K.Ryczko, J.Misiewicz, etc, "The nature of optical transition in $Ga_{0.64}In_{0.36}As_{1-x}N_x$/GaAs single quantum wells with low nitrogen content (x<0.008)", SOLID STATE COMMUNICATIONS 127: 613-618 (2003);

[35]. L.Grenouillet, C.Bru-Chevallier, and G.Guillot, "Evidence of strong carrier localization below 100K in a GaInNAs/GaAs single quantum well", APPLIED PHYSICS LETTERS 76(16): 2241-2243 (2000);

[36]. S.Tomic and E.P.O'Reilly, "Influence of confinement energy and band anticrossing effect on the electron effective mass in $Ga_{1-y}In_yN_xAs_{1-x}$ quantum wells", PHYSICAL REVIEW B 71(23): 233301 (2005);

[37]. Pan Z, Li LH, Lin YW, etc, "Conduction band offset and electron effective mass in GaInNAs/GaAs quantum-well structures with low nitrogen concentration", APPLIED PHYSICS LETTERS **78**(15):2217 (2001);

[38]. O. Anton, D. Patel, C. S. Menoni, J. Y. Yeh, L. Mawst, J. Pikal, and N. Tansu, "Increased monomolecular recombination in MOCVD grown 1.3μm InGaAsN/GaAsP/GaAs QW lasers from carrier lifetime measurements", IEEE PHOTONICS TECHNOLOGY LETTERS **17** (5): 953-955 MAY (2005);

[39]. JCL.Yong, J.M.Rorison, M.Othman, H.D. Sun, M.D.Dawson, K.A.Williams, "Simulation of gain and modulation bandwidths of 1300nm RWG InGaAsN lasers", IEE PROCEEDINGS-OPTOELECTRONICS **150** (1): 80-82 FEB (2003);

[40]. H. Carrère, X. Marie, J. Barrau, and T. Amand, "Comparison of the optical gain of InGaAsN quantum-well lasers with GaAs or GaAsP barriers," APPLIED PHYSICS LETTERS **86 :** 071116 (2005).

[41]. S.M. Wang, Y.Q. Wei, X.D. Wang, Q.X. Zhao, M. Sadeghi, and A.Larsson, "Very low threshold current density 1.3 μm GaInNAs single-quantum well lasers grown by molecular beam epitaxy," JOURNAL OF CRYSTAL GROWTH **278**: 734-738 (2005).

[42]. N. Tansu and L. J. Mawst, "Current injection efficiency of InGaAsN quantum-well lasers," JOURNAL OF APPLIED PHYSICS **97:** 054502 (2005).

[43]. N.Tansu, L.J.Mawst, "High-performance strain-compensated InGaAs-GaAsP-GaAs (lambda=1.17 μm) quantum-well diode lasers", IEEE PHOTONICS TECHNOLOGY LETTERS **13** (3): 179-181 MAR (2001).

[44]. L. A. Coldren and S. W. Corzine, *Diode lasers and Photonic Integrated Circuits*: Wiley series in microwave and optical engineering, (1995).

[45]. D. Gollub, S. Moses, and A. Forchel, "1.3 mu m double quantum well GaInNAs distributed feedback laser diode with 13.8 GHz small signal modulation bandwidth," ELECTRONICS LETTERS **40 :** 1181-1182 (2004).

[46]. J.S. Gustavsson, Y.Q. Wei, M. Sadeghi, S.M. Wang, and A. Larsson, "10 Gbit/s modulation of 1.3 μm GaInNAs lasers up to 110°C", ELECTRONICS LETTERS **42** (16): 925-926 (2006).

[47]. G.Steinle, F.Mederer, M.Kicherer, R.Michalzik, G.Kristen, "Data transmission up to 10Gbit/s with 1.3 μm wavelength InGaAsN VCSELs", ELECTRONICS LETTERS **37** (10): 632-634 MAY 10 (2001).

[48]. A.Martinez, J.G.Provost, B.Dagens, V. Sallet, etc, "9.7 GHz small-signal bandwidth of three-quantum well GaInNAs/GaAs laser diodes operating at 1.35 μm", ELECTRONICS LETTERS **40** (7): 425-427 APR (2004).

[49]. Y.Q.Wei, J.S. Gustavsson, A. Haglund, P. Modh, M. Sadeghi, S.M. Wang and A. Larsson, ' High-frequency modulation and bandwidth limitations of GaInNAs double-quantum-well lasers", APPLIED PHYSICS LETTERS **88** (5): Art. No. 051103 (2006)

[50]. O.Anton, L.F. Xu, D. Patel, C.S.Menoni, J.Y.Yeh, T.T.Van Roy, L.J. Mawst and N.Tansu, "The intrinsic frequency response of 1.3-μm InGaAsN lasers in the range T=10 degrees C-80 degrees C' IEEE PHOTONICS TECHNOLOGY LETTERS **18** (13-16): 1774-1776 (2006).

[51]. N. Tansu, L. J. Mawst, "The role of hole leakage in 1300-nm InGaAsN quantum-well lasers", APPLIED PHYSICS LETTERS **82** (10): 1500-1502 MAR (2003).

CHAPTER 2

Experimental Methods

In this chapter, detail descriptions of the experiments are presented. The investigated laser structure and lasing characteristics are introduced first in section 2.1. Continuous and time resolved photoluminescence (PL) measurements, which are aimed to understand how the electronic structure and the carrier recombination dynamics are impacted by nitrogen incorporation, are described in section 2.2. Polarization dependent photocurrent (PC), a complementary tool for analyzing the electronic structure are also introduced in the same section. The experimental set-ups for single and two color pump-probe transmission measurements, which are devoted to help understand the impact of nitrogen incorporation on the gain dynamics and on the transport processes, are described in section 2.3. In the last section, the amplified spontaneous emission (ASE) measurements are introduced. From these measurements the gain spectra is obtained at various injection conditions.

2.1 $InGaAs(N)_{0,\ 0.5\%}/GaAs$ Quantum Well structures: growth and operational characteristics

The experiments described in this dissertation were carried out in high compressively strained InGaAs(N) single QW laser structures and identical samples in which the top contact layer was removed. The laser diodes are grown on a GaAs substrate by low pressure (200 mbar) and low temperature (530 °C) metal-organic chemical vapor deposition (MOCVD), at University of Wisconsin at Madison by the group led by Dr. Luke. Mawst [1-4]. Figure 2.1 is a schematic diagram of the separate confinement heterostructure (SCH) single QW laser. The structure consists of a 6nm $In_{0.4}Ga_{0.6}As_{0.995}N_{0.005}$ ($In_{0.4}Ga_{0.6}As$) single-QW active layer sandwiched by a 300nm GaAs barrier. Here device quality material is obtained by maximizing the indium concentration to the limit imposed by strain so that a minimum amount of nitrogen, 0.5%, is needed to lower the bandgap to ~ 0.95 eV.

The lower and upper cladding layers are based on n-$Al_{0.85}Ga_{0.15}As$ and p-$In_{0.48}Ga_{0.52}P$, respectively. A very high compressive strain of 2.8% for InGaAs and of 2.5% for InGaAsN is imposed on the QW with growth. Partial strain compensation of the highly compressively strained QW is achieved by utilizing a 7.5nm-thick $GaAs_{0.85}P_{0.15}$ tensile strain layers offset 10nm from the QW, and a tensile strain buffer layer consisting of 3nm $GaAs_{0.67}P_{0.33}$, as shown in Figure 2.1. This approach of strain-compensation in a InGaAsN single QW structure by utilizing tensile GaAsP barriers provides a stronger electron and hole

confinements. This approach has resulted in very low (best reported) threshold current density in 1300-nm InGaAsN QW lasers under continuous-wave (CW) operation at room temperature up to the elevated temperature of 100 ^{0}C [5]. The

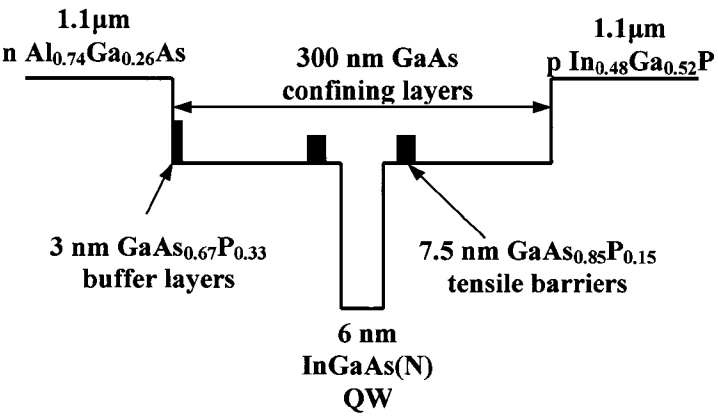

Figure 2. 1 Schematic structure of strain compensated InGaAs(N)/GaAs SQW diode lasers.

approach also resulted in the first InGaAsN QW lasers, grown by MOCVD, with lower (or better) threshold current density than the previous-record devices grown by MBE [6-9]. Threshold current densities of 200-210 A/cm^2 were realized for the strain-compensated 1280-1320 nm InGaAsN QW lasers. Threshold current densities of only 65-90 A/cm^2 and 450-540 A/cm^2 were also achieved for 1170-1233 nm InGaAs QW and 1370-nm InGaAsN QW lasers on GaAs [10] , respectively.

In the photoluminescence related measurement, the QW samples under investigation have an identical structure as the laser devices, except that they contain a thinner top cladding layer and lack a metal contact.

Broad area (BA) lasers are used in the photocurrent measurements for better signal to noise. Ridge waveguide (RWG) lasers with a narrow stripe width of ~ 4 μm and a length of 500 μm are utilized in the pump-probe experiments. Lasers of a narrow ridge contact provide a convenient way to align the pump and probe beam spatially. In addition, with a relative low threshold current for RWG lasers, I_{th}=10 mA for InGaAs and I_{th}=18 mA for InGaAsN respectively, heating due to biasing current is not a big issue compared with broad area lasers. Laser emission wavelengths for both structures are 1195nm (InGaAs) and 1275nm (InGaAsN), respectively.

2.2 Photoluminescence, continuous excitation and time resolved

2.2.1 CW photoluminescence measurements

For the cw photoluminescence (PL) spectra measurements, the samples are mounted on the cold finger of a closed-cycle Helium cryostat that allows varying the temperature from 10K to 300K. The set-up is shown in Figure 2.2. Laser sources with different wavelengths and intensities are employed to excite the samples. In our experiments, a mode-locked Ti:Sapphire laser emitting pulses at 800nm wavelength of 100fs duration and 82MHz repetition rate is used as the excitation light source. The pulse width here is estimated from self-correlation measurement. An optical parametric oscillator (OPO) which is synchronously pumped by the Ti-sapphire pulses, with pulse width of 150fs and emission

wavelength in the infrared region, is used to photo excite the carriers in the lowest QW states. These two laser sources are also used in pump-probe measurements, which are introduced in section 2.4. By selecting Ti-sapphire or OPO as the excitation light, carriers can be selectively generated within the GaAs barrier or just within the QW in the structure shown in Figure 2.1. The average excitation intensity absorbed by the sample is varied from 0.5 W/cm^2 to 50 W/cm^2 by changing the attenuation of the pump beam. Assuming that each photon generates one electron-hole pair, the corresponding photo-excited sheet carrier density varies from 2×10^{10} cm^2 to 2×10^{12} cm^{-2} . The time integrated PL is analyzed by a 2/3 m single grating spectrometer with a spectral resolution of 0.2nm and detected by a nitrogen cooled InGaAs detector using a lock-in technique. The spectral responsivity curve of the InGaAs-detector is shown in Figure 2.3. We use these data to calibrate and normalize the PL spectra. Figure 2.4 shows typical normalized PL spectra obtained after the calibration.

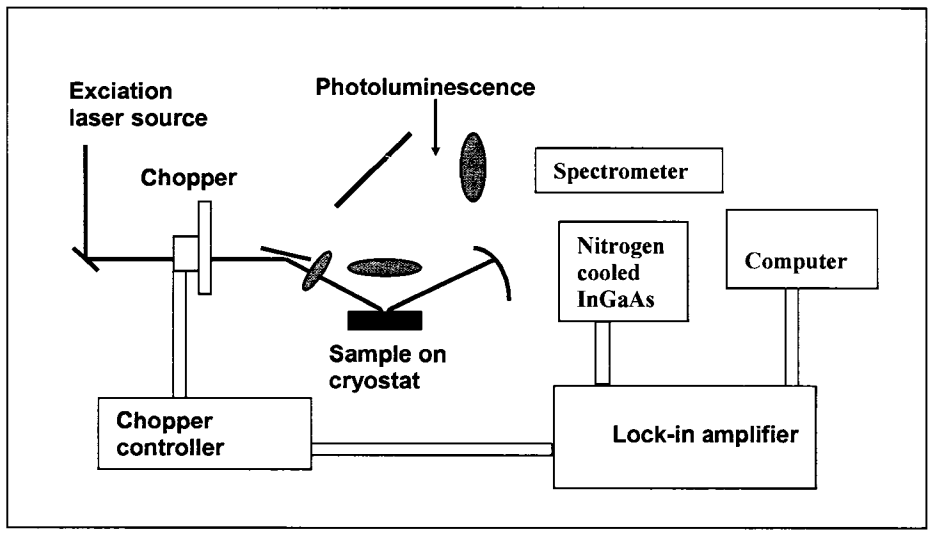

Figure 2. 2 Schematics of the continuous Photoluminescence spectra measurement setup.

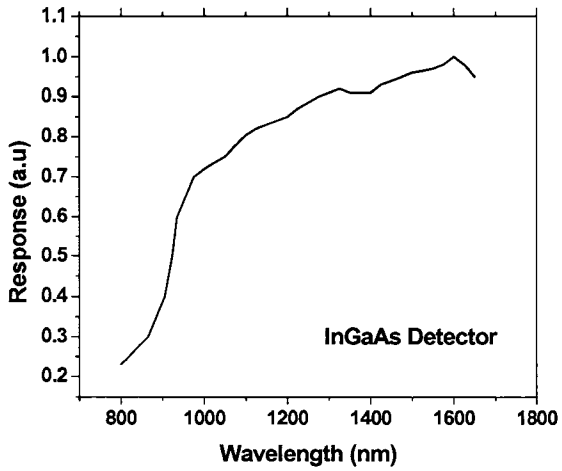

Figure 2. 3 Spectral Responsivity Curve of InGaAs detector.

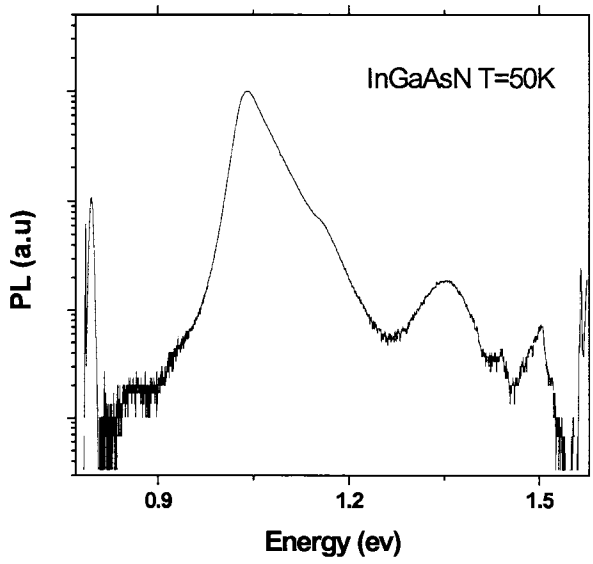

Figure 2. 4 Typical raw PL spectra at T=50K for InGaAs SQW laser structure without contacts. The PL intensity is in logarithmic scale.

2.2.2 Temporally evolved photoluminescence spectra measurements

The temporally resolved PL spectra measurements are performed using luminescence up-conversion with multichannel detection method [11]. The setup is presented in Figure 2.5. In this set up, the Ti-sapphire output is divided into two trains of pulses. One beam is used to excite the sample and to generate luminescence from the sample that is focused onto a 250μm-thick beta-barium-borate (BBO) crystal by a sequence of parabolic mirrors to avoid dispersion. Pulses of the second train are delayed by a delay stepper and are focused on the BBO crystal too. The up-converted signal that is generated is then analyzed by a charge-coupled device (CCD) in conjunction with a 0.3m monochromater. The time resolution and the spectral resolution of the up-conversion process are mainly limited by the pulsed duration and spectral width of the 800nm gating laser, ~100fs and 9meV, respectively.

The spectral bandwidth of the 250-μm-thin BBO is calculated to be 150-meV, which is broader than the luminescence spectra range of interest, 120 meV. The measured spectra are normalized by the spectral width of BBO crystal. Typical normalized PL spectra at particular time delays are shown in Figure 2.6.

This upconversion technique is, however, limited to short time delays, ~ 2 ns, mainly due to the mechanical translation length of the delay stepper. Thus, additional spectrally integrated photoluminescence intensity lifetime measurements were carried out in this work using a 25 GHz bandwidth InGaAs detector and a 25 ps rise time sampling oscilloscope. The simple set up is

schematically plotted in Figure 2.7. The PL decay data has been deconvolved with the system response. We deduce the system response function by replacing the PL sample with a piece of brass and analyzing the convolution of scattered light of the Ti-sapphire pulse with the system response. With the system response of ~35 ps, the pulse width of the Ti-sapphire, which is only 100 fs, can be regarded as a delta function. In this way, the measured convolution signal of brass is the system response function itself. Figure 2.8 plots the typical data and the system response curve.

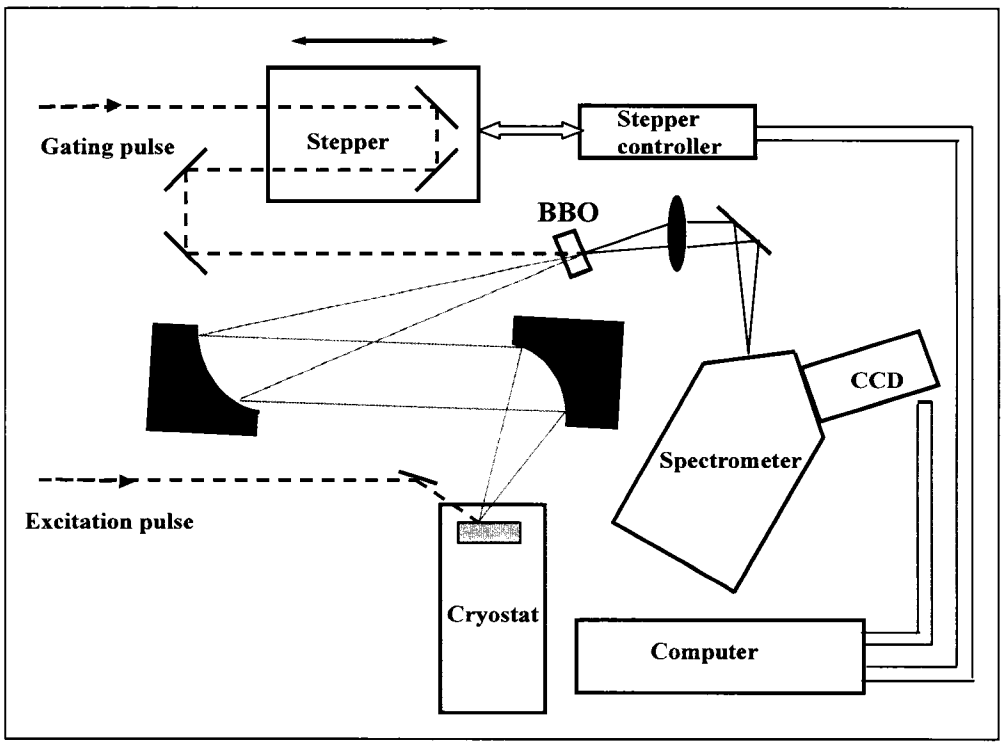

Figure 2. 5 Schematical drawing of the luminescence up-conversion setup.

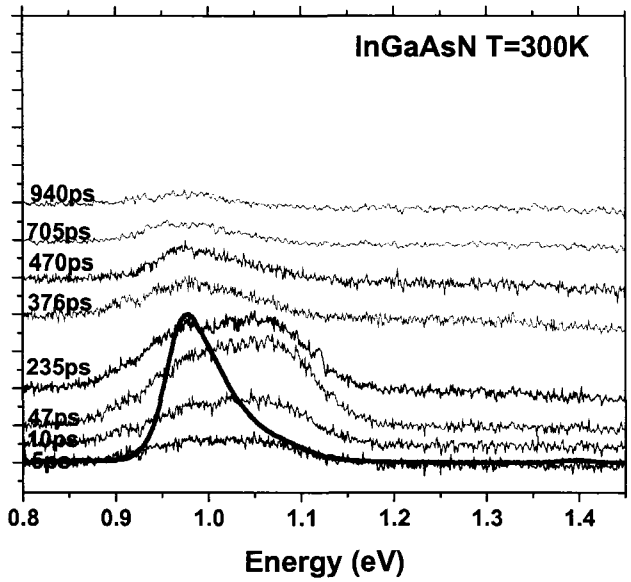

Figure 2.6 Temporarily resolved PL spectra of InGaAsN/GaAs SQW structure at different time delays with the pump power of 30 mW at T=300 K. The corresponding time integrated PL is also shown in the figure.

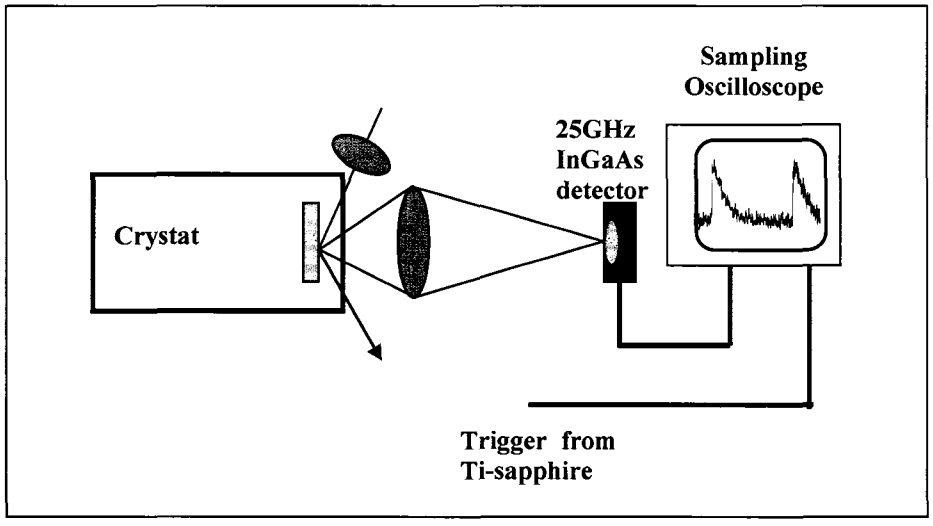

Figure 2.7 Direct photoluminescence intensity lifetime measurement under various temperatures.

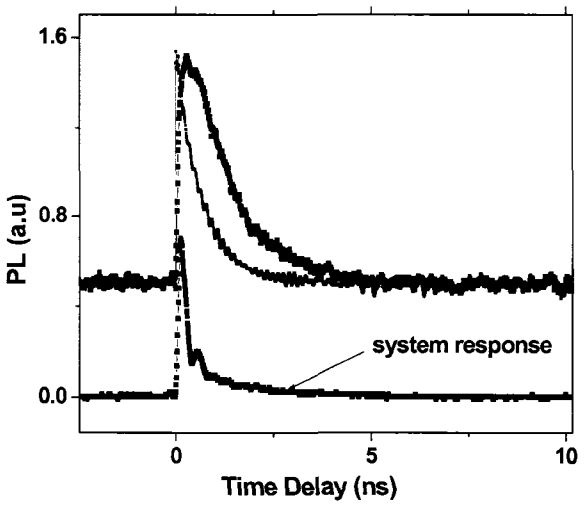

Figure 2.8 Normalized temporal evolution of the PL intensity (top curves) before (black) and after (red) deconvolution with system response. The bottom curve is the instrumental response function. The wavelength at which this signal is measured is that at the PL peak.

2.3 Polarization dependent Photocurrent

To univocally identify the origin of the different PL transitions, polarization sensitive photocurrent (PC) measurements were also performed at room temperature in an InGaAs(N)/GaAs broad area laser. In these measurements the edge of the laser structures are excited with the light from a tungsten halogen lamp dispersed via a 3/4m monochromator. The current generated in the laser diode is recorded as function of photon energy, as shown in Figure 2.9. Lock-in techniques are utilized to record the photocurrent. Figure 2.10 plots the white light spectra from the tungsten lamp. The photocurrent is analyzed after dividing the

spectra by this responsivity curve. Again, we obtain the white light spectra by using Germanium detector after the spectrometer, and then calibrate it with the responsivity of Ge detector.

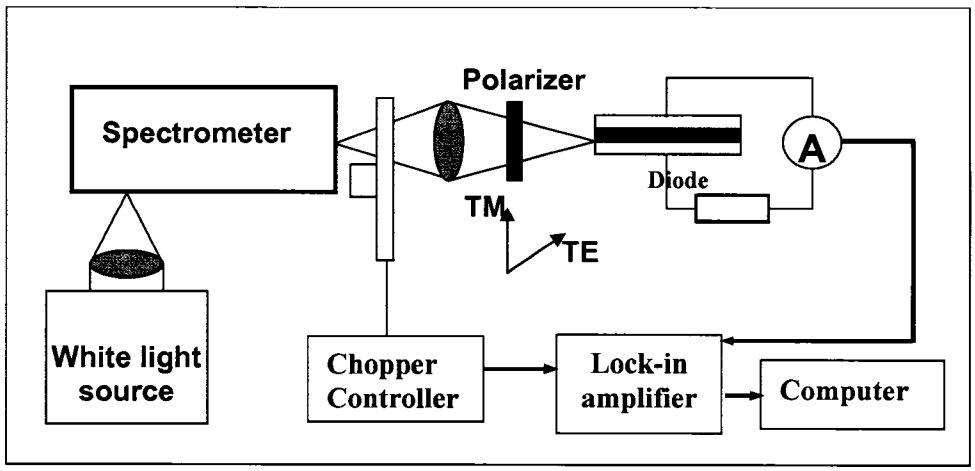

Figure 2. 9 Polarization dependent Photocurrent measurement.

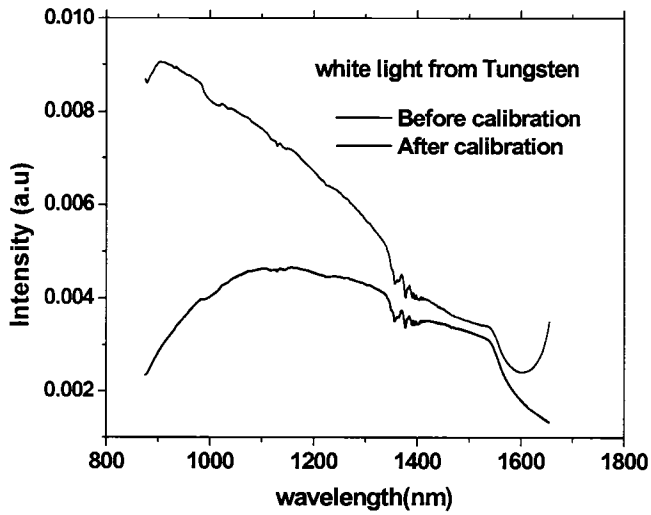

Figure 2.10 White light spectra from tungsten halogen lamp obtained with the Ge detector.

2.4 Pump-Probe transmission measurement

2.4.1 Principle of pump-probe transmission technique

In pump-probe experiments set up, two ultrashort pulse beams, a strong pump and a weak probe delayed by a time τ, are focused by a lens onto the sample. The transmission of the probe beam is detected as a function of pump-probe delay. This response measures the energy relaxation of the system.

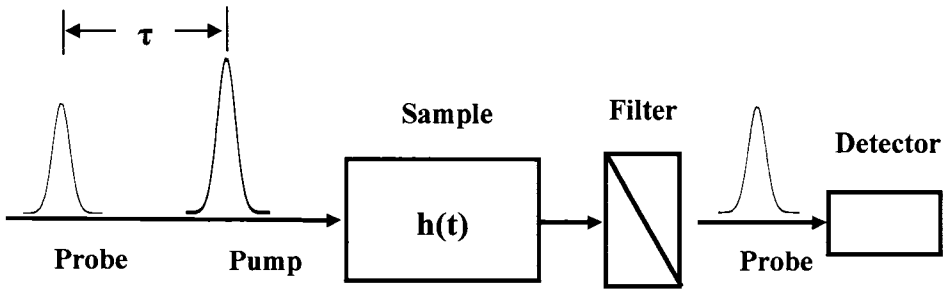

Figure 2.11 Principle of pump-probe measurement

Figure 2.11 schematically illustrates the basic principle behind the pump-probe techniques when an pump pulse of intensity $I_p(t)$ injected into a laser diode. It changes the carrier density and in turn affects the absorption (gain). If assume the impulse response function of the sample is h(t), then the change of absorption can be expressed as:

$$\Delta\alpha(t) = \int_{-\infty}^{+\infty} I_p(t')h(t-t')dt' \tag{2.1}$$

Now a weaker probe pulse delayed by τ relative to the pump pulse $I_{pr}(t-\tau)$ is injected into the laser diode to sense the change of absorption $\Delta\alpha(t)$ induced by pump pulse. The transmission of the probe is recorded by the detector and the induced change in transmission ΔT at delay time τ is the integration of the product of $\Delta\alpha(t)$ and $I_{pr}(t-\tau)$:

$$\Delta T(\tau) = \int_{-\infty}^{\infty} \Delta\alpha(t) I_{pr}(t-\tau)dt \tag{2.2}$$

Substituting Eq. (2.1) into Eq. (2.2), and writing $t-t' = t''+\tau$ yields:

$$\Delta T(\tau) = \int_{-\infty}^{\infty} dt'' h(t''+\tau) \int_{-\infty}^{\infty} dt' I_p(t') I_{pr}(t'+t'') \tag{2.3}$$

Thus the transmission change of probe is the pulse intensity cross-correlation

$$C(t'') = \int_{-\infty}^{\infty} dt' I_p(t') I_{pr}(t'+t'') \tag{2.4}$$

convoluted with the impulse response h(t) of the sample. So we see that the time resolution of the impulse response measurement is limited by the pulse cross-

correlation function. The shorter the pump and probe pulses, the better the resolution.

Figure 2.12 shows the experimentally determined intensity autocorrelation for both Ti-sapphire and the optical parametric oscillator (OPO) pulses, which have FWHM widths of 100 and 203 fs, respectively. Both of these have been utilized as pump or probe in our following experiments.

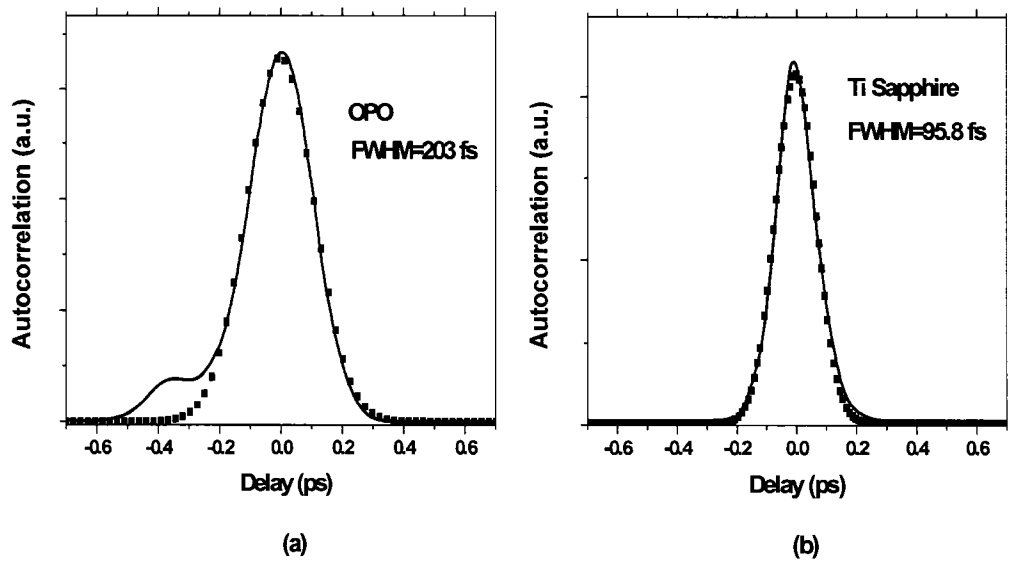

Figure 2.12 Intensity autocorrelation traces of the (a) OPO and (b) Ti-sapphire pulses.

When pumping the waveguide devices with short optical pulses, one disturbs the system's equilibrium, and the following interactions are reflected by a

impulse response function, h(t), in Eq. (2.3). The convolution of h(t) and the pulse intensity cross-correlation is reflected by the transmission change of probe.

In pump-probe experiment, one of the most important things is to distinguish the pump beam and probe beam after the sample. If the probe beam is indistinguishable from the pump beam, then background-free measurement of probe are difficult.

2.4.2 Cross polarization Pump-Probe transmission measurement

Figure 2.13 shows the schematics of the pump-probe set up to investigate the nonlinear gain dynamics. Both the pump and probe beams are generated by the optical parametric oscillator (OPO) which is synchronously pumped by the mode-locked Ti-sapphire pulse laser, as described in section 2.2. The average output power of the OPO is about 40 mW, with pulse width of 150 fs. The wavelength of the OPO is tuned to the corresponding emission wavelengths of the studied laser devices, by choosing the mirror sets of the cavity, adjusting the position of the PPLN crystal, and by slightly changing the cavity length. Using a neutral density (ND) filter, the power of the pump beam is chosen to be around 3 mW and ten times higher than that of the probe beam. The relative delay between the pump and the probe is controlled through a stepping-motor-driven translation stage. Two microscope objectives are used to couple the light into and out of the waveguide of the RWG laser devices. Both the pump and probe beams are aligned collinearly in the waveguide structure. Collinear pump and probe beams are

required to be coupled simultaneously and efficiently. To distinguish between the collinear pump and probe beams, the polarization of one of the beam is rotated with respect to the other by 90 degrees, and a polarizer is placed after the waveguide to select the probe beam for detection [12]. Generally the pump beam is set to TE-polarized and the probe beam TM-polarized. The polarization of the pump beam is selected to be that of laser's that stimulated emission. Here a lock-in technique is used where the pump beam is chopped and the probe beam is measured at the chopper frequency. These measurements were conducted for different laser bias, ranging from 0 mA to $0.8I_{th}$.

The typical raw data obtained from the photodiode corresponding to the induced change in probe transmission is plotted in Figure 2.14. The impulse function model will be used to fit the plot to investigate the nonlinear dynamics of the laser system after the gain is disturbed by the pump beam. Mathematical detail will be presented in section 5.2 of Chapter 5.

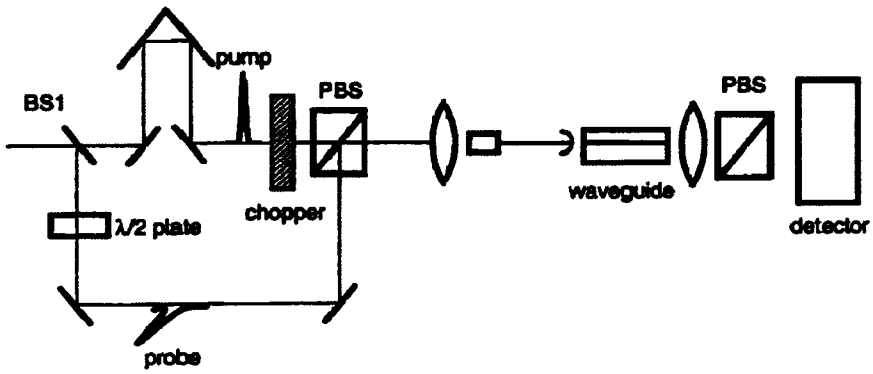

Figure 2.13 Pump-probe set up cross polarization and collinear beams. PBS: polarization beam splitter.

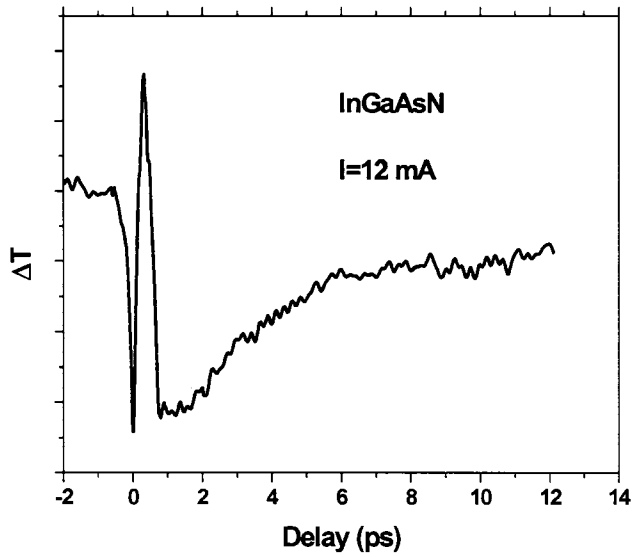

Figure 2.14 Measured changes in probe transmission as function of pump-probe delay (raw data) for InGaAsN/GaAs RWG single QW lasers at room temperature. The wavelength of both the pump and probe are chosen to be 1280 nm; the bias current I=12 mA. Thus experiments are performed in three regimes of gain. The pump is TE-polarized and the probe is TM polarized

2.4.3 Two color pump-probe transmission measurement

Pump and probe measurements with selective wavelengths are used to obtain the carrier capture and escape time in the QW laser active region. The first multiple-wavelength technique was developed by [13], where a short pulse pump beam and a cw probe beam combined with a gating technique are used. However, to obtain a reasonable sum frequency signal, this technique requires a relatively high cw probe power. Such high power will not be used in the experiments described here as it would disturb the equilibrium of the measured system and

make the data interpretation more difficult. In another broadband pump-probe technique, both pump and probe pulses are generated from a single laser oscillator. Before the probe pulse coupled into the waveguide, a white continuum light is obtained by focusing the laser pulse through either a water cell or a short single mode fiber. The most popular multiple-wavelength pump-probe measurement nowadays was proposed and realized by Sun [14][15]. This set up has a high power requirement for the laser oscillator.

We designed our experiments according to our instruments performance. The experimental setup is shown in Figure 2.15. The probe pulse train is generated from the OPO. The residual of the Ti-sapphire light used to pump the OPO is utilized as the pump beam. The wavelength of the OPO is tuned to the corresponding emission wavelengths of the studied laser devices, 1280 nm and 1200 nm, respectively. Taking advantage of the different wavelengths of the pump and the probe, we eliminate the pump pulses by using a 1150 nm long pass filter (LPF) before the final detection. A typical change in probe transmission is plotted as function of pump-probe delay in Figure 2.16. With the pump beam exciting only the unconfined state outside of the QW and probing the ground state in the well, the risetime of ΔT reflects the carrier capture process of carrier into the well. The decay time can be ascribed to contribution of both carrier escape from the well and carrier recombination. The latter, from the results of PL lifetime measurements in chapter 4 at room temperature, is on the order of 300-400 ps for InGaAsN and >2 ns for InGaAs lasers, respectively. Thus, the decay of ΔT observed here, which is less than ~100 ps, mainly represents the carrier escape

processes. Measurements under various laser bias were also conducted in order to extract the escape time τ_{esp} as function of biasing.

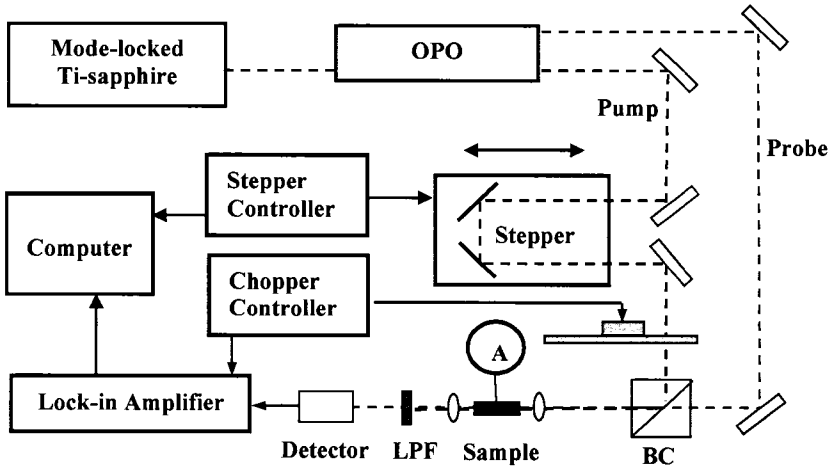

Figure 2.15 Experimental set up for two-color pump-probe transmission measurements. BC: beam combiner. LPF: long pass filter. A: current source.

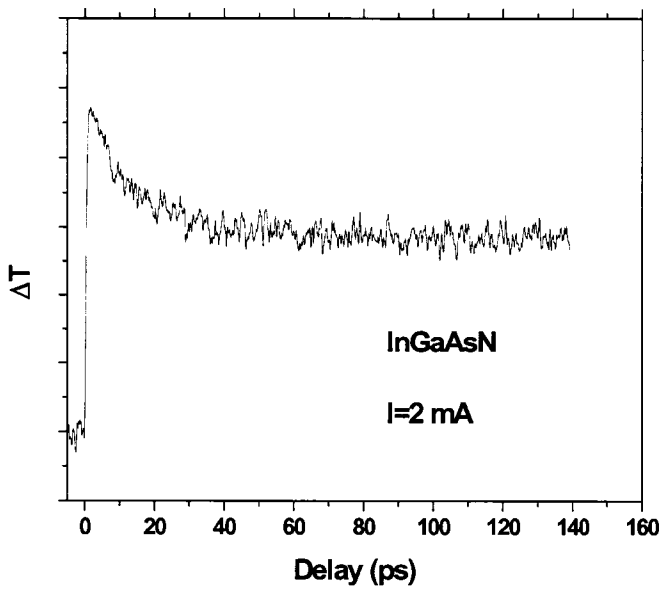

Figure 2.16 Typical relative changes in the probe transmission induced by the pump as function of the pump-probe delay in two color pump-probe measurements.

2.5 Amplified Spontaneous Emission

Part of this dissertation includes the analysis of gain in the InGaAsN structures. The gain spectrum was obtained by applying Hakki-Paoli analysis [16] on the amplified spontaneous emission (ASE) traces of InGaAs(N) RWG lasers cw biased. The ASE from one facet of laser diode is collected by a 20× objective lens and collimated into a fiber coupled Optical Spectrum Analyzer (OSA). The OSA is set to a resolution of 0.02 nm, with 5001 sampling points and HI-SENS2 mode. Figure 2.17 (a) shows the typical traces and the gain spectrum extracted from it by applying Hakki-Poli analysis is plotted in Figure 2.17 (b).

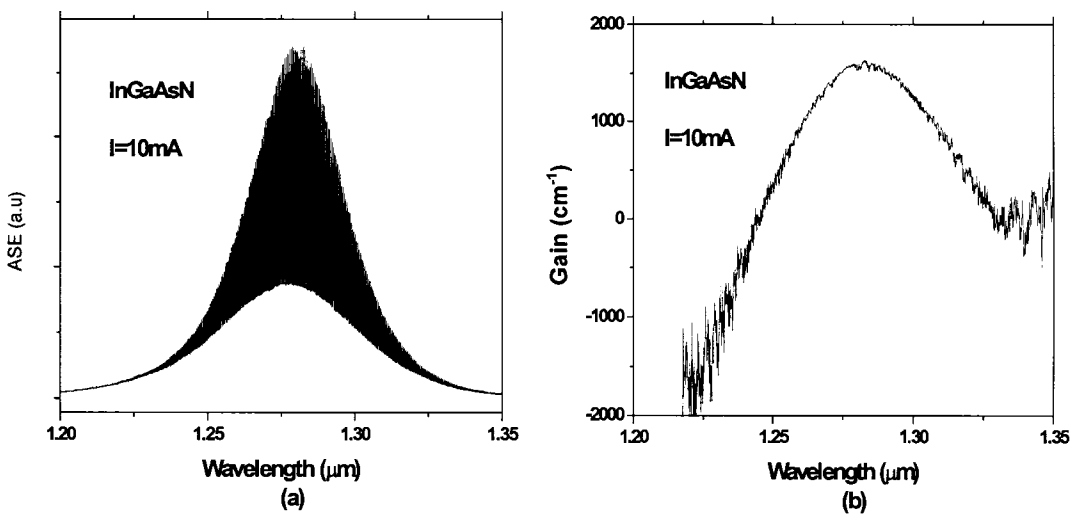

Figure 2.17 (a) Typical amplified spontaneous emission traces obtained in $In_{0.4}Ga_{0.6}As_{0.995}N_{0.005}$ single quantum well (QW) ridge waveguide (RWG) lasers and (b) the corresponding net modal gain spectra obtained from the ASE.

Reference:

[1] N.Tansu and L. J. Mawst, "Low-threshold strain-compensated InGaAs(N) (lambda=1.19-1.31 μm) quantum-well lasers", IEEE PHOTONICS TECHNOLOGY LETTERS **14** (4): 444-446 (2002).

[2] N.Tansu, Y.L. Chang, T. Takeuchi, D.P. Bour, S.W. Corzine, M.R.T. Tan and L.J. Mawst,"Temperature analysis and characteristics of highly strained InGaAs-GaAsP-GaAs (lambda > 1.17 μm) quantum-well lasers", IEEE JOURNAL OF QUANTUM ELECTRONICS **38** (6): 640-651 (2002).

[3] N.Tansu, N.J.Kirsch, L.J. Mawst, "Low-threshold-current-density 1300-nm dilute-nitride quantum well lasers", APPLIED PHYSICS LETTERS **81** (14): 2523-2525 (2002).

[4] N.Tansu, J.Y.Yeh and L.J.Mawst, "Extremely low threshold-current-density InGaAs quantum-well lasers with emission wavelength of 1215-1233 nm", APPLIED PHYSICS LETTERS **82** (23): 4038-4040 (2003).

[5] N.Tansu, A. Quandt, M. Kanskar, W. Mulhearn and L.J. Mawst, "High-performance and high-temperature continuous-wave-operation 1300 nm InGaAsN quantum well lasers by organometallic vapor phase epitaxy", APPLIED PHYSICS LETTERS **83** (1): 18-20 (2003).

[6] D.A.Livshits, A.Y.Egorov, H.Riechert, "8W continuous wave operation of InGaAsN lasers at 1.3 μm", ELECTRONICS LETTERS **36** (16): 1381-1382 AUG 3 (2000).

[7] C.S.Peng, T. Jouhti, P.Laukkanen, etc, "1.32-μm GaInNAs-GaAs laser with a low threshold current density", IEEE PHOTONICS TECHNOLOGY LETTERS **14** (3): 275-277 (2002)

[8] S.Sato, "Low threshold and high characteristic temperature 1.3 mu m range GaInNAs lasers grown by metalorganic chemical vapor deposition", JAPANESE JOURNAL OF APPLIED PHYSICS PART 1-REGULAR PAPERS SHORT NOTES & REVIEW PAPERS **39** (6A): 3403-3405 (2000).

[9] V. Gambin, W. Ha, M. Wistey, H. Yuen, S.R. Bank, S.M. Kim, J.S. Harris, "GaInNAsSb for 1.3-1.6-mu m-long wavelength lasers grown by molecular beam epitaxy", IEEE JOURNAL OF SELECTED TOPICS IN QUANTUM ELECTRONICS **8** (4): 795-800 (2002).

[10] J.Y.Yeh, N. Tansu and L.J. Mawst, "Long wavelength MOCVD grown InGaAsN-GaAsN quantum well lasers emitting at 1.378-1.41 mu m", ELECTRONICS LETTERS 40 (12): 739-741 (2004).

[11] S.Haacke, R.A.Taylor, I.Bar-Joseph, MJSP. Brasil, M. Hartig, B.Deveaud, "Improving the signal-to-noise ratio of femtosecond luminescence upconversion

by multichannel detection", JOURNAL OF THE OPTICAL SOCIETY OF AMERICA B-OPTICAL PHYSICS **15** (4): 1410-1417 APR (1998).

[12] M.S.Stix, M.P.Kesler, E.P.Ippen, "Observations of subpicosecond dynamics in GaAlAs laser-diodes", APPLIED PHYSICS LETTERS **48** (25): 1722-1724 JUN 23 (1986).

[13] M.P.Kesler and E.P. Ippen, " Subpicosecond spectral gain dynamics in AlGaAs laser-diodes", ELECTRONICS LETTERS **24** (17): 1102-1104 AUG 18 (1988).

[14] C.K.Sun, H.K.Choi, C.A.Wang, J.G.Fujimoto, " Studies of carrier heating in InGaAs/AlGaAs strained-layer quantum-well diode-lasers using a multiple wavelength pump probe technique", APPLIED PHYSICS LETTERS **62** (7): 747-749 FEB 15 (1993).

[15] C.K.Sun, B.Golubovic, J.G.Fujimoto, H.K.Choi, C.A.Wang, " Heterodyne nondegenerate pump-probe measurement technique for guided-wave devices", OPTICS LETTERS **20** (2): 210-212 JAN 15 (1995).

[16] B.W. Hakki and T.L. Paoli, " Gain spectra in GaAs double heterostructure injection lasers", JOURNAL OF APPLIED PHYSICS **46** (3): 1299-1306 (1975)

CHAPTER 3

Analytical Gain Model

In this chapter, the analytical models that are used to calculate the band diagram and the gain in the active region of laser structures are constructed to help investigate and predict the influence of nitrogen incorporation. The interband transition energies at k=0 are firstly calculated, incorporating strain and by using the band anti-crossing (BAC) approach. We refrain from using k*p simulation to determine the E-k dispersion curve, allowing interband interaction and hence non-parabolicity of bands, as it is computationally demanding and does not favor intuitive estimation. We, therefore, calculate the gain spectra by assuming a parabolic band structure and test it against k*p model results from previous published literature. The aim of this chapter is to provide a guideline for the experimental data obtained in the next following chapters. The discrepancy between the theory and experiments can in this way be better understood.

3.1 Band diagram calculation

3.1.1 InGaAs/GaAs QW Band Offset Calculation

In the calculation of the quantum well (QW) band diagram, the band alignments between InGaAs(N) QW and the GaAs barrier are estimated using the model solid theory where the relative energies of the bands on an "absolute" scale are given. The band alignment is first calculated for the InGaAs host by incorporating strain. The effect of nitrogen is introduced only on the conduction band by applying band anti-band crossing (BAC) theory, as well as an adjusted strain and adjusted band offset ratio.

The expressions for bulk conduction band (c) , heavy-hole (hh) and light-hole (lh) of strained $In_{0.4}Ga_{0.6}As$ are given by [1]:

$$E_c(InGaAs) = E_{v,av}(InGaAs) + \frac{\Delta(InGaAs)}{3} + E_g + P_c \qquad (3.1)$$

$$E_{hh}(InGaAs) = E_{v,av}(InGaAs) + \frac{\Delta(InGaAs)}{3} - P_v - Q_v \qquad (3.2)$$

$$E_{lh}(InGaAs) = E_{v,av}(InGaAs) + \frac{\Delta(InGaAs)}{3} - P_v + Q_v - 2\frac{Q_v^2}{\Delta(InGaAs)} \qquad (3.3)$$

where $E_{v,av}$ is the average energy of the three top valence band, Δ is the spin-orbit split-off energy, E_g is the bandgap energy and P_c, P_v and Q_v determine the band edge shift due to strain, and are expressed as:

$$P_c = -2a_c \frac{C_{11} - C_{12}}{C_{11}} \varepsilon \tag{3.4}$$

$$P_v = -2a_v \frac{C_{11} - C_{12}}{C_{11}} \varepsilon \tag{3.5}$$

$$Q_v = -b \frac{C_{11} + 2C_{12}}{C_{11}} \varepsilon \tag{3.6}$$

The lattice-mismatch parameter, ε, is defined as $\varepsilon = \frac{a_s - a_w}{a_w}$. Here a_s and a_w are the lattice constants for the GaAs barrier and InGaAs well, C_{11} and C_{12} are the in-plane and out-of-plane elastic stiffness constants, a_c and a_v are the hydrostatic deformation potentials for conduction band and valence band, b is the shear deformation potential.

The band offset for the conduction, heavy hole and light bands are obtained as:

$$\Delta E_c(\text{InGaAs}) = E_c(\text{GaAs}) - E_c(\text{InGaAs}) \tag{3.7}$$

$$\Delta E_{hh}(\text{InGaAs}) = E_{hh}(\text{InGaAs}) - E_v(\text{GaAs}) \tag{3.8}$$

$$\Delta E_{lh}(InGaAs) = E_{lh}(InGaAs) - E_v(GaAs) \tag{3.9}$$

where for GaAs barrier, since it is a much thicker layer compared to the QW, the effect of strain is negligible and the expression for E_c(GaAs), E_v(GaAs) reduce to:

$$E_c(GaAs) = E_{v,av}(GaAs) + \frac{\Delta(GaAs)}{3} + Eg(GaAs) \tag{3.10}$$

$$E_c(GaAs) = E_{v,av}(GaAs) + \frac{\Delta(GaAs)}{3} \tag{3.11}$$

3.1.2 Nitrogen Incorporated QW Band Calculation

In our calculation, the effect of nitrogen incorporation is mainly reflected in the change of the conduction band after applying the BAC model. Minor changes in the lattice constants and strain are also considered.

Two of the most important parameters in the BAC model are E_N and V_{NC}, which characterize the position of the nitrogen induced energy level above conduction band E_C(InGaAsN) and the strength of the interaction between E_C(InGaAsN) and E_N, respectively. This interaction is repulsive, giving rise to two states E- and E+. The E- is, in the BAC model, taken to be the fundamental new conduction band edge for InGaAsN and is expressed as the solution of the eigenvalue equation:

$$\begin{vmatrix} E - E_C(InGaAsN) & V_{NC} \\ V_{NC} & E - E_N \end{vmatrix} = 0 \qquad (3.12)$$

$$E_{-} = \frac{E_N + E_C(InGaAsN) - \sqrt{(E_N - E_C(InGaAsN))^2 + 4V^2{}_{NC}}}{2} \qquad (3.13)$$

The expression for E_C(InGaAsN), E_N and V_{NC} are adopted from reference [2][1],

$$E_C(InGaAsN) = E_C(InGaAs) - 1.55y + 3.5y \qquad (3.14)$$

$$E_N = E_C(InGaAsN) + 0.44eV \qquad (3.15)$$

$$\text{and} \quad V_{NC} = 3.2\sqrt{y} \qquad (3.16)$$

where y is the nitrogen content in InGaAsN alloy.

Although it is under debate, several experimental references have pointed out that the incorporation of N into InGaAs likely leads to an increase of the conduction-band-offset ratio (Qc=ΔEc /ΔEg) from 60%–65% to about 80%. We take into account these calculations to obtain an adjusted band offsets from our calculation.

$$\Delta E_c(InGaAsN) = ((E_c(GaAs) - E_{-}) + (E_{hh}(InGaAsN) - E_v(GaAs)) \cdot 0.8 \qquad (3.17)$$

$$\Delta E_{hh}(InGaAsN) = ((E_c(GaAs) - E\_) + (E_{hh}(InGaAsN) - E_v(GaAs)) \cdot 0.2 \quad (3.18)$$

$$\Delta E_{lh}(InGaAsN) = \Delta E_{hh} - (E_{hh}(InGaAsN) - E_{lh}(InGaAsN)) \quad (3.19)$$

3.1.3 Calculation of the Quantized States

After the band offsets are derived, we are now in the position of calculating the confined states in the quantum well, where the depth of the potential $V_0=\Delta E_C$ for electrons and $\Delta E_{hh(lh)}$ for heavy(light) holes are given in equation (3.17) and (3.18).

The number of bound states N is determined by

$$(N-1)\frac{\pi}{2} \le \sqrt{\frac{2m_w * V_0}{\hbar^2}}\frac{L}{2} \le N\frac{\pi}{2} \quad (3.20)$$

and the eigenenergy E_n is determined by searching for the root of both equations:

$$y = \frac{m_b *}{m_w *} x \tan(x) \text{ or } y = -\frac{m_b *}{m_w *} x \cot(x) \quad (3.21)$$

$$y = \sqrt{\frac{m_b *}{m_w *}\left[\frac{2m_w V_0}{\hbar^2}(\frac{L}{2})^2 - x^2\right]} \quad (3.22)$$

where $E_n = \frac{\hbar^2}{2m_w}(\frac{x}{L})^2$.

Figure 3.1 shows the typical plot of Eq. (3.21) and (3.22) which are solution of Schrödinger equation for a finite potential well.

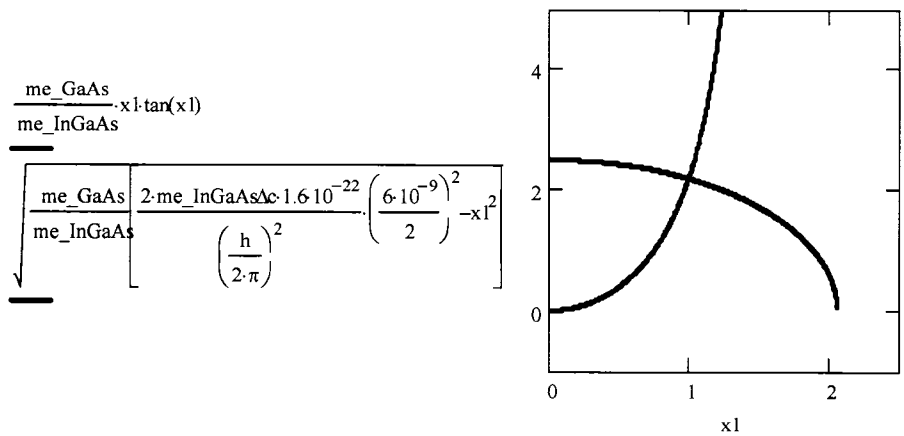

Figure 3.1 Typical plot of Eq. (3.21) and (3.22). The intersection of the two curve yield the solution of quantized state for a finite potential well.

But in a laser structure, the separate confinement region is sandwiched between n and p regions. Here we also take into account the effect of the built-in electric field F due to the p-n doping in the cladding layers. This is done by modifying the Hamiltonian as

$$H = H_0 + eFz \tag{3.23}$$

Treating $H' = eFz$ as a perturbation to H_0 shifts the eigenenergy E_n as:

$$E_n = E_n^{(0)} + C_n \frac{m_w * e^2 F^2 L^4}{\hbar^2} \tag{3.24}$$

where C_n is given by

$$C_n = \frac{n^2\pi^2 - 15}{24n^4\pi^4} \tag{3.25}$$

3.1.4 Band Parameters for the ternary and quaternary alloys

The band parameters of the parental binary compounds that from the ternary and quaternary QW used in our calculations are taken from Ref.[3] and are listed in Table 3.1. The parameters for $In_xGa_{1-x}As$ and $In_xGa_{1-x}As_{1-y}N_y$ are interpolated as follows:

$$P(In_xGa_{1-x}As) = (1-x)P(GaAs) + xP(InAs) \tag{3.26}$$

$$\begin{aligned} &P(In_xGa_{1-x}As_{1-y}N_y) = \\ &(1-x)(1-y)P(GaAs) + x(1-y)P(InAs) + (1-x)yP(GaN) + xyP(InN) \end{aligned} \tag{3.27}$$

Hole effective mass

$$m_{hh(lh)}(In_xGa_{1-x}As) = \frac{1}{\frac{1-x}{m_{hh(lh)}(GaAs)} + \frac{x}{m_{hh(lh)}(InA)}} \tag{3.28}$$

In our calculation, the hole effective masses for InGaAsN are the same as InGaAs. This is the case because the incorporation of nitrogen does not affect the heavy hole and light hole band structure.

For the band gap energy and electron effective mass of $In_xGa_{1-x}As$, we have included bowing parameters [3]

$$E_g(In_xGa_{1-x}As) = (1-x)E_g(GaAs) + xE_g(InAs) - 0.477x(1-x) \quad (3.29)$$

$$m_e^*(In_xGa_{1-x}As) = (1-x)m_e^*(GaAs) + xm_e^*(InAs) - 0.0091x(-x) \quad (3.30)$$

Table 3. 1 Parameters for parental binary compounds at T=300K.

Parameters	GaN	InN	GaAs	InAs
a (Å)	4.55	5.03	5.65	6.058
E_{v_av} (eV)			-6.92	-6.67
Δ (eV)	0.017	0.006	0.34	0.38
E_g (eV, T=300 K)			1.424	0.354
C11 (10^{11} dyne/cm^2)	29.3	18.7	11.879	8.329
C12 (10^{11} dyne/cm^2)	15.9	12.5	5.376	4.526
a_v (eV)	-0.69	-0.7	1.16	1
a_c (eV)	-6.71	-2.65	-7.17	-5.08
b (eV)	-2	-1.2	-1.7	-1.8
γ_1	2.83	3.77	7.65	19.67
γ_2	0.85	1.33	2.41	8.37
γ_3	1.14	1.6	3.28	9.29

The band gap of $In_xGa_{1-x}As_{1-y}N_y$, as we stated in section 3.1.2, is derived from that of $In_xGa_{1-x}As$, combined with the BAC model. As for the electron effective mass of $In_xGa_{1-x}As_{1-y}N_y$, however, to date no direct determination of m_e^* has been reported for the high Indium content (30%~40%) $In_xGa_{1-x}As_yN_{1-y}$, mainly due to the difficulties in growing thick freestanding epilayer (typically 1~3 μm) for accurate measurements. There are basically two approaches to predict electron effective mass, the phenomenological relationship [4] and band anti-crossing (BAC) model [5][6]. Later in chapter 4 we will show how we experimentally determine m_e^* from a lineshape analysis of the temperature dependent photoluminescence spectra in combination with a fractional parameter model. Here we employ the result from the theoretical models and will show that m_e^* is not a critical factor in the band diagram calculation, but it does play a very important role in gain.

The phenomenological relationship that predicts m_e^* of $In_xGa_{1-x}As_{1-y}N_y$ is given by

$$m_e^*(In_xGa_{1-x}As_{1-y}N_y) = m_e^*(In_xGa_{1-x}As) + 18.667m_0\Delta e(x,y) \quad (3.31)$$

$$m_e^*(In_xGa_{1-x}As_{1-y}N_y) = m_e^*(In_xGa_{1-x}As) + 18.667m_0\Delta e(x,y) \quad (3.31)$$

where $\Delta e(x,y)$ is the difference of strain between $In_xGa_{1-x}As_{1-y}N_y$ and $In_xGa_{1-x}As$.

The m_e^* of $In_xGa_{1-x}As_{1-y}N_y$ as predicted by the BAC model is given by

$$m_e^*(In_xGa_{1-x}As_{1-y}N_y) = 2m_e^*(In_xGa_{1-x}As)/(1-\frac{E_C-E_N}{\sqrt{(E_C-E_N)^2+4V_{NC}^2}}) \quad (3.32)$$

For the high indium content $In_{0.4}Ga_{0.6}As_{0.995}N_{0.005}$, the phenomenological relationship predicts $m_e^*=0.069m_0$ while the BAC model calculates $m_e^*=0.083m_0$. In the rest of the analysis, we will adopt $m_e^*=0.083m_0$ to test our model against published k*p model as it reflects the trend obtained from experiments, where m_e^* is measured to be $m_e^*=0.11m_0$.

3.1.5 Results

Our calculation is based on the specific $In_xGa_{1-x}As_{1-y}(N_y)$/GaAs QW structure studied in this thesis, where x=0.4 and y=0 (0.005), with well width of 6nm, barrier width 300 nm and two 7.5 nm GaAsP strain compensated layers. Although the function of the GaAsP layer is to compensate the high strain of the QW and enhance the optical quality, in our band diagram calculation, this strain compensation is not taken into account due to the small thickness of the layer. However, it is accounted for the total strain of the QW.

The results of the calculated band diagrams for InGaAs and InGaAsN at T=300K are shown schematically in Figure 3.2. The compressive strain is 2.7% for $In_{0.4}Ga_{0.6}As$ and 2.5% for $In_{0.4}Ga_{0.6}As_{0.995}N_{0.005}$, as shown in the diagram. The resulting conduction and valence band discontinuities are ΔE_C=251 meV, ΔE_{hh}=177 meV for InGaAs and ΔE_C=421 meV, ΔE_{hh}=105 meV for InGaAsN QW. The band offset for InGaAsN QW corresponds to the adjusted results based on the 80% band offset ratio. Notice that using the model solid theory, the band offset

ratio for InGaAs QW gives Q_c=58.6%, close to the range of 60%-65% given in the literature.

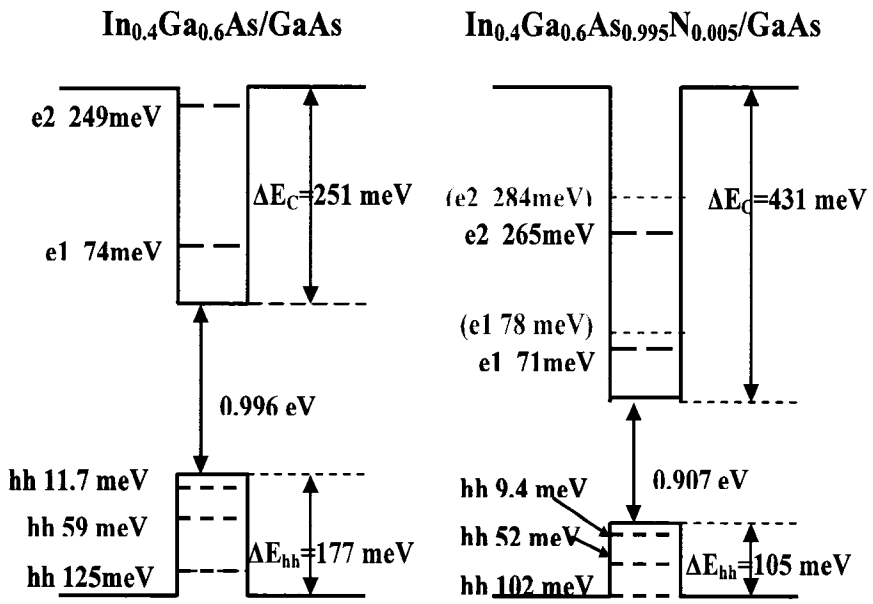

Figure 3.2 Band lineup for conduction and valence bands of $In_{0.4}Ga_{0.6}As/GaAs$ and $In_{0.4}Ga_{0.6}As_{0.995}N_{0.005}/GaAs$ QW lasers at T=300K. For the calculation of conduction band bound states of InGaAsN two values of the effective mass are used, $m_e^*=0.083m_0$ (black line) and $m_e^*=0.067m_0$ (gray line).

Due to the large strain in the InGaAs and InGaAsN QW, the valence band consists of only heavy-hole subbands in the 2D states, with light-hole states having bulk-like 3D properties where ΔE_{lh}=-64 meV (InGaAs) and -49meV (InGaAsN).

The temperature dependence of the ground state transition energy can be derived from the Varshni equation [9]:

$$E(T) = E(0) - \frac{\alpha T^2}{T + \beta} \tag{3.33}$$

where T is the absolute temperature, and α and β are constants. α and β of $4.7X10^{-4}$ eV/K and 253.707 K are obtained for InGaAsN from the fit of our temperature dependent PL data between 80 and 300 K, the region that is absent from carrier localization. Similarly, α and β values of $4.3X10^{-4}$ eV/K and 247.42 K are obtained for InGaAs.

3.2 Optical Gain Model

The optical gain spectrum for QW structure is calculated using [10]

$$g(N,E) = \sum_{m,n} C_0(E)\frac{2}{L_z}\int_0^{\infty} M_{m,n}(k)\frac{\frac{\gamma_k}{\pi}}{(E_{cv}(k)-E)^2+\gamma_k{}^2}(f_c(N,k)-f_v(N,k))\frac{k}{2\pi}dk \quad (3.34)$$

Where $C_0(E) = \frac{\pi e^2\hbar}{n_g c\varepsilon_0 m_0{}^2 E}$, e and m_0 are the free electron charge and mass, respectively, n_g is the refractive index of the QW material, c is speed of light, ε_0 is the free-space dielectric constant and E is the photon energy. All of these parameters are given in Table 3.2 for the 0 and 0.5% nitrogen containing wells. M_{cv} is the optical momentum matrix element which is polarization dependent in QWs. $\frac{\frac{\gamma_k}{\pi}}{(E_{cv}(k)-E)^2+\gamma_k{}^2}$ reflects the linewidth broadening where $E_{cv}(k)$ is the dispersion curve for the ground state and γ_k is the linewidth.

Table 3.2 Parameters used in gain model for the 0 and 0.5% nitrogen containing wells.

Parameters	$In_{0.4}Ga_{0.6}As/GaAs$ QW	$In_{0.4}Ga_{0.6}As_{0.995}N_{0.005}/GaAs$ QW
E_g (T=300K, eV)	0.996	0.907
α (eV/K)	$4.3X10^{-4}$	$4.7X10^{-4}$
β (K)	247.42	253.707
E_{c1} (meV)	74	71
E_{c2} (meV)	249	265
E_{hh1} (meV)	11.7	9.4
E_{hh2} (meV)	59	52
E_{hh3} (meV)	125	102
m_e*	0.047 m_0	0.083 m_0 (0.11m_0)
m_{hh}*	0.457 m_0	
Δ (eV)	0.356	
γ_k (meV)	9	
n_g	3.69	
e (C)	1.6×10^{-19}	
ε_0 (F/m)	8.8542×10^{-12}	
m_0 (kg)	9.1095×10^{-31}	
$\hbar$ (eV·s)	0.701×10^{-15}	
c (m/s)	3×10^{8}	

Usually a nonparabolic band structure can be obtained by applying the k*p method, but here we employ the parabolic assumption for simplicity, where

$$E_{cv}(k) = E_g + E_{cn} + E_{vm} + \frac{\hbar^2 k^2}{2m_e^*} + \frac{\hbar^2 k^2}{2m_v^*} \tag{3.35}$$

and E_{cn} and E_{vm} are the interband confined transition energies at k=0, obtained from results of Figure 3.2. m_e^* and m_v^* are the effective mass for electron and holes (Table 3.2). $(f_c(N,k) - f_v(N,k)$ is the Fermi-Dirac inversion factor, which is dependent on the quasi-Fermi level for a given injection carrier density in the well. Later in section 3.2.4, we will test our results from the parabolic E(k) assumption against those from k*p simulation. While our results are slightly off compared to k*p data, the overall agreement is good, thus our simplified model gives an insightful prediction of the laser performance.

3.2.1 Optical Transition Matrix Element

The optical momentum matrix element, $M_{m,n}$, describes the strength of the optical transition between the conduction and valence band and is polarization dependent for the QW structure. We are more interested in gain spectra for TE (perpendicular to growth direction) polarization because the laser is TE polarized. The approach for TM polarization will be similar.

For TE polarization, $M_{m,n}$ can be generally expressed as:

$$M_{m,n}(k) = \frac{3}{4}\left[< \phi_n \mid g_m^{(1)} >^2 + < \phi_n \mid g_m^{(2)} >^2 \right] \frac{m_0}{6} E_P \qquad (3.36)$$

$$E_P = \frac{3}{2}\left(\frac{m_0}{m_e^*} - 1\right) \frac{E_g(E_g + \Delta)}{\left(E_g + \frac{2}{3}\Delta\right)} \qquad (3.37)$$

ϕ_n and g_m are the conduction and hole subband eigen functions. There are many factors affecting the selection of ϕ_n and g_m, such as the band anti-crossing of the conduction band with the nitrogen localized state, valence band mixing, interaction between conduction band and valence bands, value of m_e^*, and many others. The solution of the ground state wavefunctions can be obtained only through a numerical approach under this situation. Meanwhile, the choice of ϕ_n and g_m brings up uncertainty in the theoretical calculation of $M_{m,n}$. We will clarify later in section 3.2.3, for the first time, that the uncertainty of $M_{m,n}$ in theory leads to the discrepancy in the prediction of laser performance due to nitrogen incorporation, such as intrinsic differential gain dG/dN.

For the simplified parabolic model, $M_{m,n}$ for a QW can be obtained analytically as:

$$M_{m,n}(k) = \frac{3}{4}(1 + \cos^2\theta) \frac{m_0}{6} E_P \qquad (3.38)$$

where the angular factor $\cos^2\theta$ is related to the electron or hole wave vectors by

$$\cos^2\theta = \frac{k_z^{\,2}}{k^2 + k_z^{\,2}} = \frac{E_{cn} + E_{vm}}{E_{cn} + E_{vm} + \dfrac{\hbar^2 k^2}{2m_r}} \tag{3.39}$$

The reduced effective mass m_r is defined as:

$$\frac{1}{m_r} = \frac{1}{m_e^*} + \frac{1}{m_v^*} \tag{3.40}$$

3.2.2 Quasi-Fermi Levels and Carrier Density

In order to investigate the gain spectra, the corresponding distribution function f_c and f_v for electrons and holes respectively at a selected energy E_c and E_v (Eq. (3.41) and (3.42)) are needed. The quasi-Fermi level F_c and F_v have to be determined for a given carrier density N.

$$f_c(N, E_c) = \frac{1}{1 + \exp[(E_c - F_c(N))/k_B T]} \tag{3.41}$$

$$f_v(N, E_v) = \frac{1}{1 + \exp[(-E_v - F_v(N))/k_B T]} \tag{3.42}$$

Here $E_c = E_g + E_{cn} + \dfrac{\hbar^2 k^2}{2m_e^*}$ and $E_v = \dfrac{\hbar^2 k^2}{2m_v^*}$

Obtaining F_c and F_v requires calculating the inverse of the Fermi-Dirac integral:

$$N = \int_{Eg}^{\infty} f_c(E)\rho_c(E)dE \tag{3.43}$$

For bulk material, the density of state $\rho_c(E) \propto \sqrt{E - E_g}$, and no analytical solution exists to calculate the Fermi level, thus various approximations have been used over the years. For the QW structure instead, the density of states is a step like constant function which can be expressed as

$$\rho_c(E) = \frac{m^*}{\pi\hbar^2 L_z}\sum_n H(E - E_n) \tag{3.44}$$

where $H(E-E_n)$ is a heaviside step function $H(x)=1$ for $x>0$ and $H(x)=0$ for $x<0$. Thus the integral has a closed form solution. For the carrier density of interest (below threshold carrier density, ~ 3×10^{18} cm^{-3}), the quasi-Fermi levels are just exceeding the first confined conduction band and valence band states, and do not fill up to the second confined states, thus we can write the expressions for F_c and F_v as:

$$F_c(N) = E_{11} + k_B T \ln[\exp(\frac{\pi\hbar^2 L_z}{k_B T m_e^*}N) - 1] \tag{3.45}$$

$$F_v(N) = -k_B T \ln[\exp(\frac{\pi\hbar^2 L_z}{k_B T m_{hh}^*} N) - 1] \quad (3.46)$$

where the top of the first confined heavy hole subband hh1 is set as energy zero, $E_{11}=E_g+E_{c1}+E_{hh1}$.

For the TE mode, the population inversion occurs when the separation of electron and hole quasi-Fermi levels exceeds E_{11}. The transparent carrier density N_{tr} is thus defined as the carrier density at which population inversion takes place:

$$F_c(N_{tr}) - F_v(N_{tr}) = E_{11}(N_{tr}) \quad (3.47)$$

where the E_{11} is corrected for bandgap shrinkage due to carrier filling. $E_{11}(N_{tr})=E_{11}-\xi N^{1/3}$. Figure 3.3 shows the typical calculated quasi-Fermi level $\Delta\mu=F_c-F_v$ and the band transition as a function of carrier concentration at T=283K. The intersection point gives N_{tr}.

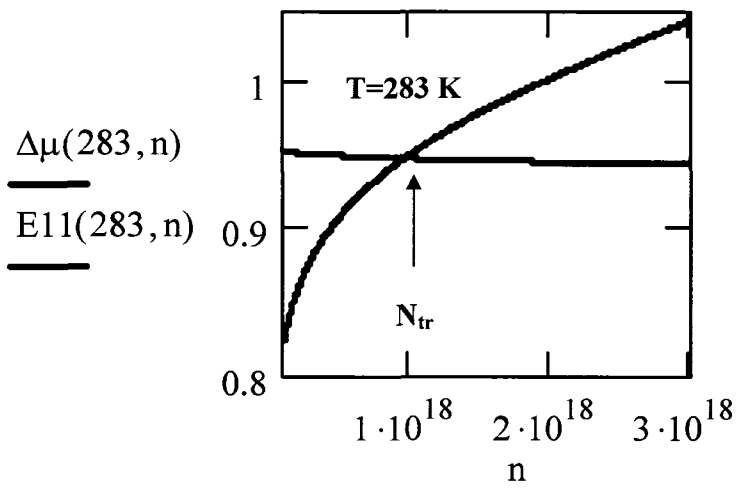

Figure 3.3 The separation of quasi-Fermi level $\Delta\mu=F_c-F_v$ and the band transition as function of carrier concentration at T=283K. The intersection point gives N_{tr}

3.2.3 Typical model results

Computed steady-state TE mode gain spectra for different carrier concentration at T=283 K are shown in Figure 3.4(a) for $In_{0.4}Ga_{0.6}As/GaAs$ QW and Figure 3.4(b) $In_{0.4}Ga_{0.6}As_{0.995}$ /GaAs QW. Here $m_e^*(InGaAs)=0.047m_0$ and the bandwidth γ_k=9meV are used in the calculation. To compare with the results from k*p simulation in reference [11], the electron effective mass from the BAC model $m_e^*(InGaAsN)= 0.083\ m_0$ and a same γ_k as InGaAs are adopted for the InGaAsN QW gain calculation. From the figure, a noticeable increase of transparentcy carrier density and a decreased in dG/dN are observed, as plotted in Figure 3.5.

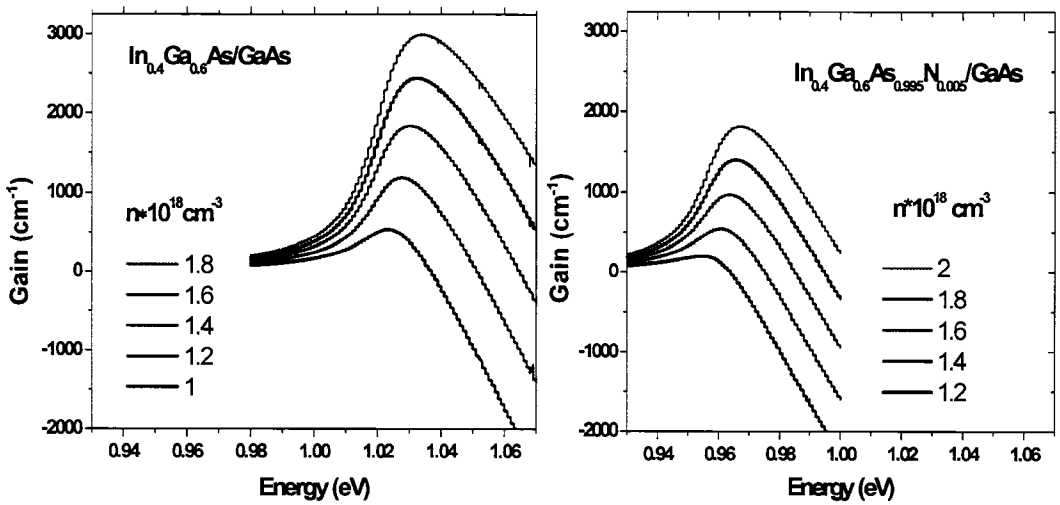

Figure 3.4 Steady state modal gain for different carrier density as function of photon energy at T=283 K.

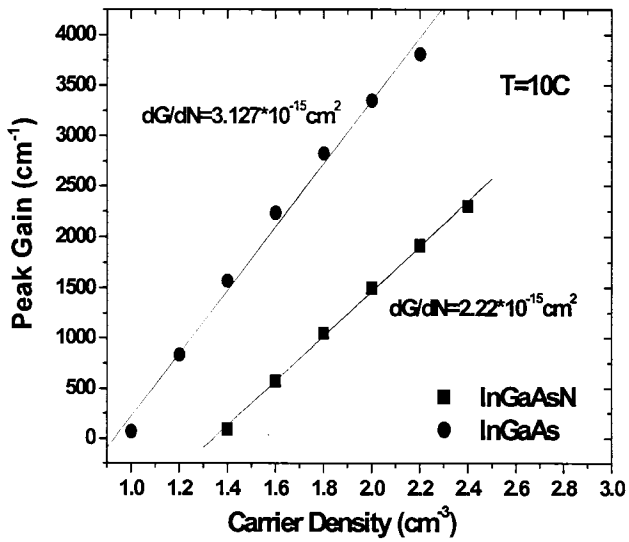

Figure 3.5 Peak modal gain as function of carrier density at T=283 K extracted from Figure 3.4.

3.3 Gain model result analysis

In this section, an analysis based on the gain model allows us to study and predict different aspects of the performance of InGaAsN lasers. First, the temperature behavior of differential gain dG/dN and transparency carrier density are extracted from the calculations, which is tested against published k*p simulation results. Following is the discussion on the influence of enhanced m_e* and excition effects on differential gain are presented. In this last section, gain compression due to the carrier heating effect is shown.

3.3.1 Temperature behavior of dG/dN and N_{tr}

Differential gain dG/dN as well as transparency carrier density N_{tr} as function of temperature are extracted from the calculation results at three temperatures(T=10 °C, 40 °C and 80 °C, respectively), as shown in Figure 3.6 and 3.7. In Figure 3.6, our results are tested against the results from k*p calculation [11], which states that a 0.5% of nitrogen incorporation leads to a 25% decrease in dG/dN and ascribes it to the increase of electron effective mass. From our results, we also notice that both InGaAs and InGaAsN show a similar trend in dG/dN and N_{tr} with temperature, i.e as temperature increases, dG/dN decreases and N_{tr} increases. This temperature behavior can be explained by the temperature variation of the bandgap energy and quasi-Fermi levels.

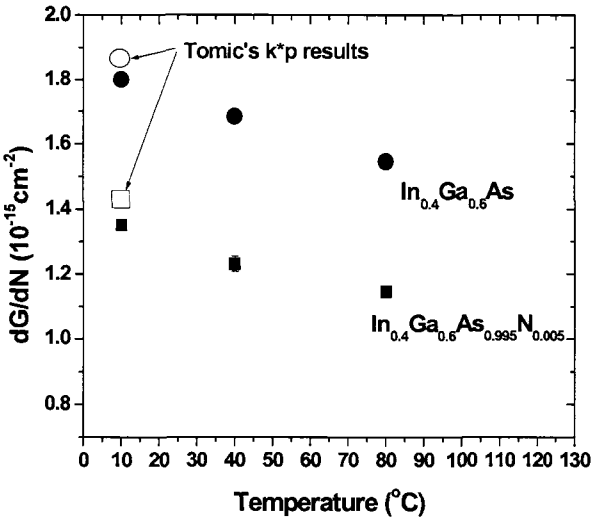

Figure 3.6 The intrinsic differential gain dG/dN as function of temperature for InGaAs (solid circle) and InGaAsN (solid square) QW, testing against Tomic's k*p simulation results.

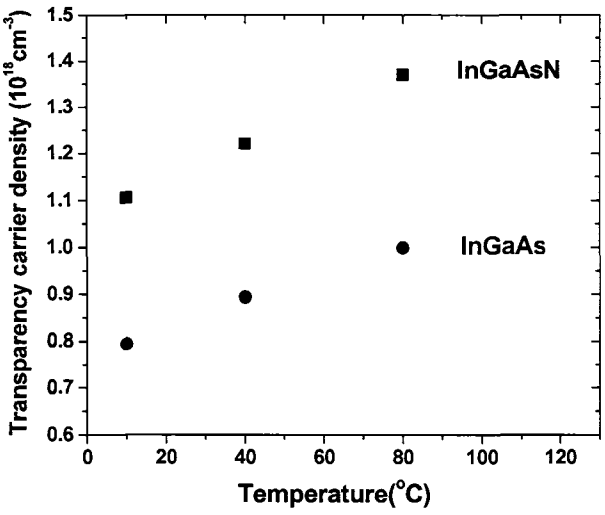

Figure 3.7 The transparency carrier density N_{tr} as function of temperature for InGaAs (solid circle) and InGaAsN (solid square) QW.

3.3.2 The effect of enhanced m_e*

So far, our gain model based on the parabolic E-k dispersion relationship has been tested against the published k*p simulation of reference 11, which ascribe the decrease in dG/dN with nitrogen incorporation to the increase of electron effective mass m_e*. However, a more recent analysis has shown that [12] the k*p model using different band structure actually yield different change in dG/dN, as shown in Figure 3.8. In all those different k*p models, an increased electron effective mass m_e* is employed, indicating the increase of m_e* might not be the factor that leads to a decrease of dG/dN.

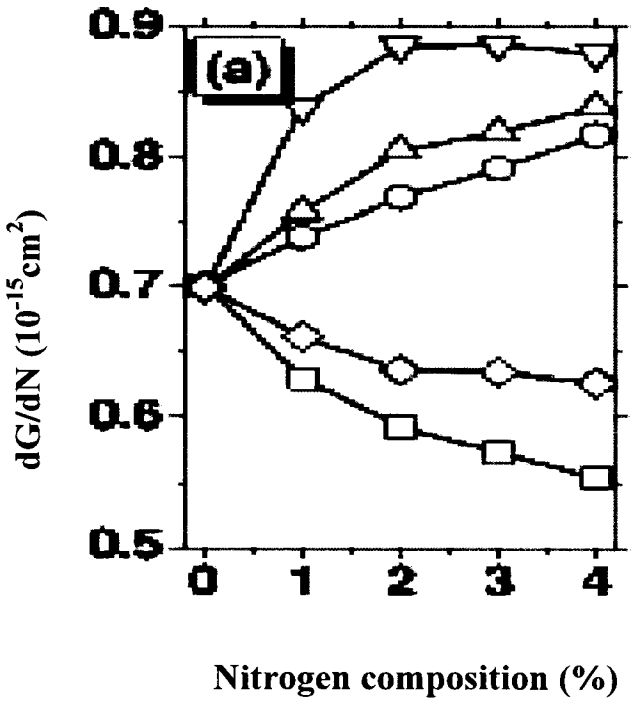

Figure 3.8 Dependence of differential gain dG/dN of a 7 nm $In_{0.35}Ga_{0.65}As_{1-y}N_y$ /GaAs quantum well on nitrogen composition for various k*p models considered in ref [12].

Therefore, we look into our gain model and try to inspect how m_e* affects dG/dN and why the k*p models using different band structure can lead to different results. As seen in the expression of gain in Eq. (3.34), the effect of m_e* on gain is mainly reflected on the effect of momentum matrix element $M_{m,n}$ and quasi-Fermi levels. The former is, as mentioned in section 3.2.1, not only determined by m_e*, but also affected by the choice of ϕ_n and g_m, which will bring up uncertainty in theoretical calculation of $M_{m,n}$. By letting $M_{m,n}$ remain unchanged with nitrogen incorporation, we evaluate the effect of quasi-Fermi

level on dG/dN. The result of this analysis is shown in Figure 3.9. Notice that a 30% enhancement in dG/dN is obtained in InGaAsN QW with m_e^*(InGaAsN)=0.083m_0. This actually makes sense because the larger m_e^* would allow the quasi-Fermi levels to separate more symmetrically into the bands, therefore having a positive impact on the dG/dN. We therefore attribute on the uncertainty in dG/dN to that of M_{nm}. An enhanced electron effective mass has positive impact on dG/dN, that is, the decreased dG/dN in reference 8 can not be ascribed to m_e^*. These findings are supported by recent experimental results that a similar intrinsic dG/dN was obtained after incorporation of nitrogen [13][14]

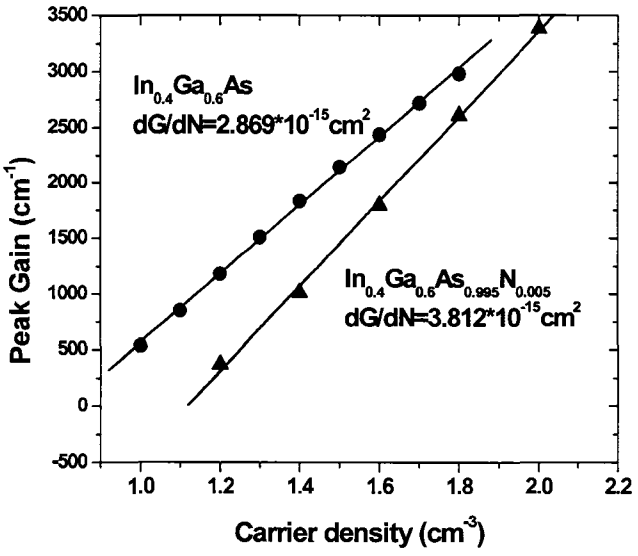

Figure 3.9 Peak gain as function of carrier density. The impact of enhanced m_e^*due to nitrogen incorporation is only reflected on the quasi-Fermi level while M_{nm} is set unchanged.

3.3.3 The effect of exciton on gain and differential gain

Up to now, the previous approaches in the gain model are all based on the assumption that the carriers only consist of free electrons and holes. Later in chapter 4, a lineshape model analysis is carried out on a set of PL spectra with low excitation intensity to study thermal ionization of excitons as function of temperature. In this model the PL spectrum is assumed to be a superposition of both excitonic and free carrier recombination. From the results, it is found that as temperature raises, the relative contribution of exciton to the emission peak decreases, while the free carrier's contribution increases. But at room temperature excitonic recombination is still present, representing 49% (24%) of the total emission in InGaAs and InGaAsN respectively [7]. Therefore, it is necessary to incorporate the existence of excitons in our gain model.

For the exciton gain model, the only different treatment is that, in contrast to a separate electron and hole quasi-Fermi level calculation, the expression of the quasi-Fermi level for heavy hole does not follow Fermi-Dirac statistics, but follow the electron distribution, i.e the distribution function for both electrons and holes are the same, $f_c=1-f_v$. Therefore, the inversion factor f_c-f_v in Eq. (3.34) becomes $2f_c-1$, resulting in an increased band filling effect of the hole state. The revised optical gain spectrum for QW structure with pure exciton as carriers is:

$$g(N,E) = \sum_{m,n} C_0(E)\frac{2}{L_z}\int_0^{\infty} M_{m,n}(k)\frac{\frac{\gamma_k}{\pi}}{(E_{cv}(k)-E)^2+\gamma_k^{\,2}}(2f_c(N,k)-1)\frac{k}{2\pi}dk \qquad (3.48)$$

Figure 3.10 gives the calculation results of peak gain versus carrier density for extreme cases where carriers are either pure excitons or pure free carriers. We find that for the same carrier density, the existence of exciton enhances the peak gain, for both InGaAs and InGaAsN QW lasers. However, the differential gain does not increase as much in dilute nitride laser as in nitrogen free lasers. This is not surprising if we consider that the increased m_e^* in dilute nitride laser leads to a slower increase in band filling of hole state in the excitonic dominated gain.

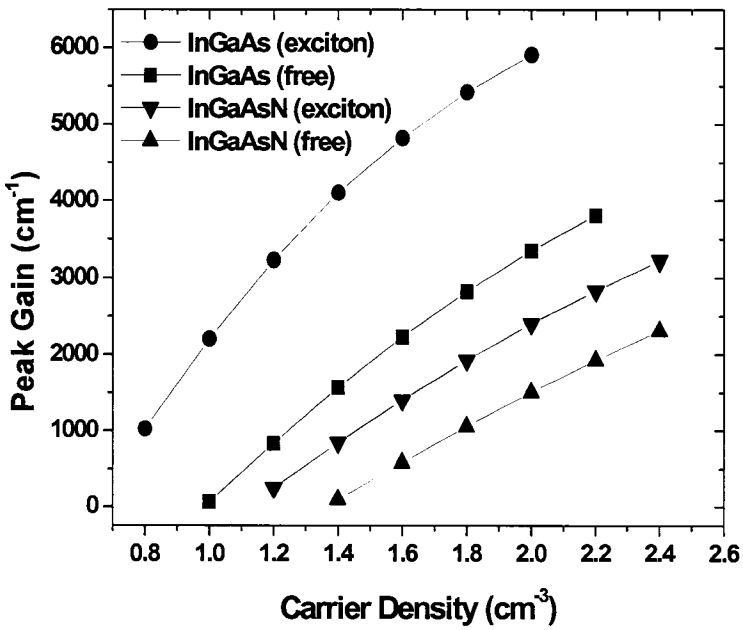

Figure 3. 10 Peak gain as function of carrier densities for pure exciton content and pure free carrier content. The calculation is carried out for both InGaAsN and InGaAs lasers at T=283 K.

3.3.4 The effect of carrier heating on gain compression

In this section, we intend to utilize our gain model to demonstrate the effect of carrier heating on gain compression ε, which is a main factor that limits the high speed performance of laser diode. Usually after an initial transition, the carrier distribution is heated up to a temperature higher than the lattice temperature T_0. Strong carrier-carrier and carrier-phonon interaction bring the carrier distribution to reach equilibrium with the lattice after so called gain compression relaxation time [15]. Here we treat the carrier heating as an quasi-equilibrium process in order to investigate the effect of the heated temperature on gain. Figure 3.11 illustrate the gain spectra for the same carrier density, but with different temperature. It is noted that higher temperature not only brings the gain peak to lower energy (red shift of band gap), but also compresses the gain.

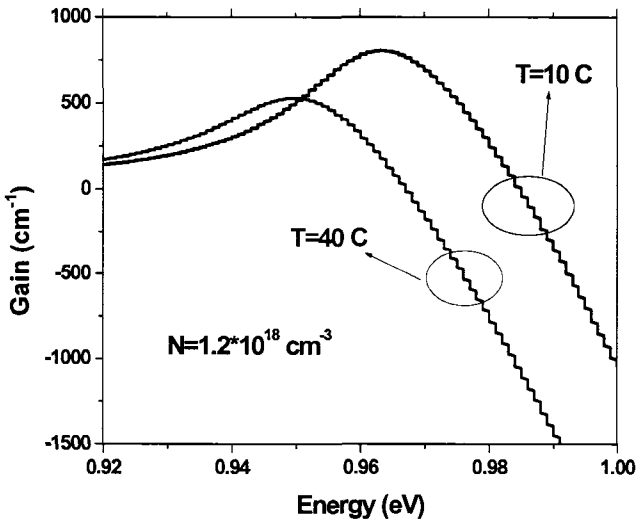

Figure 3.11 Modal gain for different carrier temperature as function of photon energy. The model is used for InGaAs/GaAs laser diode, carrier density $N=1.2\times10^{18}$ cm^{-3}.

3.4 Chapter summary

In this chapter, in order to investigate the impact of nitrogen incorporation we have built an analytical model based on the assumption of parabolic E-k dispersion relationship. Testing against the k*p simulation, the intrinsic differential gain dG/dN, transparency carrier density N_{tr} as function of temperature for both nitrogen and nitrogen free QW are retrieved through the analysis of the results from the model. A climbing N_{tr} and a descending dG/dN with temperature are observed for both InGaAs and InGaAsN QW. The introduction of nitrogen into InGaAs leads to an increase of N_{tr} by about 40%, and we ascribe this behavior to the enhancement of the electron effective mass m_e*. While a 25% decrease in dG/dN is obtained from our model, a 30% enhancement in dG/dN is observed in the InGaAsN QW if only the effect of quasi-Fermi level due to the increased m_e* is considered. This allows us to evaluate that an enhanced electron effective mass actually has a positive impact on dG/dN while the uncertainty of calculated $M_{m,n}$ in k*p simulation leads to the discrepancy in the prediction of real dG/dN in current theoretical models. Therefore, further efforts in the k*p theoretical modeling is needed.

The analysis based on the gain model also allow us to study and predict different aspects of material and laser performance of InGaAsN laser, such as excitonic effect and carrier heating effect. The former shows a positive effect on gain and differential gain, while the latter, compress the gain and thus deteriorate high speed performance of laser diodes.

Reference:

[1] L.A.Coldren and S.W.Corzine, *Diode lasers and Photonic Integrated Circuits*: Wiley series in microwave and optical engineering, 1995

[2] R.J.Potter, N.Balkan, X.Marie, H.Carrere, E. Bedel and G.Lacoste G , "Interaction strength between the highly localised nitrogen states and the extended semiconductor matrix states in GaInNAs", PHYSICA STATUS SOLIDI A-APPLIED RESEARCH **187** (2): 623-632 (2001).

[3] I. Vurgaftman, J. R. Meyer, and L. R. Ram-Mohan, "Band parameters for III-V compound semiconductors and their alloys ",JOURNAL OF APPLIED PHYSICS **89** (11): 5815-5875 Part 1, (2001).

[4] W.W.Chow, E.D. Jones, N.A.Modine, A.A.Allerman and S.R.Kurtz "Laser gain and threshold properties in compressive-strained and lattice-matched GaInNAs/GaAs quantum wells", APPLIED PHYSICS LETTERS **75** (19): 2891-2893 NOV 8 (1999).

[5] Wu J, Shan W, Walukiewicz W, "Band anticrossing in highly mismatched III-V semiconductor alloys", SEMICONDUCTOR SCIENCE AND TECHNOLOGY **17** (8): 860-869 AUG (2002).

[6] Duboz JY, Gupta JA, Z.R.Wasilewski, J.Ramsey, R.L.Williams, G.C.Aers, B.J.Riel and G.I. Sproule, "Band-gap energy of $In_xGa_{1-x}N_yAs_{1-y}$ as a function of N content", PHYSICAL REVIEW B **66** (8): Art. No. 085313 AUG 15 (2002).

[7] L. F. Xu, D. Patel and C.S.Menoni, J.Y. Yeh, L. J. Mawst, Nelson Tansu, *Applied Physics Letters* **89** (17): Art. No. 171112 OCT 23 (2006).

[8] Tansu N, Mawst L, "Current injection efficiency of InGaAsN quantum-well lasers" JOURNAL OF APPLIED PHYSICS **97** (5): Art. No. 054502 (2005).

[9] K.P.O'Donnell, X.Chen, "Temperature-dependence of semiconductor band-gaps" APPLIED PHYSICS LETTERS **58**(25): 2924-2926 JUN 24 (1991).

[10] S.L. Chuang, *Physics of optoelectronic devices:* Wiley (New York), 1995.

[11] S.Tomic, E.P.O'Reilly, R. Fehse, S.J.Sweeney, A.R. Adams, A.D. Andreev, S.A. Choulis, T.J.C.Hosea and H.Riechert, "Theoretical and experimental analysis of 1.3-mu m InGaAsN/GaAs lasers", IEEE JOURNAL OF SELECTED TOPICS IN QUANTUM ELECTRONICS **9** (5): 1228-1238 SEP-OCT (2003).

[12] S. T. Ng, W. J. Fan, Y. X. Dang, and S. F. Yoon, "Comparison of electronic band structure and optical transparency conditions of $In_xGa_{1-x}As_{1-y}N_y/GaAs$ quantum wells calculated by 10-band, 8-band, and 6-band k center dot p models", PHYSICAL REVIEW B **72**, 115341 (2005).

[13] D. J. Palmer, P. M. Smowton, P. Blood, J. Y. Yeh, L. J. Mawst, and N. Tansu,"Effect of nitrogen on gain and efficiency in InGaAsN quantum-well lasers," APPLIED PHYSICS LETTERS, vol. **86** (7), Art. No. 071121, (2005).

[14] O. Anton, L.F. Xu, D. Patel, and C.S. Menoni, etc, "The intrinsic frequency response of SQW-MOCVD 1.3μm InGaAsN lasers in the range T=10-80°C", IEEE PHOTONICS TECHNOLOGY LETTERS **18** (13-16): 1774-1776 (2006).

[15] W.Z. Lin, R.W. Schoenlein, J.G. Fujimoto and E.P. Ippen, "Femtosecond absorption saturation studies of hot carriers in GaAs and AlGaAs", IEEE JOURNAL OF QUANTUM ELECTRONICS **24**: 267 (1988).

CHAPTER 4

Carrier recombination in InGaAsN QW

This chapter is devoted to understand the influence of 0.5% nitrogen incorporation on the emission efficiency and carrier recombination dynamics of InGaAsN/GaAs QW. We do this through a comprehensive study of the spectrally and temporarily resolved photoluminescence (PL) in the temperature range of 10-300 K. The analysis of the results provide insight on carrier localization effects, the nature of the electron and hole states that participate in the emission and their recombination dynamics. The analysis of the photoluminescence spectra at temperatures above where localization occurs allows determining the exciton binding energy. This analysis coupled with a 2-D model enables the determination of the electron effective mass, m_e^*.

4.1 Investigation of carrier recombination through time integrated photoluminescence

Time integrated photoluminescence (PL) was excited by a mode-locked Ti:Sapphire pulse laser. With an excitation wavelength of 800nm, most of the photoexcited carriers are generated within GaAs barrier, and then captured into the well. Typical excitation intensities in these experiments are ~ 50 W/cm^2, which converts to an excitation carrier density of ~ 1×10^{12}cm^{-2}. This carrier density is comparable to that of device when operating close to threshold. Figure 4.1 shows typical temperature dependence of the normalized PL spectra for both InGaAsN and InGaAs QW.

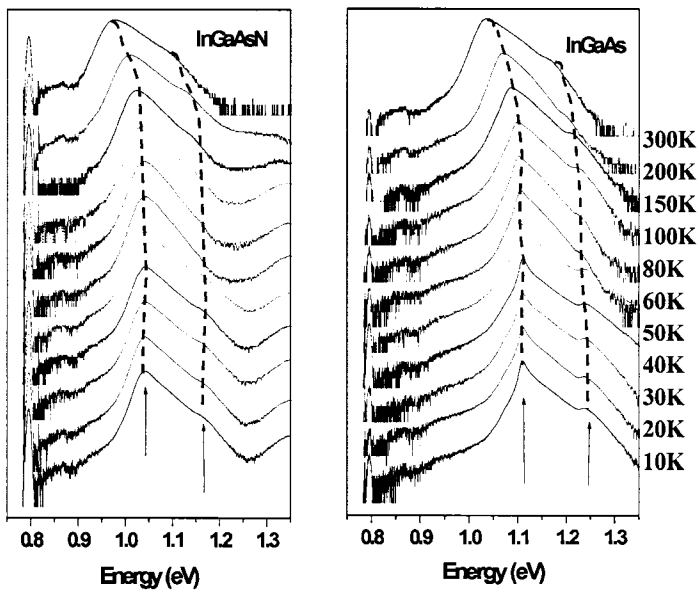

Figure 4.1 Temperature dependence of the time integrated PL spectrum in logarithmic scale, with an excitation intensity of 50 W/cm^2.

Two luminescence features are observed under high excitation intensity, a low energy feature ascribed to the ground state of QW transition. The PL peak energy for both transitions versus temperature is guided to the eye by a dashed line in Figure 4.1.

We first investigate the temperature dependence of the lower energy PL peak energy, plotted in Figure 4.2. Note that for temperatures higher than 80K, the PL peak exhibits a similar behavior with temperature in both samples. This behavior reflects the temperature dependence of band gap energy $E_g(T)$, known as

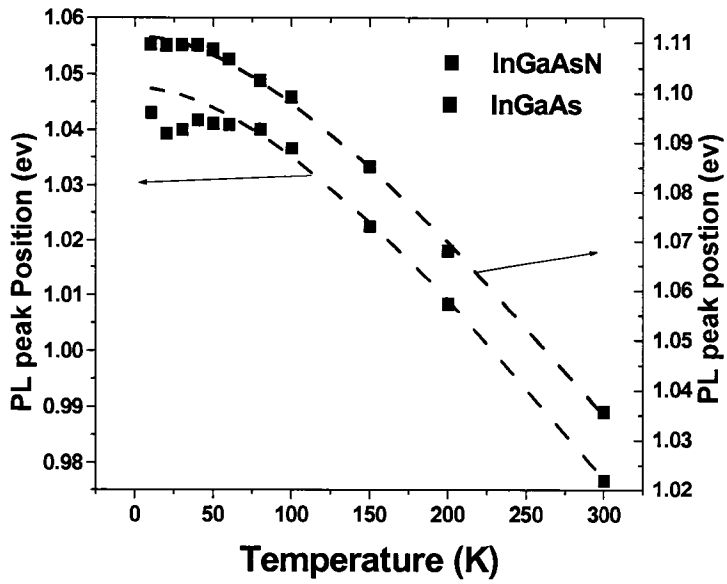

Figure 4. 2. Temperature dependence of lower energy PL peak energy positions for both InGaAsN and InGaAs samples. The dashed lines are the fitting results to Vashni equation.

the Varshni equation [1] $E(T) = E(0) - \frac{\alpha T^2}{T + \beta}$, where T is the absolute

temperature, and α and β are constants . The temperature dependence of the lower energy PL peak energy for both samples is fitted to this equation. α and β values of $4.7X10^{-4}$ eV/K and 253.707 K were obtained for InGaAsN. Similarly, α and β values of $4.3X10^{-4}$ eV/K and 247.42 K were obtained for InGaAs. The fitted curves are shown in Figure 4.2 by the dashed lines. These results show that the lower energy PL peak of InGaAsN at T>80K is dominated by the near band-edge e1-hh1 transition and the temperature coefficient of band-edge of InGaAsN is comparable to that of InGaAs. While the trace of InGaAs at low temperature still matches the extrapolation of the Varshni equation, in InGaAsN. The Varshni-like behavior is only observed above ~80K. At lower temperatures, the S-shape behavior, already documented in the literature, and associated with the trapping and detrapping of excitons to localized excitonic states [2], is observed.

To diagnose the origin of the localized states, PL spectra excited by a cw λ=980 nm diode laser were measured. In this case the photoexcited carriers are only generated within the quantum well active region. Figure 4.3 shows typical PL spectra at 50K. A remarkable difference is observed between the N free and dilute N sample. First of all, the PL spectrum for InGaAsN exhibits a much broader width compared with its host matrix InGaAs. Secondly the InGaAsN PL shows a low-energy tail, together with a steeper higher energy edge. These features suggest a distribution of localization states with an exponential-like density of states on the lower energy side in both as-grown and annealed InGaAsN QW. We can usually estimate the localization potential Δ by fitting the low energy tail with Eq. (4.1)[3]:

$$\rho(E) \propto e^{-E/\Delta} \tag{4.1}$$

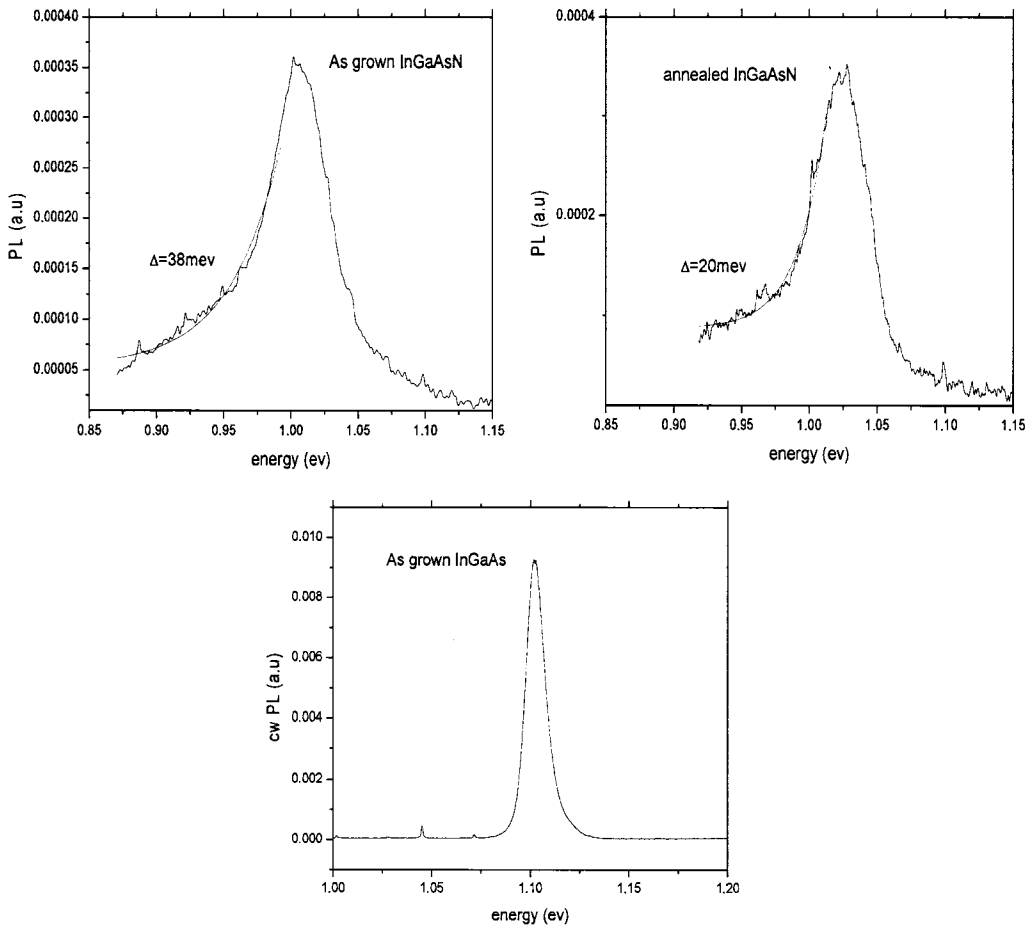

Figure 4.3 Cw photoluminescence spectra obtained with λ=980 nm excitation at T=50 K for (a) as grown InGaAsN, (b) annealed InGaAsN and (c)InGaAs SQW.

At T=50K, the localization potential is fitted approximately to be 38 meV for as grown InGaAsN and drops to 20meV after annealing, indicating that annealing can smear some shallow localized states. No obvious exponential lower

energy tail was observed in InGaAs QW, which means there are almost no localization centers.

In III-V ternary and quaternary semiconductor alloys, the carrier localization is caused by potential fluctuations of the conduction/valence bands, due to a random distribution of the group III and V elements on respective lattice sites. This random distribution of group III and V atoms has negative influence on the optical quality of the samples: it causes inhomogeneous broadening of the photoluminescence (PL). This effect may be accentuated in quantum wells due to strain and has negative impact on the laser characteristics.

In our case, the narrow PL width and absence of localization observed in InGaAs QWs indicates a good optical quality of the host matrix and also suggests that localization effects and the poorer optical quality in InGaAsN QW may be accentuated by the instability of nitrogen incorporation during growth. Actually this is one of the challenges of the technology to control the homogeneity of InGaAsN quantum wells in order to obtain small inhomogeneous broadening of the photoluminescence.

4.2 Analysis of the main features in the photoluminescence

The photoluminescence was measured under different excitation intensity, i.e from 0.5-100 W/cm^2, with corresponding excitation carrier density varying from $1\times10^{10}\,cm^{-2}$ to $2\times10^{12}cm^{-2}$. Figure 4.4 shows typical spectra. It is seen that

as the excitation intensity decreases, the higher energy shoulder also decreases and tends to disappear at low excitation intensity.

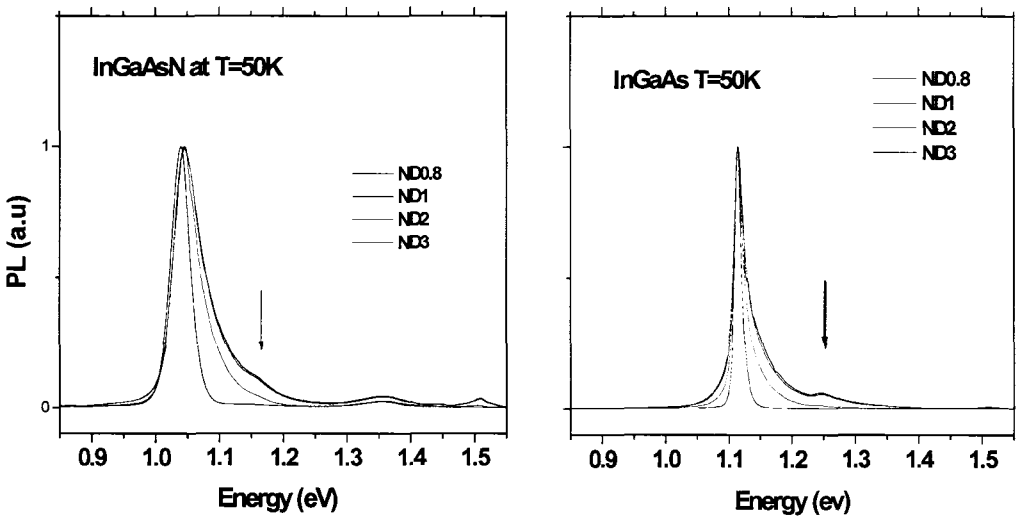

Figure 4. 4 Photoluminescence spectra under different excitation intensity from 0.5-100 W/cm^2 at T=50K for both InGaAsN and InGaAs QW.

To univocally characterize the additional PL emission at the higher energy side of the spectra in both InGaAsN and InGaAs sample, polarization dependent photocurrent (PC) measurements of broad area laser devices were carried out at room temperature. In these measurements, the samples were illuminated from the edge. The results are shown in Figure 4.5, where the corresponding photoluminescence spectrum is also shown. Under TE polarization, when the incident light is parallel to the junction, the band-edge transition e1-hh1 is clearly visible and the higher energy emission is much weaker; Under TM polarization, when the light is parallel to the growth direction, the higher energy emission band

becomes dominant and the fundamental transition e1-hh1 is considerably reduced but not completely quenched. An 84- kV/cm built-in field due to the doping in the cladding layer may contribute to QW symmetry breaking such that the e1-hh1 transition does not totally disappear under TM polarization. Thus, it is safe to assign the higher energy emission as e1-lh1 transition, and its appearance of this transition in PL spectra is due to band-filling effect. In contrast with model calculations that predict that due to the large strain in the QW, the hole band structure consists of only heavy-hole subbands in the 2D states, with light-hole states having bulk-like (3-D) properties [4], our polarization dependent photocurrent results show that the light-holes state has a 2-D character, indicating either partial strain relaxation, or larger valence band offset.

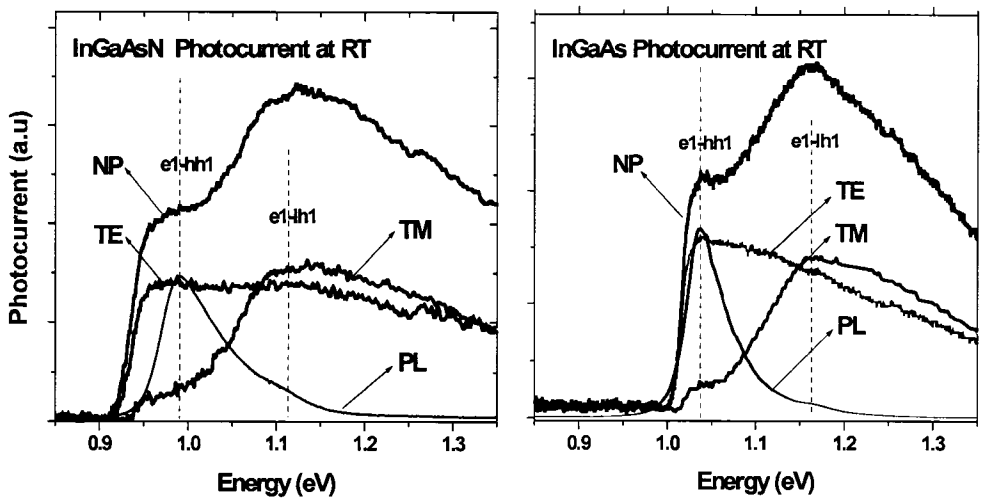

Figure 4. 5 Polarization dependent photocurrent measurement at RT reveals the origin for each feature in photoluminescence.

4.3 Exciton binding energy and electron effective mass

The electron effective mass m_e^* is one of the most important fundamental parameters of QW structures. However, to date no direct determination of the electron effective mass, m_e^*, has been reported for high indium content (~30%-40%) $In_xGa_{1-x}As_yN_{1-y-}$, due to the limitations imposed by the high strain in growing thick freestanding epilayers (typically ~1-3μm) or QWs with different thickness.

There are model calculations and a few experiments that have investigated the effect of nitrogen on the electron effective, m_e^*. From the modeling standpoint there are basically two approaches to predict m_e^*, the phenomenological relationship [5] and the band anti-crossing (BAC) model [6][7]. However, these two approaches yield quite different enhancement of m_e^* with nitrogen. The former predicts $m_e^*=0.069m_0$ while in the latter $m_e^*=0.083m_0$. The experiments, mainly conducted on low In-content alloys, report values of m_e^* ranging from 0.08 m_o to 0.12 m_o [8][9][10]. The large spread in the experimental results may arise from the method used to determine me*, which relies on the fitting of the optical transitions and requires knowledge of the band-offset ratio that is still relatively controversial.

In this work, the conduction band edge electron effective mass, m_e^*, for $In_{0.4}Ga_{0.6}As_{1-y}N_y/GaAs$ single QWs was obtained by using a fractional dimension model [11] to fit the exciton binding energy extracted from the lineshape analysis of the photoluminescence (PL) at different temperatures above 80 K. Here the PL

spectra were obtained at low excitation intensity. The procedure used to determine the exciton binding energy, elucidated in Figure 4.6 is as follows: 1) a detailed line shape analysis of PL spectra is carried out, This consists of fitting a superposition of exciton recombination and free carrier recombination, with a selected exciton binding energy R as input parameter. 2) The ratio between free carriers and excitons at a given temperature is obtained from the fit. 3) The ratio between the excitons and free carriers populations as function of temperature is evaluated with a two-dimensional law of mass action [12] and exciton binding energy is obtained; 4) Since the exciton binding energy is also a parameter used in the lineshape fitting of the PL spectra, a careful iteration was implemented to extract R that fits simultaneously the ratio between the excitons and free carriers populations and the PL spectra. Finally a fractional dimension method [11] is used to extract m_e^* from R.

To circumvent the complexity in lineshape fitting, we analyzed the PL data under relatively low excitation intensity, where only the e1-hh1 transition is observed and the contribution of e1-lh1 transition is negligible. Typical average excitation intensity absorbed by the sample was 0.5 W/cm^2. Assuming that each 1.55 eV photon generates one electron-hole pair, the corresponding photo-excited sheet carrier density equals 2×10^{10} cm^{-2}. The temperature dependent PL spectra for both samples are shown in Figure 4.7. Relevant features of the PL spectra are: (1) the broader linewidth of InGaAsN PL compared to InGaAs, and (2) the distinct change from Guassian-like to asymmetric lineshape induced by the

temperature increase in both samples. The latter suggests an increased contribution from free carrier recombination as temperature increases.

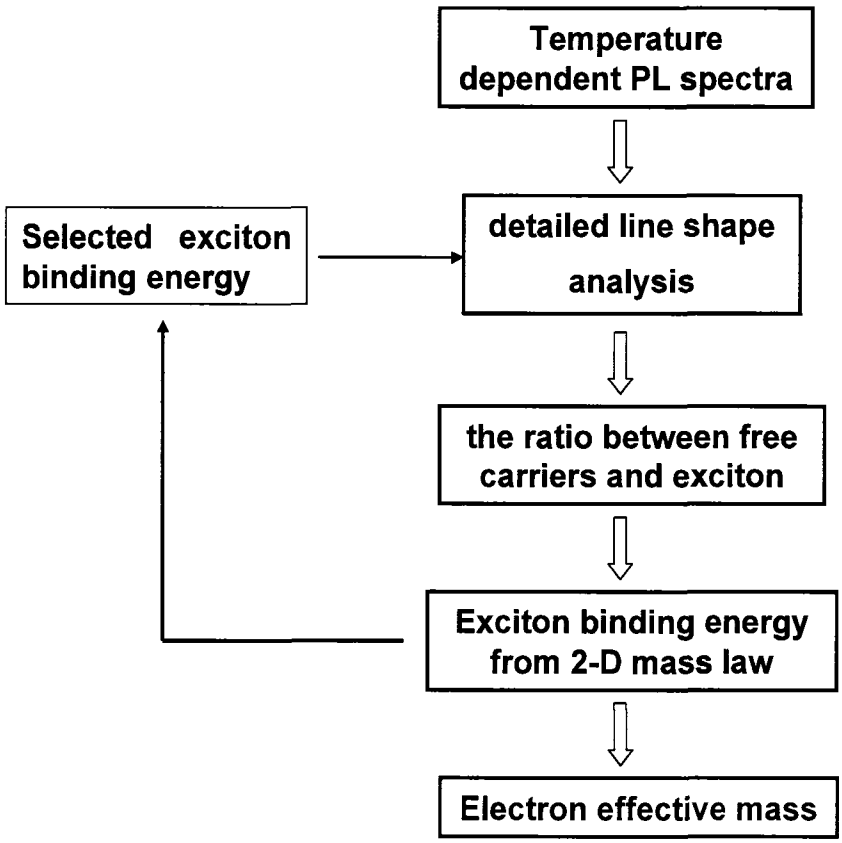

Figure 4.6 Flow diagram showing the optical method used to determine m_e^*.

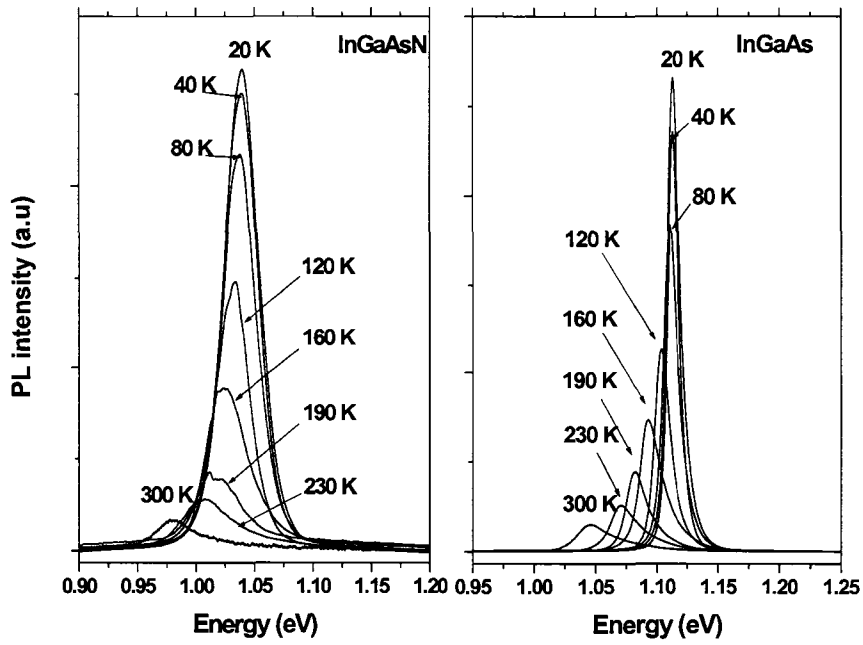

Figure 4. 7 PL spectra of InGaAs (right) and InGaAsN (left) at various temperature under an excitation intensity of 0.5 W/cm^2.

4.3.1 Exciton binding energy R

The data of Figure 4.7 were analyzed using a simple statistical model proposed in reference [13]. In this model the PL spectrum is assumed to be a superposition of excitonic and free carrier recombination. The exciton line can be reasonably taken into account by means of a Gaussian profile multiplied by the Fermi-Dirac statistical distribution function, as shown in Eq. (4.2). The free-carrier recombination term is modeled by an analytical expression that contains the contribution from high-k states. As shown in Eq. (4.3), this expression

incorporates a broadened step-like two-dimensional density of states multiplied by the Fermi-Dirac distribution of the free electrons and holes, and a two-dimensional Sommerfield factor that accounts for the Coulomb interaction between carriers. Thus, the PL emission intensity is the sum of Eq.(4.2) and Eq.(4.3):

$$I_x(E) = A_x \exp(-\frac{(E-E_H(T))^2}{2\sigma_H{}^2(T)}) \frac{1}{1+\exp(\frac{E-E_H(T)}{k_BT})}, \quad (4.2),$$

$$I_C(E) = A_C \frac{1}{1+\exp(-\frac{E-E_C(T)}{\sigma_C(T)})} \frac{2}{1+\exp(-2\pi\sqrt{\frac{R}{|E-E_C(T)|}})} \frac{1}{1+\exp(\frac{E-E_C(T)}{k_BT})} \quad (4.3),$$

where A_x (A_C), E_H (E_C) and σ_H (σ_C) are the amplitude, peak energy and broadening fitting parameters of the e_1-hh_1 exciton (free carrier) recombination, respectively. R is the binding energy of the exciton that needs to be determined, with $E_C = E_H + R$.

The fit of the PL spectra of InGaAs and InGaAsN single QWs with the sum of Eqs. (4.2) and (4.3), shown in Figure 4.8, describes satisfactorily the main features of the PL peaks. It can be seen that as temperature rises, the relative contribution of the exciton emission decreases, while that of free carriers increases.

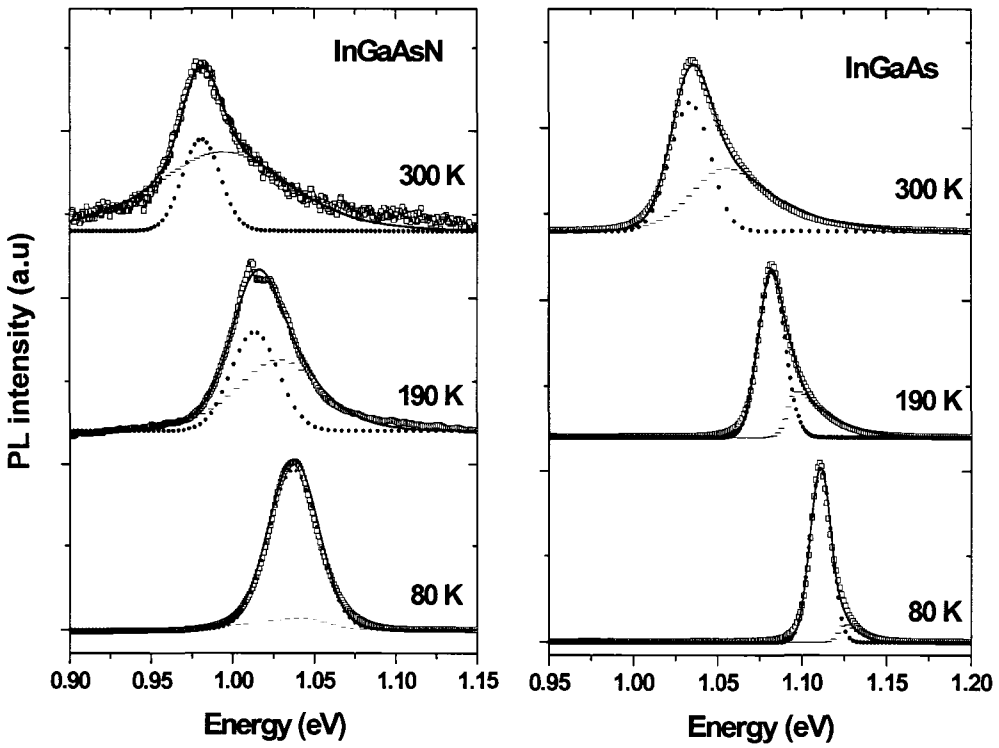

Figure 4.8 Fit (solid line) of the PL spectra lineshape normalized to peak (open circle) at different temperatures for InGaAs (right) and InGaAsN (left). The contributions from exciton recombination (dotted line) and free carrier recombination (dashed line) are shown in the graph.

The integrated exciton and free carrier area emission obtained from the fit were assumed to be proportional to the free exciton (N_x) and free carriers (N_e, N_h) populations respectively. This is the case when the recombination coefficient for both excitons and free carriers has the same temperature behavior [14]. Figure 4.9 depicts the semilogrithmic variation of the ratio of free carriers to exciton

populations, $\frac{N_e N_h}{N_x}\frac{1}{T}$, as function of $\frac{1}{k_B T}$. These traces show a linearity for both InGaAs and InGaAsN. Plotted in this format, the data of Figure 4.9 can be fitted with the two-dimensional law of mass action [12]:

$$\rho = \frac{N_e N_h}{N_x} \propto \frac{m_e m_h}{m_e + m_h}\frac{k_B T}{\pi\hbar^2} e^{-\frac{R}{k_B T}} \qquad (4.4),$$

to obtain from the slope of Figure 4.9 the exciton binding energy R. Implementing a careful iteration, R, that fits simultaneously the data of Figures 4.8 and Figure 4.9, is extracted.

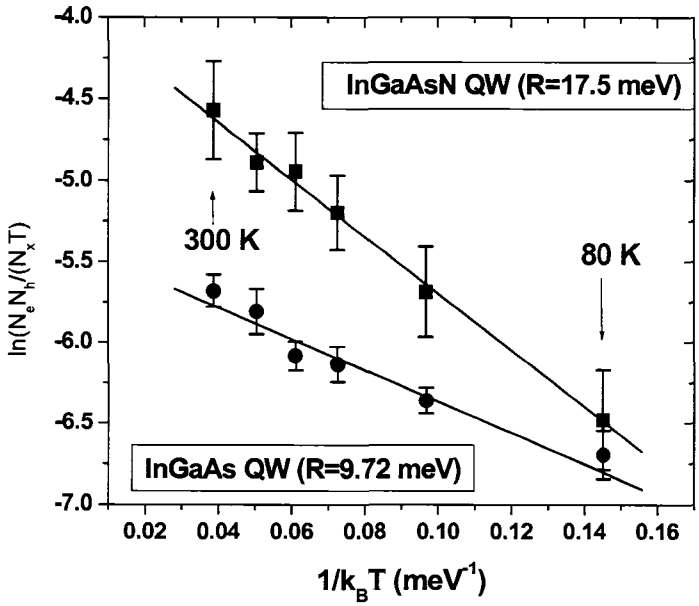

Figure 4. 9 Semilogarithmic plot of $N_eN_h/(N_xT)$ as function of $1/k_BT$ from both InGaAs and InGaAsN QW (symbols). The straight lines are the best fit to the experimental data using the 2-D mass law. The slope yields the exciton binding energy R indicated on the figure.

Based on this fitting procedure, R was determined to be 9.72±1.24 meV and 17.5±0.9 meV for InGaAs QW and InGaAsN QW, respectively.

4.3.2 Electron effective mass m_e*

The analysis just described was combined with a simple theoretical calculation based on a fractional dimension model proposed by ref [11], to obtain the electron effective mass m_e*. Within this framework, the ground state e1-hh1 exciton binding energy is given by:

$$R = (\frac{2}{\alpha - 1})^2 R_y \qquad (4.5),$$

where $R_y = (\frac{\varepsilon_0}{\varepsilon})^2 \frac{\mu}{m_0} R_H$ is the exciton Rydberg energy, expressed in terms of m_0, the free electron mass, μ the exciton reduced mass $\frac{1}{\mu} = \frac{1}{m_e^*} + \frac{1}{m_h^*}$ and R_H=13.6eV. Here the parameter α is a fractional dimension value, which varies between 2 and 3 in a real quantum-well structure. The values α=3 and α=2 give $R=R_y$ and $R=4R_y$, respectively, corresponding to the well-known results for bulk and 2-D infinite quantum well cases. Thus, solving for the exciton binding energy from Eq. (4.5) consists of defining the spatial dimension parameter α, which is expressed as:

$$\alpha = 3 - e^{-\overline{L_w}/2\overline{a_0}} \qquad (4.6),$$

Here $\overline{L_w}$ is the effective QW width, representing the spatial extension of the electron and hole wavefunctions which can be obtained by solving Schrödinger's equation. $\overline{a_0}$ is the effective Bohr radius, $\overline{a_0} = \frac{\varepsilon}{\varepsilon_0}\frac{m_0}{\overline{\mu}} a_H$ where $\overline{\mu}$ is the mean value of the three-dimensional reduced mass of the exciton, which is given by $\frac{1}{\overline{\mu}} = \frac{1}{\overline{m_e^*}} + \frac{\overline{\gamma_1}}{m_0}$. $\overline{\gamma_1}$ is the mean value of the Luttinger parameter, and $\overline{m_e^*}$ is the mean value of electron effective mass. All mean values of the parameters used here are positionally weighted across the GaAs heterostructure. .

Using Eqs. (4.5) and (4.6) we calculated m_e^* from the measured exciton binding energy R on the well-studied InGaAs/GaAs QW first. Using the parameters summarized in Table. 4.1 [4], the analysis yielded a fractional dimension parameter α = 2.248, and a band edge electron effective mass $m_e^*=(0.049\pm0.007)m_0$ which is in good agreement with the established value of $m_e^* =(0.047m_0)$ [15].

Similar calculations were carried out in InGaAsN using the band-offset ratio given in ref [4] and the parameters in table I. The fractional dimension parameter was found to be α = 2.199. The electron effective mass for InGaAsN was calculated to be $m_e^*=(0.11\pm0.015)m_0$, considering that the dielectric constant and hole effective mass m_h^* do not change sizably upon the incorporation of nitrogen.

Table 4.1 Parameters for the calculation of electron effective mass at band edge.

Material	$In_{0.4}Ga_{0.6}As$	$In_{0.4}Ga_{0.6}As_{0.995}N_{0.005}$	GaAs Barrier
Heavy hole mass m_{hh}*	$0.457m_0$	$0.457m_0$	$0.51m_0$
Well depth Conduction band	306 meV	451 meV	
Well depth Valence band	165 meV	99 meV	
Luttinger Parameter γ_1	12.188	12.188	6.98
Dielectric Constant ε	13.9	13.9	12.9

Notice that the value α=2.199 for the InGaAsN single QW is not significantly different from α = 2.248 obtained for the InGaAs QW, indicating that the band offset ratio does not strongly influence the calculation of the electron effective mass from the exciton binding energy. This larger value of m_e* is in reasonably good agreement with those reported [8][9][10]. Unlike these previous experiments which are heavily dependent on the knowledge of the band-offset ratio our method is proven to be less sensitive on the choice of band offset ratio, thus provides more reliable results.

4.3.3 Impact of enhanced m_e*

The intrinsic differential gain dG/dN is a very important parameter in that it determines the modulation speed of the device. Although a decrease in dG/dN

by 25% with 0.5% of nitrogen content has been predicted by model calculations and is ascribed to the increase in the electron effective mass m_e^* [7], the impact of the enhanced m_e^* on dG/dN is debated in reference [16]. First let's put the theoretical model calculation aside. Realizing that the differential gain depends on how quickly the band edge carrier density changes in response to changes in the quasi-Fermi levels, it is critical to bring both quasi-Fermi levels as close to the band edges as possible to improve dG/dN[17]. Larger m_e^* allows the quasi-Fermi levels to separate more symmetrically in the electron and hole wells, therefore it has a positive impact on dG/dN. Instead, the larger effective mass does affect the transparency carrier density N_{tr}, which is expected to be larger in InGaAsN.

Theoretically, we performed a gain spectra calculation described in chapter 3 to investigate the impact of an increased m_e^* on dG/dN. In the model, m_e^* affects dG/dN through the change in quasi-Fermi level and the change in momentum matrix element. The latter is, not only determined by the band-edge electron effective mass, but also determined by the chosen orbital function and thus its value is uncertain. Only considering the effect of quasi-Fermi level, the enhanced m_e^* has a positive influence on intrinsic dG/dN. As supported proof, recent experiments have revealed a similar intrinsic dG/dN after the incorporation of nitrogen. And the measured reduced effective differential gain after adding nitrogen is mainly attributed to the transport effect [18][19].

4.4 Carrier recombination dynamics study

Next a carrier dynamics study is carried out through time-resolved photoluminescence (TRPL) measurements, from which the carrier recombination paths after the pulsed carrier generation are obtained. Insight into the optical transitions and their dynamics is important in that it can shed light onto the understanding of the mechanism of efficient optical emission. Although there were works that have been done on the characterization of emission lines in steady state photoluminescence (PL) measurements [20][21], as of yet no complete work has been accomplished on the study of the corresponding recombination dynamics.

Our results show that a second recombination channel, which has been proved to be contribution from e1-lh1 transition in section 4.2, affects the carrier injection distribution and further possibly influence the device performance. Nonradiative recombination, mainly Auger, is also observed to be very important at room temperature in InGaAsN/GaAs QW.

4.4.1 Study of carrier dynamics from time resolved PL spectra using the up-conversion method

The time resolved spectra obtained from the upconversion experiments provided the means to investigate the carrier dynamics of the e1-hh1 and e1-lh1

transitions at early stages following photoexcitation. A sequence of spectra taken at different delays at T=25 K and T=300 K are shown in Figure 4.10.

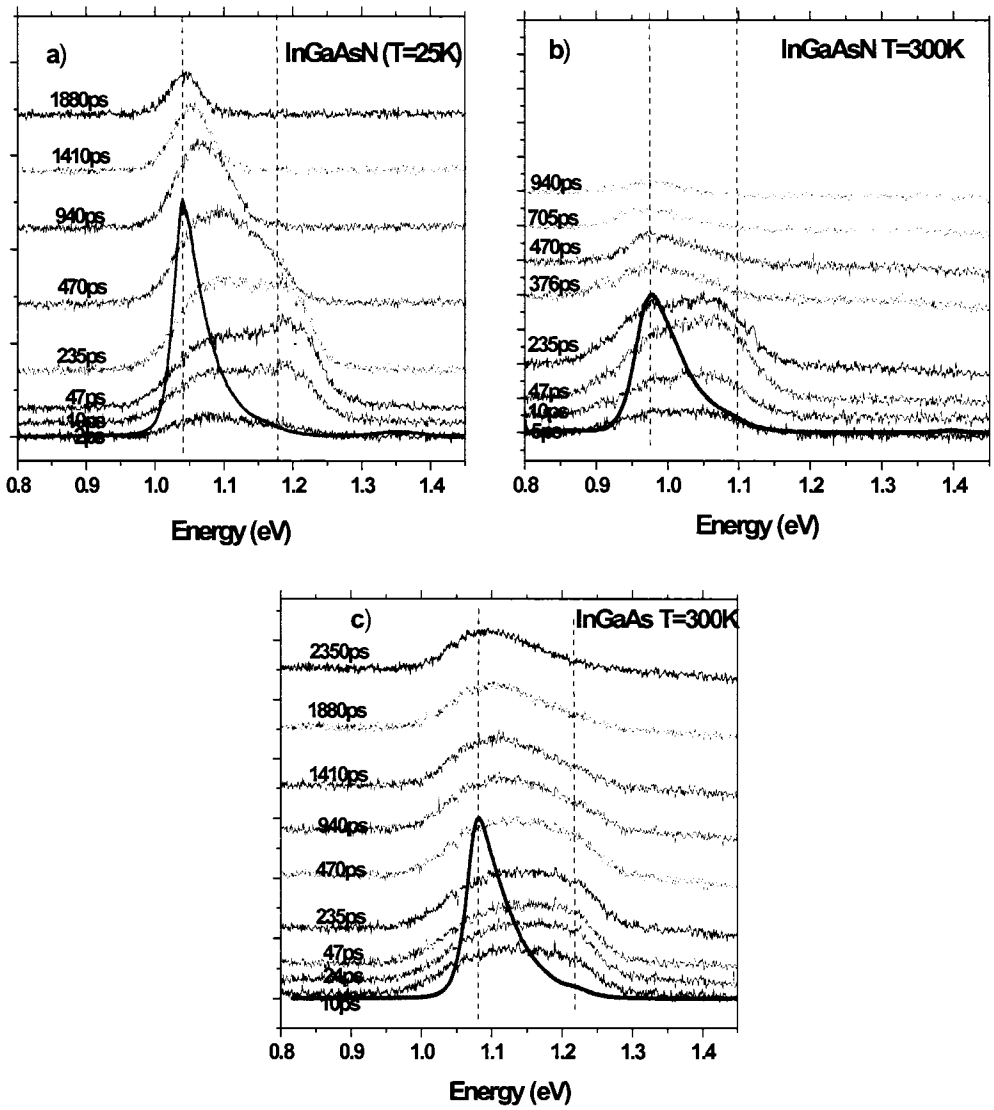

Figure 4.10 Temporarily resolved PL spectra at different time delays at T=25K and 300K. The dashed lines in the plots represent the energy location of e1-hh1 and e1-lh1 transitions observed in time integrated PL. The pump power into the sample was 30 mW.

At 25 K, the e1-hh1 PL emission in InGaAsN (Figure 4.10 (a)) shows a monotonous red shift of ~ 30 meV taking place in the first ~ 1.2 ns which is further evidence of carrier localization that is also described by the S-shape variation of the bandgap with temperature. This redshift decreases as temperature increases and is absent at room temperature (Figure 4.10 (b)). No localization effects are observed in InGaAs in the whole temperature range, coincident with the results shown in Figure 4.2. The energy position of the e1-hh1 transition of InGaAs as a function of time delay are also plotted in Figure 4.11.

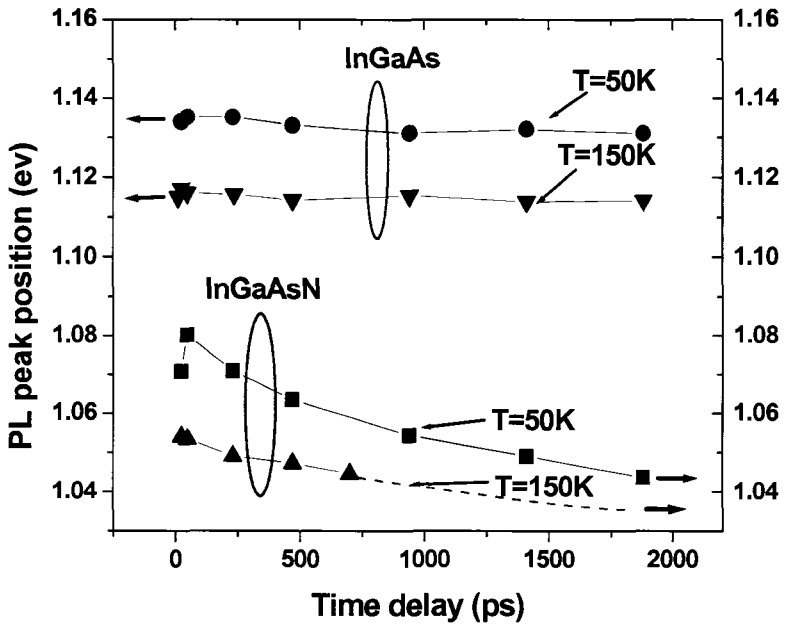

Figure 4.11. PL peak energy position from e1-hh1 as function of time delay after excitation for temperature 50K and 150K .

The dynamics of the PL spectra shown in Figure 4.10 also reveals that the higher energy e1-lh1 transition in InGaAsN, which is dominant at early stages of carrier recombination, is characterized by a shorter lifetime, ~ 600 ps (~300 ps) versus ~2000 ps (~700 ps) for the e1-hh1 transition at 25 (300) K, respectively. This is not surprising, as the light hole band in InGaAsN is barely confined, and its dynamics is affected by hole leakage to the barriers. Instead in InGaAs QW (Figure 4.10 (c)), the e1-lh1 emission lifetime is relatively long, ~1500 ps compared to ~2000 ps for e1-hh1 transition at room temperature, suggesting a better confinement of the light hole state.

4.4.2 Analysis of the PL lifetime

Purpose of the analysis presented here is to gain understanding of nonradiative and radiative recombination processes from the temperature dependence of the PL lifetime. As described in Chapter 2, we measured the lifetime by using an up-conversion technique. In the set up of this measurement, the CCD in Figure 2.4 is replaced by a high gain photo multiplier tube (PMT) and a 100μm width slit is added at the output of the spectrometer. The photoluminescence decay is recorded at different energy positions in PL spectra and both the rise time and decay time are analyzed. The rise time reflects how fast the carriers get captured into the states from where they recombine. Three different processes account for the decay: radiative, nonradiative recombination and carrier transfer. Figure 4.12 plots the transient luminescence at 50K for both

samples, for the case of strong pumping: $n=1\times10^{12}cm^{-2}$. It is noticed that the luminescence decay decreases with decreasing energy, and a convex shape instead of a single exponential decay appears at the early stages of time delay as energy decreases. This can be explained as a competition between carrier recombination and carrier transfer from a higher energy state. However, we still utilize a single exponential constant to fit the decay. The carrier lifetime is obtained by fitting the data of Figure 4.12 at a longer time delay for a lower energy, where the effect of carrier transfer is assumed to be negligible.

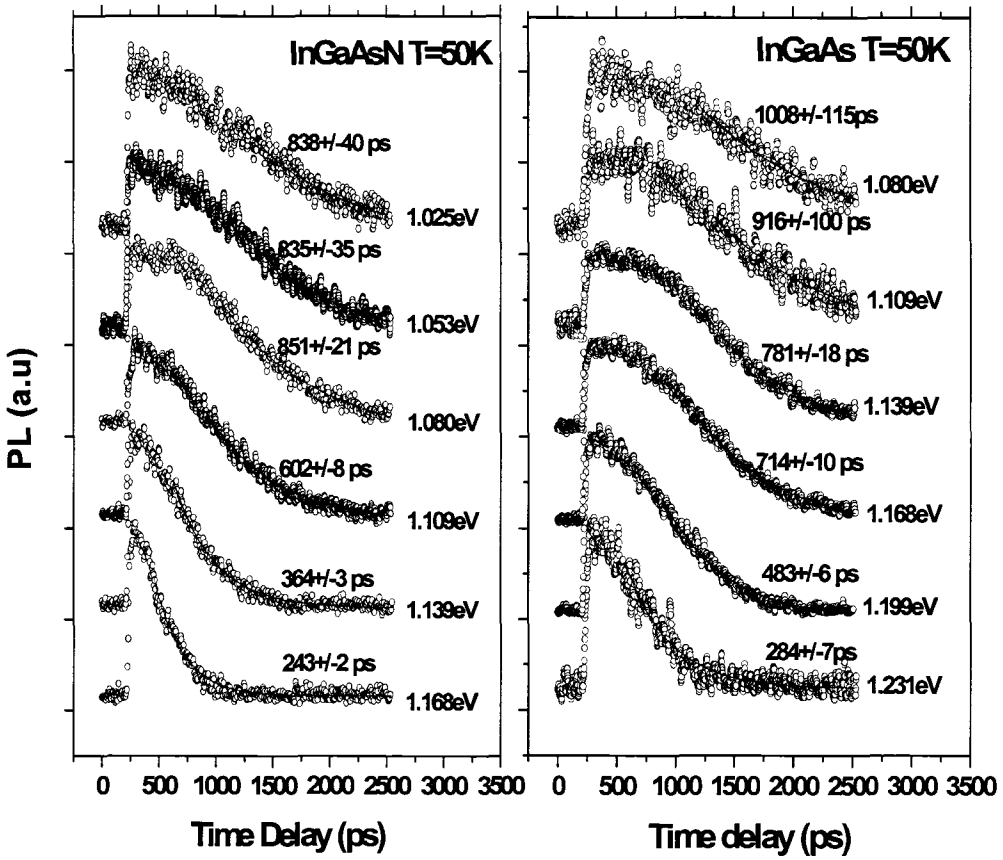

Figure 4.12 Time resolved PL measured at different photon energies (circles) at T=50K. Photoexcited carrier density=$1\times10^{12}cm^{-2}$. The single exponential decay fitting is shown by the solid line. The intensity is normalized and a baseline is added to the spectrum for clarity

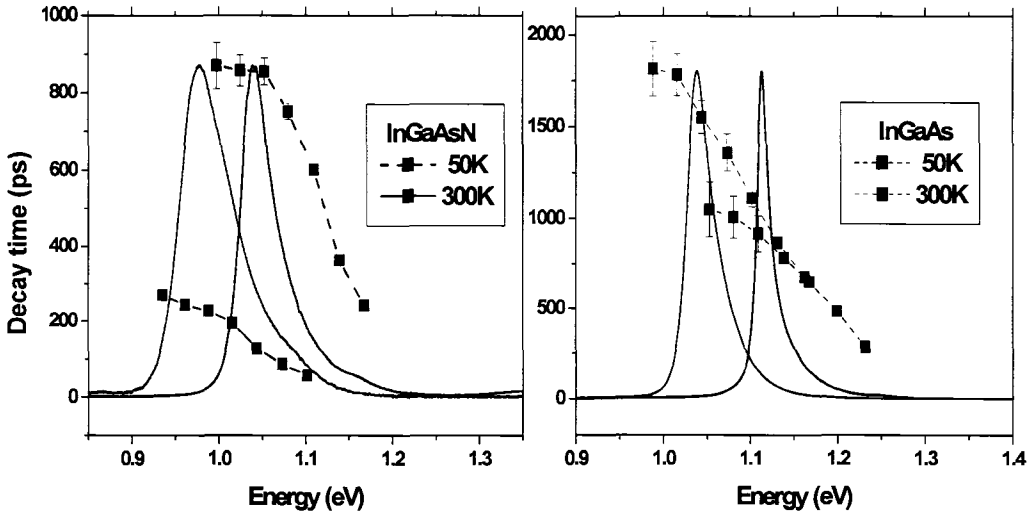

Figure 4. 13 Dependence of the PL decay time on the detection energy for the both InGaAsN and InGaAs QW at 50K and 300K together with the corresponding time-integrated luminescence spectra

The fitted lifetimes for energies across the entire luminescence band are given in Figure 4.13, together with the representative time-integrated PL spectra for two temperature 50K and 300K. As can be seen, for both temperatures the luminescence decay time increases towards decreasing energy, for both InGaAs and InGaAsN, however, there is a marked difference between the lifetime behaviors with temperature. In InGaAs the lifetime increases by a factor of 2 while in InGaAsN QW it decreases by a factor of 3 as temperature increases from 50K to 300K. The huge decrease of carrier lifetime in InGaAsN QW indicates the dominance of a nonradiative recombination at room temperature. The dominance

of non-radiative recombination at room temperature is a key factor in affecting the threshold current of laser device.

The rise time is also obtained by fitting the PL decay data and is measured to be about 10ps at 50K, remaining constant with energy within the experimental accuracy, as shown in Figure 4.14. As temperature increases to 300K, the average rise time increases to 12ps. However the increase is not significant considering the change of temperature from 50K to 300K.

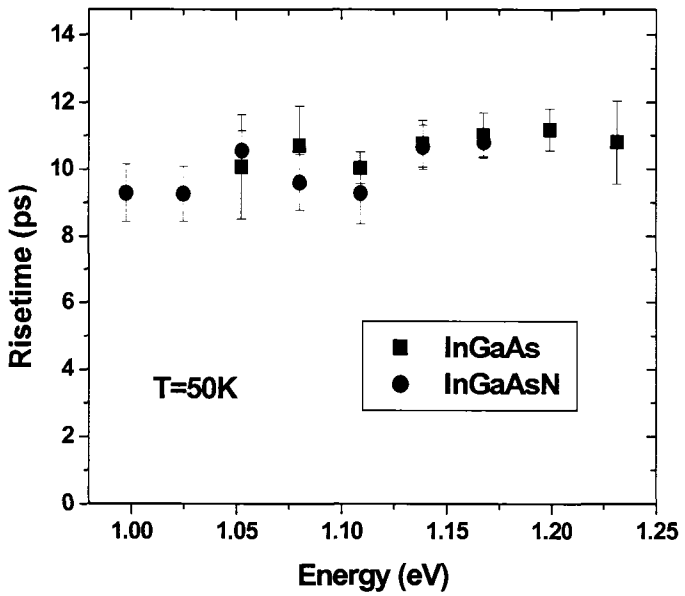

Figure 4. 14 Rise times of the luminescence measured at different energy positions in the PL spectra for both samples at T=50K.

It would be interesting to track the variation of the luminescence intensity decay within the whole temperature range. However, the up-conversion method is

limited to short time delays, ~ 2 ns, mainly due to the mechanical translation length of the delay stepper. As we can see in Figure 4.12, at the low energy side the time range that we can use to fit the decay is very short, and thus the fitted decay constant is very sensitive to the choice of the fitting range, furthermore, the intensity of the signal is quite weak at these long time delay.

As a complementary method, we measured the luminescence lifetime directly using a 12 GHz bandwidth InGaAs detector and a 25 ps rise time sampling oscilloscope. The time resolution of this measurement is thus determined by the system response time (~35ps), which is still reasonable to measure lifetimes longer than several hundreds of picoseconds. The time interval, 12ns, is only limited by the repetition rate of the Ti-sapphire laser. Although this measurement is not spectrally resolved, it reflects the maximum decay constant. From Figures 4.10 and 4.13, at long delay times the luminescence is mainly the contributions of the recombination from the low energy side of the PL that shows the longest time decay. Figure 4.15 plots the typical results for the fast detector measurements. The system response curve is also shown in the plot. The decay curve used for fitting is the curve deconvolved with the system response, shown by the red line in the plot.

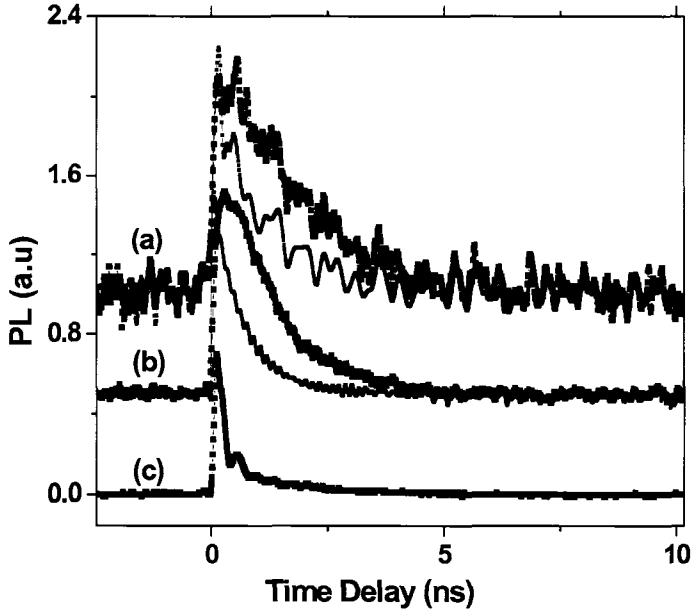

Figure 4. 15 Temporal evolution of the PL intensity at T=50K for (a) InGaAs and (b) InGaAsN samples before (black) and after (red) deconvolution with system response. Curve (c) is the instrumental response function for curve (a) and (b).

The decay time constant as a function of temperature obtained from the data of Figure 4.15 are plotted in Figure 4.16. For comparison, the lifetime obtained from the up-conversion method is also plotted in the figure as solid symbol. Reasonable agreement between the two methods is obtained. It is noted that for InGaAsN QW at T<100K, a longer PL lifetime is measured when the carrier localization becomes stronger, in agreement with the behavior shown in Figure 4.2.

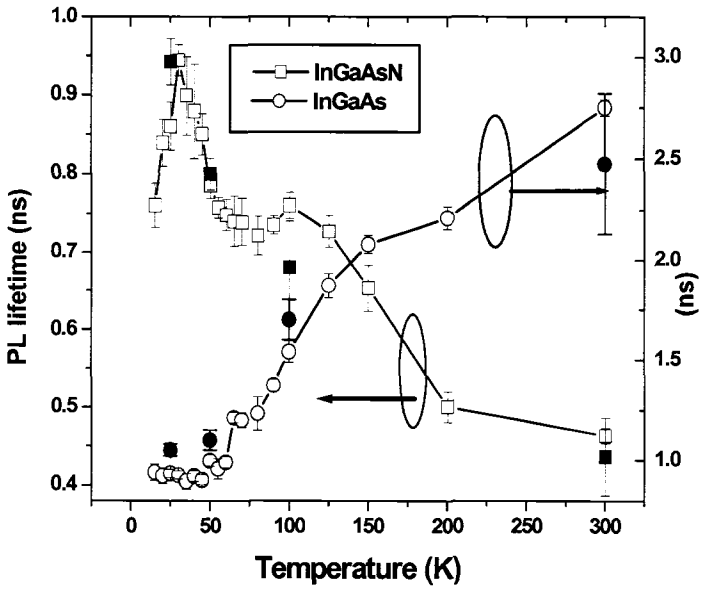

Figure 4.16 PL intensity lifetime as function of temperature from 10K to 300K (InGasAsN - □ and InGaAs - ○). The solid symbols denote the maximum decay constant obtained from up conversion measurement.

The lifetime decreases as temperature increases for T>100 K. Instead in InGaAs, the lifetime does not depend on temperature below 50 K and above 50 K it increases with temperature. As shown in Figure 4.8, the emission contains contribution from free carriers and excitons [22]. For a mixture of exciton and free carriers, radiative recombination leads to an increased lifetime following a temperature dependence that is a mixture of T and $T^{3/2}$, similar to that observed in the data of figure 4.16 for InGaAs QWs. Monomolecular recombination would also increase the lifetime with temperature due to a decrease in the defect collision cross section [23]. Thus, the decrease in lifetime observed in InGaAsN is

likely due to a significant contribution of Auger recombination. An increased hole escape from the well might also contribute to the decreased lifetime, which will be shown in chapter 5.

4.5 Summary

In this chapter, we employed steady state and time resolved photoluminescence to investigate different aspects of carrier recombination in InGaAsN/GaAs single QW structures: luminescence emission characterization, carrier localization, measurement of band edge electron effective mass and carrier recombination dynamics.

Polarization dependent photocurrent measurements showed that the PL spectra obtained under high excitation conditions contains contributions from the e1-hh1 and e1-lh1 transitions in both InGaAs and InGaAsN. We discovered through time resolved PL spectra measurement that holes are populated almost simultaneously on both heavy hole and light hole states after photo excitation, leading to a possible enhanced hole leakage from the well to SCH in InGaAsN QW due to the reduced confinement of light hole state compared to InGaAs QW.

The incorporation of nitrogen creates carrier localization and nonradiative recombination centers. The former only exists at low temperature (T<100K) and exhibits a rather long lifetime. We ascribe the reduction in the lifetime at T>100K to non-radiative recombination. These processes deteriorate the luminescence efficiency of the InGaAsN QW.

Employing steady state PL spectra data with relatively low excitation intensity, we carried out a detailed PL lineshape analysis. This analysis allowed extraction of the exciton binding energy which was found to increase from R= 9.72meV to R=17.5meV when the nitrogen content in the single InGaAsN QW increases from 0 to 0.5%. The electron effective mass was obtained from the exciton binding energy using a fractional parameter model. This approach yielded $m_e^*=(0.049\pm0.007)m_0$ and $m_e^*=(0.11\pm0.015)m_0$ for InGaAs and InGaAsN. The excellent agreement obtained in me* for InGaAs verifies the validity of our approach, which in turn is more accurate as it is less sensitive to variations in the band offset ratio. The effect of a larger m_e^* on the device performances is two fold: on one hand, the increase of m_e^* might have positive impact on high speed modulation ability of the device in that it enhances the intrinsic differential gain; on the other hand, an enhanced m_e^* may lead to a higher transparent carrier density, thus for given losses of the device, higher threshold carrier density.

Reference

[1] K.P.O'Donnell, X.Chen, "Temperature-dependence of semiconductor band-gaps" APPLIED PHYSICS LETTERS **58** (25): 2924-2926 JUN 24 (1991).

[2] L.Grenouillet,, C.Bru-Chevallier, G.Guillot, P.Gilet , P.Duvaut, C.Vannuffel, A.Million , A.Chenevas-Paule, " Evidence of strong carrier localization below 100 K in a GaInNAs/GaAs single quantum well", APPLIED PHYSICS LETTERS **76** (16):2241 (2000).

[3] M.Oueslati, M.Zouaghi, M.E.Pistol, L.Samuelson, etc. "Photoluminescence study of localization effects induced by the fluctuating random alloy potential in indirect band-gap $GaAs_{1-x}P_x$ ", PHYSICAL REVIEW B **32** (12): 8220-8227 (1985).

[4] N.Tansu, L.J.Mawst, "Current injection efficiency of InGaAsN quantum-well lasers", JOURNAL OF APPLIED PHYSICS **97** (5): Art. No. 054502 (2005).

[5] Chow WW, Jones ED, Modine NA etc, "Laser gain and threshold properties in compressive-strained and lattice-matched GaInNAs/GaAs quantum wells", APPLIED PHYSICS LETTERS **75** (19): 2891-2893 NOV 8 (1999).

[6] J. Wu, W. Shan and W. Walukiewicz, "Band anticrossing in highly mismatched III-V semiconductor alloys", SEMICONDUCTOR SCIENCE AND TECHNOLOGY **17** (8): 860-869 AUG (2002).

[7] S.Tomic, E.P.O'Reilly, R.Feshe, etc. "Theoretical and experimental analysis of 1.3μm InGaAsN/GaAs Lasers", IEEE JOURNAL OF SELECTED TOPICS IN QUANTUM ELECTRONICS **9** (5): (2003).

[8] Z. Pan, L.H. Li, Y.W. Lin, etc, "Conduction band offset and electron effective mass in GaInNAs/GaAs quantum-well structures with low nitrogen concentration", APPLIED PHYSICS LETTERS **78** (15):2217 (2001).

[9] M. Hetterich, M.D. Dawson, A.Y. Egorov, D. Bernklau, and H. Riechert, "Electronic states and band alignment in GaInNAs/GaAs quantum-well structures with low nitrogen content", APPLIED PHYSICS LETTERS **76** (8): 1030 (2000).

[10] J.B. Heroux, X. Yang, and W.I. Wang, "Photoreflectance spectroscopy of strained InGaAsN/GaAs multiple quantum wells", JOURNAL OF APPLIED PHYSICS **92** (8): 4361 (2002).

[11] H. Mathieu, P. Lefebvre, and P. Christi, "Simple analytical method for calculating exciton binding energies in semiconductor quantum wells" PHYSICAL REVIEW B **46**(7): 4092 (1992).

[12] D.S. Chemla, "Two dimensional semiconductors-recent development", JOURNAL OF LUMINESCENCE **30** (1-4):502-519 (1985).

[13] M. Colocci, M. Gurioli and A. Vinattieri, "Thermal ionization of excitons in GaAs/AlGaAs quantum well structure", JOURNAL OF APPLIED PHYSICS, **68**(6): 2809 (1990).

[14] Basu PK, *Theory of Optical Processes in Semiconductors: Bulk and Microstructures*, Oxford University Press, New York (2002).

[15] I. Vurgaftman, J. R. Meyer and L. R. Ram-Mohan "Band parameters for III-V compound semiconductors and their alloys" JOURNAL OF APPLIED PHYSICS **89** (11): 5815-5875 Part 1, (2001)

[16] S. T. Ng, W. J. Fan, Y. X. Dang, and S. F. Yoon, "Comparison of electronic band structure and optical transparency conditions of InxGa1-xAs1-yNy/GaAs quantum wells calculated by 10-band, 8-band, and 6-band k center dot p models"PHYSICAL REVIEW B **72**, 115341 (2005).

[17] L. A. Coldren and S. W. Corzine, *Diode lasers and Photonic Integrated Circuits*: Wiley series in microwave and optical engineering, (1995).

[18] D. J. Palmer, P. M. Smowton, P. Blood, J. Y. Yeh, L. J. Mawst, and N. Tansu,"Effect of nitrogen on gain and efficiency in InGaAsN quantum-well lasers," APPLIED PHYSICS LETTERS, vol. **86** (7), Art. No. 071121, (2005).

[19] O. Anton, L.F. Xu, D. Patel, C.S. Menoni, J.Y. Yeh, T.T. Van Roy, L.J. Mawst and N. Tansu, "The intrinsic frequency response of 1.3-mu m InGaAsN lasers in the range T=10 degrees C-80 degrees C' IEEE PHOTONICS TECHNOLOGY LETTERS **18** (13-16): 1774-1776 (2006).

[20] H.D.Sun, A.H.Clark, S.Calvez, M.D.Dawson, N.Y.Qiu, J.M.Rorison, K.S.Kim, T.Kim, Y.J.Park, "Spectroscopic characterization of 1.3 μm GaInNAs quantum-well structures grown by metal-organic vapor phase epitaxy" APPLIED PHYSICS LETTERS 86 (9): Art. No. 092106 (2005).

[21] N.J. Kim, Y.D. Jang, D. Lee, K.H. Park, W.G. Jeong and J.W. Jang, "Reliable strain determination method for InGaAsN/GaAs quantum wells using a simple photoluminescence measurement" APPLIED PHYSICS LETTERS 83 (15): 3114-3116 OCT 13 (2003).

[22] L.F. Xu, D.Patel and C.S.Menoni, "Optical determination of the electron effective-mass of strain compensated $In_{0.4}Ga_{0.6}As_{0.995}N_{0.005}$/GaAs Quantum Well structure", APPLIED PHYSICS LETTERS **89** (17): Art. No. 171112 OCT 23 (2006).

[23] Abakumov V.N , Perel V.I. and Yassievich I.N, " *Nonradiative recombination in semiconductors*" , Elsevier Science Publishers B.V. (1991).

[24] J.M. Pikal, C.S. Menoni, P. Thiagarajan, G.Y. Robinson, and H. Temkin, "Temperature dependence of intrinsic recombination coefficients in 1.3 mm InAsP/InP quantum-well semiconductor lasers", APPLIED PHYSICS LETTERS **76** (19): 2659-2661 MAY 8 (2000).

CHAPTER 5

Carrier and gain dynamics in InGaAsN/GaAs Quantum Wells

The motivation of this chapter is to understand carriers and gain dynamics in dilute nitride quantum wells, processes that affect the high frequency operation of the InGaAsN lasers. We do this by studying the nonlinear gain dynamics and carrier capture and escape processes of ridge waveguide (RWG) laser devices, employing sub-picoseconds pump-probe transmission techniques.

5.1 Background

Gain nonlinearity and carrier capture and escape processes are important not only because of the fundament physics they represent, but also because of their dramatic effect on the dynamic response of the laser diodes, especially in high speed modulation applications[1][2].

The relaxation resonance frequency f_R, directly related to the modulation bandwidth, includes the gain nonlinearity and carrier transport effects[3][4]:

$$f_R^{\,2} = \frac{v_g \cdot dg/dN_w}{4\pi^2 \tau_p (1+\tau_{cap}/\tau_{esc}) \cdot (1+\varepsilon N_{P0})} \cdot N_{P0} \qquad (5.1)$$

We see that the square of f_R is directly proportional to the differential gain dg/dN_w, group velocity v_g and the average photon density in the cavity, and inversely proportionally to the photon lifetime in the cavity τ_p. For an ideal infinite QW structure, where the capture process is much faster than carrier escape, $\tau_{cap}/\tau_{esc} \rightarrow 0$, and gain compression can be neglected, $\varepsilon N_{P0} << 1$, thus the enhancement of the intrinsic differential gain dg/dN_w leads to the theoretical predictions of increased modulation bandwidth in quantum well lasers. However, in reality, this enhancement in the modulation bandwidth proved initially to be elusive. This is because in most semiconductor lasers to date, as noticed from Eq. (5.1), the effect of gain compression and capture/escape time ratio impose an ultimate limit in the high speed modulation. Note that here the capture time τ_{cap} is

the sum of the quantum mechanics capture time into the QW (τ_{cap_QW}) and the transport time from the edge of the SCH to the QW (τ_{tr}).

Therefore, study of the nonlinear gain and its relaxation dynamics, measuring the carrier capture and escape processes are of intrinsic importance in understanding and improving the high speed performance of dilute nitride lasers. Only limited work have been devoted in investigating the nonlinear gain dynamics of InGaAsN/GaAs QW lasers [5][6]. Although large values for the differential gain and the gain compression factor have been discovered recently in dilute nitride lasers [7], the origin of the nonlinear gain and the time domain relaxation of the gain compression need to be further explored.

Presumably, the nonlinearity of the gain is fundamental in that it is more associated with the quantum well material rather than the laser diode structures. Carrier transport, capture and escape, are more related to laser structures. The nonlinear gain saturation mechanism, as have been studied thoroughly in other well developed laser diodes such as InP-based lasers, includes spectral hole burning, carrier heating and two-photon absorption [8][9][10]. The time domain behavior of each nonlinearity mechanism will be discussed in the following section.

As to carrier transport effects, it has been pointed out in recent work [4][7] that the bandwidth of current dilute nitride lasers is mainly limited by carrier transport effects which reduce the effective differential gain and cause a rapid increase of the threshold current. However, the transport effect cited in the previous work, which is a function of the carrier escape and capture rates, was

only theoretically calculated based on a thermionic process assumption [11]. Thus, to verify the theoretical results on carrier capture and escape time and these recent discoveries on the bandwidth limit factors due to nitrogen incorporation, direct experimental measurements of the transport time are especially important.

5.2 Analysis of nonlinear gain dynamics

As discussed in section 2.4, pump and probe experiments provide the framework to investigate the gain dynamics. When pumping the waveguide devices with short optical pulses, one disturb the system's equilibrium, and the following interactions are reflected by a impulse response function h(t) given in Eq. (2.1). The transmission change of probe is the correlation of pulse intensity cross-correlation

$$C(t'') = \int_{-\infty}^{\infty} dt' I_p(t') I_{pr}(t'+t'') \tag{5.2}$$

with the impulse response h(t) of the waveguide:

$$\Delta T(\tau) = \int_{-\infty}^{\infty} dt'' h(t''+\tau) \int_{-\infty}^{\infty} dt' I_p(t') I_{pr}(t'+t'') \tag{5.3}$$

For the situation in which the pump and the probe have the same wavelength and are resonant with the ground state in the well, the pump pulse

induces a transient gain (absorption) step change due to pump-induced interband stimulated transitions, as well as a transient gain compression due to the heating of the carrier distribution by two photon absorption (TPA) and free carrier absorption (FCA) [12-15]. As has been discussed in chapter 3, heating the carrier distribution reduce the gain. Immediately after the initial transitions, the carrier distribution becomes non-Fermi with a carrier concentration change. Strong carrier-carrier and carrier-phonon interaction bring the carrier distribution into equilibrium with the lattice, at lattice temperature T_0 [16]. This time is identified as the gain compression relaxation time. Up to this point, the carrier distribution has still not been fully recovered. The last stage in this relaxation processes is carrier escape from the well and carrier recombination through spontaneous emission which takes places in tens of picoseconds to nanoseconds. The whole interaction is schematically illustrated in Figure 5.1.

Therefore, the impulse function h(t) can be fitted as a sum of different time constants:

$$h(t) = u(t)\left[a_1 \cdot \exp(-t/\tau_1) + a_2 \cdot \exp(-t/\tau_2) + a_3 \cdot \exp(-t/\tau_3\right] + a_4\delta(t) \quad (5.4)$$

Here

$$u(t) = \begin{cases} 0 & t < 0 \\ 1 & \text{otherwise} \end{cases} \quad (5.5)$$

reflects the "step" change in the probe transmission caused by the pump-induced carrier density change.

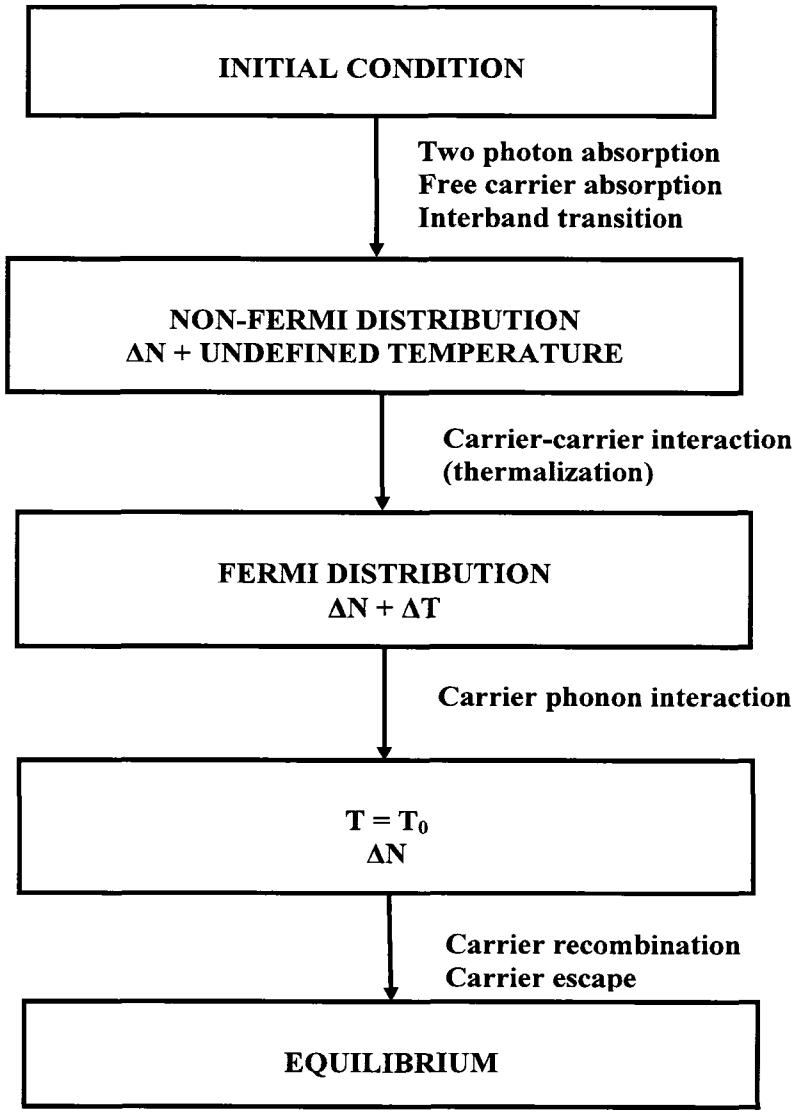

Figure 5. 1 Schematic diagram for transient gain dynamics.

Other parameters in Eq. (5.4) represent the physical processes as described in Figure 5.1, where a_1 is the amplitude of gain (absorption) step change and τ_1 denotes the interband relaxation time constant. The sign of a_1 is dependent on which regime the pump beam is exciting. Depending on carrier injection, the pump pulse is absorbed and probe pulse transmission is increased ($a_1>0$) due to absorption bleaching in absorption regime. In the other case in gain regime, the pump pulse is amplified and the probe pulse transmission is reduced due to gain compression ($a_1<0$). There is no step change in the probe transmission associated with pump induced transition in the transparency point ($a_1=0$). In the absorption regime, the pump pulse induces stimulated absorption and τ_1 represents the combined effect of carrier recombination and carrier escape from the well. In the gain regime, the pump pulse induces stimulated emission, the relaxation of the induced step change can be regarded as an infinitely long processes. a_2 is the amplitude of the carrier heating with relaxation time constant τ_2. Carrier heating includes multiple nonlinearities from both intraband [e.g., carrier heating due to free carrier absorption (FCA)] and interband [e.g., spectral hole burning and carrier heating or cooling due to stimulated transitions] effects. Carrier heating due to intraband transition reduces the gain in all regimes of diode operation, as demonstrated in our analytical gain model in chapter 3, thus it always has a negative contribution to a_2. However, gain nonlinearity due to stimulated interband transition does not always have a negative attribution to a_2. Generally there is also a transient absorption bleaching (transient increase in gain) observed in gain dynamics pump-probe measurements [9][18] which recovers with a 100-

250 fs time constant. This can be due to spectral hole burning, or can be explained by a delay in the turn-on of carrier heating. We assign $a_3 \cdot \exp(-t/\tau_3)$ to denote this process. The term $a_4 \cdot \delta(t)$ models two photon absorption (TPA) and a_4 is usually a negative value. Since the time resolution of the experiment is limited by the pulse width of pump and probe, we use a cross correlation of the pump and probe pulse to replace $\delta(t)$ in the fitting process. Table 5.1 summarizes the sign of the parameters (a_i) and their associated contributions as discussed above.

Table 5. 1 Sign of the components (a_i) in the impulse response function h(t) in single color pump-probe experiment.

Prameters \ Operation regimes		gain	transparency	absorption
a_1	Interband transition	-	0	+
a_2	Intraband (FCA)	-	-	-
	Interband (carrier heating)	+	0	-
a_3	Absorption bleaching	+	+	+
a_4	Two photon absorption	-	-	-

In this work, we are especially interested in investigating a_2 and τ_2, in regarding to the nonlinear gain compression and its relaxation dynamics. Keep in mind that the pump (TE) and probe (TM) are cross-polarized for the single color pump-probe experiment described in 2.4.2. Ideally due to the selection rule, the e1-hh1 transition is only allowed for TE polarized light (parallel to QW layer) but forbidden to TM polarization (perpendicular to QW layer). Considering that the

polarization selection rules are only strictly true at the Brillouin zone center and that the effect of band mixing, built-in field from doping in cladding layer and applied bias current will further break the selection rule, a probe beam with TM polarization is still able to sense the dynamics at the e1-hh1 transition induced by the TE polarized pump pulse. This can be verified from our polarization dependent photocurrent measurement (PC) as shown in Figure 4.5, in which the PC signal at transition e1-hh1 is considerably reduced but not completely quenched for TM polarization.

With pump beam outside of the well and the probe resonant in the well, we are able to evaluate the carrier capture and escape processes even in the gain regime, as well as simplify the interpretation of the impulse function by eliminating gain (absorption) bleaching, spectral hole burning and by reducing the sensitivity to state filling at the pump wavelength. Another advantage of this approach is that both pump and probe beam can have the same polarization and can be separated using a spectral filter due to the different wavelengths. The new impulse function is therefore expressed as:

$$h(t) = u_1(t) \cdot \left[a_1 \cdot \exp(-t/\tau_1) + a_2 \cdot \exp(-t/\tau_2)\right] + a_4 \delta(t) \qquad (5.6)$$

where a_1 is the amplitude of carrier escape and a_2 is amplitude of carrier recombination. Taking into account the quantum capture time of carriers from out-of-well state into the QW, we rewrite the step function as:

$$u_1(t) = \begin{cases} 0 & t < 0 \\ 1 - \exp(-t/\tau_{cap\_QW}) & \text{otherwise} \end{cases} \quad (5.7)$$

5.3 Nonlinear gain dynamics study

The nonlinear gain dynamics is investigated in ridge waveguide (RWG) InGaAs and InGaAsN single QW lasers. To study the nonlinear dynamics of the laser diode in different operation regimes, such as absorption, transparency and gain regime, we varied the bias current for a fixed pump-probe wavelength, or varied the pump-probe wavelength while the bias current is fixed. Thus in our data presented below, probe transmission as a function of pump-probe time delay are shown for the absorption, transparency and gain regime, respectively.

5.3.1 Gain Spectrum Measurements

To select the gain(absorption) condition in which the pump-probe experiment are performed, the gain spectrum of both InGaAsN and InGaAs RWG lasers with different current biasing are obtained by applying Hakki-Paoli analysis [17] on the amplified spontaneous emission (ASE) traces. Figure 5.2 shows typical ASE spectra of InGaAsN (a) and InGaAs (b) lasers under different biasing, and the corresponding gain spectra are presented in Figure 5.3. The arrows in the gain map denote the wavelengths chosen in the pump-probe experiments.

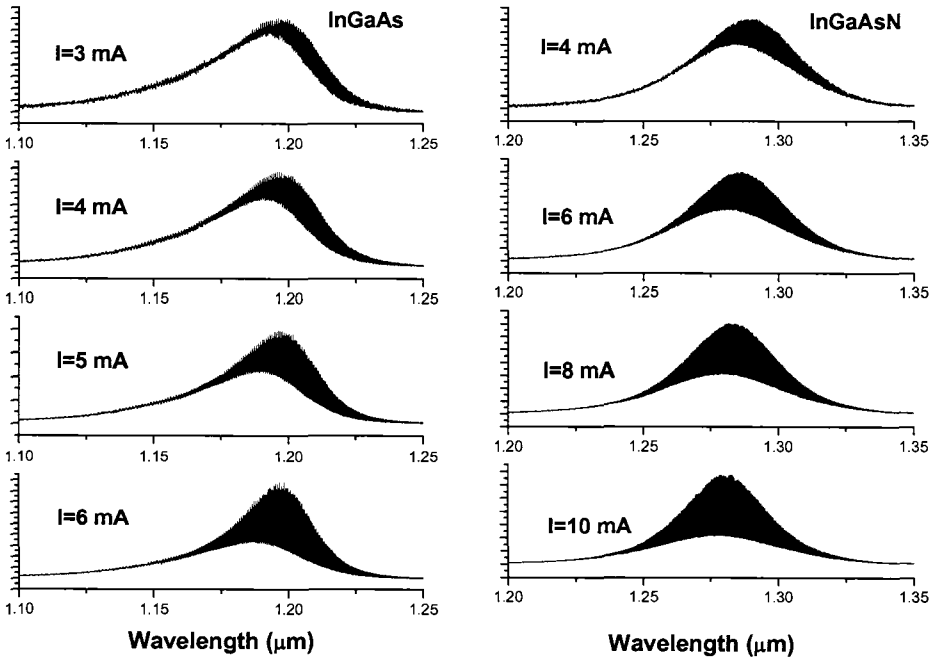

Figure 5. 2 Amplified spontaneous emission traces obtained in $In_{0.4}Ga_{0.6}As$ and $In_{0.4}Ga_{0.6}As_{0.995}N_{0.005}$ single quantum well (QW) ridge waveguide (RWG) lasers held at room temperature. Due to the low current applied (<10mA), current heating is not considered as a issue and no temperature control has been applied.

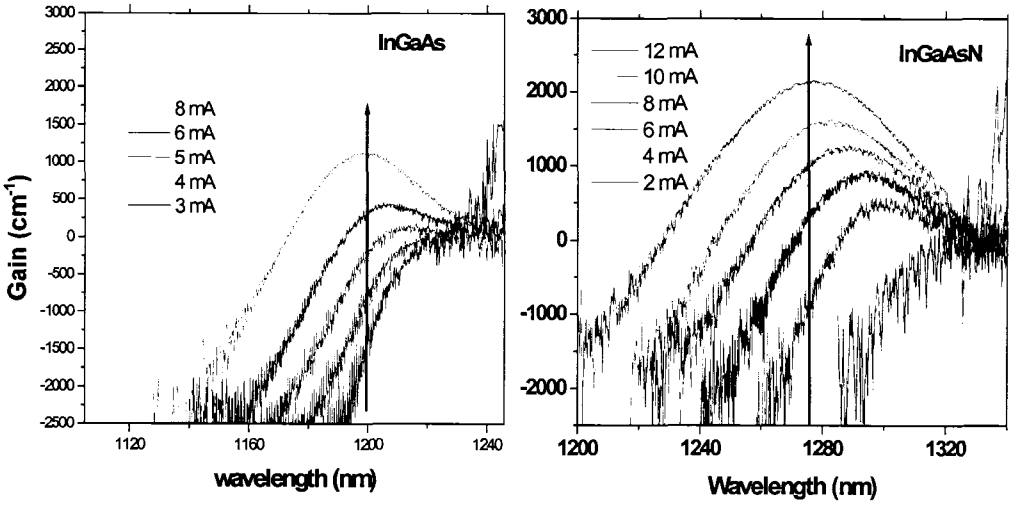

Figure 5. 3 Gain spectra extracted from Figure 5.4 for both $In_{0.4}Ga_{0.6}As$ and $In_{0.4}Ga_{0.6}As_{0.995}N_{0.005}$ single quantum well (QW) ridge waveguide (RWG) lasers.

5.3.2 Pump-Probe results

Figure 5.4 shows the measured change in probe transmission as a function of pump-probe delay in the three regimes of operation. The data are displayed in a time scale that includes negative time delays (probe leads the pump) as well as positive delays (probe lags the pump). The negative time delays are shown to verify that the system is causal and that there no strange misalignments in the pump-probe arms that might cause a change in probe transmission in the absence of the pump.

First, notice that for a time delay longer than 2-3 ps, the gain seen by the probe is increased in the absorption regime and decreased in the gain regime. This is the step change in the gain due to pump-induced carrier density changes. Within the pump-probe time scale shown here, ~14 ps, the exponential recover due to the much longer spontaneous recombination does not show. As expected, in the transparency regime, where stimulated emission and stimulated absorption are equally probable, there is no long-lived change in the gain seen by the probe.

The traces of Figure 5.4 also show that for each regime, there is a transient gain compression that recovers with a time constant of ~2-3 ps. This compression, as we discussed in the previous section, is associated with the heated carrier distribution cooling back to the lattice temperature, and corresponds to the time constant denoted as τ_2. In the transparency and gain regimes of InGaAs, this compression is less visible. The instantaneous transient increase and gain decrease are also observed at very early stages of time delay, with a time constant

of approximately 100~200 fs and associated with transient absorption bleaching and TPA.

As described previously, we evaluated these transmission changes of the probe pulse by fitting it with the convolution of the pulse intensity cross-correlation of Figure 2.12 with the impulse response h(t) of the sample given by Eq. (5.4). Since the time step relaxation is a long lived processes in our time scale, we choose τ_1=1 ns for all. A 100 fs rise time for u(t) is applied in the fitting. The dotted lines in Figure 5.4 are the best fit and Figure 5.5 illustrate the separate components in the fit of Figure 5.4 (a). The corresponding impulse response functions in each situation that have been used to fit the data are presented next.

For InGaAs/GaAs QW lasers, the impulse function h(t) used in the fitting are:

$$h(t) = u(t)(1.05 \cdot e^{-t/1ns} - 0.91 \cdot e^{-t/2.9ps} + 3.8 \cdot e^{-t/0.16ps}) + 0\delta(t) \qquad (5.8)$$

in the absorption regime,

$$h(t) = u(t)(0.05 \cdot e^{-t/1ns} - 0.17 \cdot e^{-t/2.7ps} + 0 \cdot e^{-t/0.16ps}) - \delta(t) \qquad (5.9)$$

in the transparency regime, and

$$h(t) = u(t)(-0.17 \cdot e^{-t/1ns} - 0.13 \cdot e^{-t/2.1ps} + 0 \cdot e^{-t/0.16ps}) - 0.7 \cdot \delta(t) \quad (5.10)$$

for the gain regime.

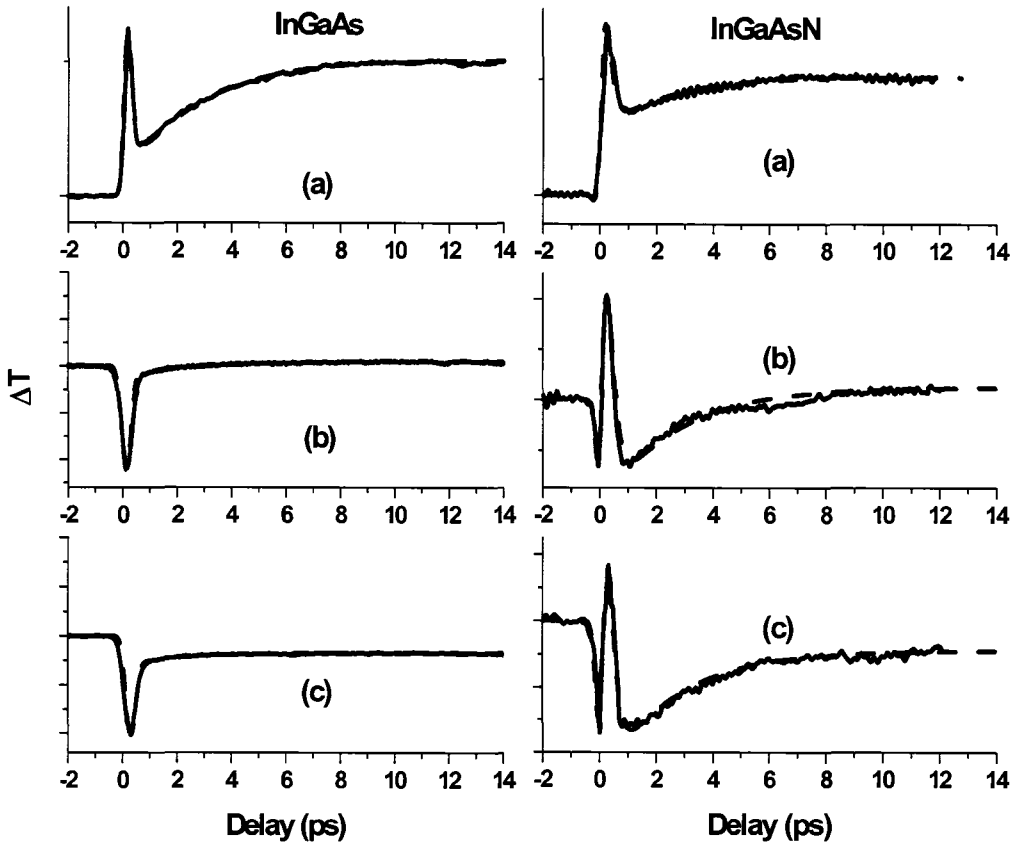

Figure 5. 4 Measured change in probe transmission (solid line) and fit (dashed line) as function of pump-probe delay for both InGaAs/GaAs and InGaAsN/GaAs RWG single QW lasers. Experiments are performed based in three regimes of operation: (a) absorption, (b) transparency and (c) gain, respectively and the values are shown in the plot. The pump is TE-polarized and the probe is TM polarized.

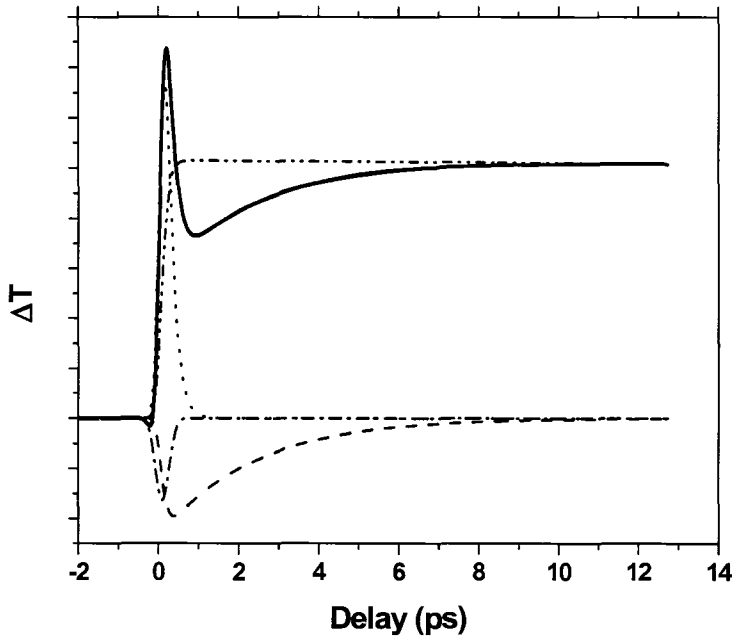

Figure 5. 5 Step due to stimulated transitions (dash dot dot line, $u(t)\cdot a_1 e^{-t/\tau 1}$), carrier heating (dash line, $u(t)\cdot a_2 e^{-t/\tau 2}$) , absorption bleaching (dot line, $u(t)\cdot a_3 e^{-t/\tau 3}$) and TPA (dash dot line, $a_4\delta(t)$) components separated from the total fits (solid line) shown in Figure 5.4 (a).

Similar fitting procedure are performed on InGaAsN. The impulse function h(t) is

$$h(t) = u(t)(0.86\cdot e^{-t/1ns} - 0.4\cdot e^{-t/2.3ps} + 4\cdot e^{-t/0.16ps}) - 0.25\delta(t) \qquad (5.11)$$

in the absorption regime,

$$h(t) = u(t)(0.05 \cdot e^{-t/1ns} - 0.5 \cdot e^{-t/2.5ps} + 5 \cdot e^{-t/0.21ps}) - 0.85\delta(t) \quad (5.12)$$

in the transparency regime, and

$$h(t) = u(t)(-0.18 \cdot e^{-t/1ns} - 0.77 \cdot e^{-t/2.4ps} + 7.8 \cdot e^{-t/0.21ps}) - 1.6\delta(t) \quad (5.13)$$

in the gain regime.

To summarize, Table 5.2 lists the values of the amplitudes (a_i's) and the time constants (τ_i's) of the impulse functions used in the fits.

Table 5.2 Components in the impulse response function h(t) fits for InGaAs/GaAs and InGaAsN/GaAs single QW lasers data shown in Figure 5.4.

	Step	Carrier heating		Absorption bleaching		TPA
Diode	a_1	a_2	τ_2	a_3	τ_3	a_4
InGaAs (gain)	-0.17	-0.13	2.1 ps	0	0.16 ps	-0.7
(transparency)	0.05	-0.17	2.7 ps	0	0.16 ps	-1
(absorption)	1.05	-0.91	2.9 ps	3.8	0.16 ps	0
InGaAsN (gain)	-0.18	-0.77	2.4 ps	7.8	0.21	-1.6
(transparency)	0.05	-0.5	2.5 ps	5	0.21 ps	-0.85
(absorption)	0.86	-0.4	2.3 ps	4	0.16 ps	-0.25

From the fitting results, we see that in the gain regime, both carrier heating and two photon absorption contribute to the compression of the gain. It is interesting that while in InGaAsN laser carrier heating has a more significant effect on gain compression; the relaxation time constant of carrier heating in both lasers have similar values, 2-3 ps. In all three regimes, gain, transparency and absorption, the relaxation time ascribed with carrier heating is the same.

In summary, gain nonlinearity and its ultrafast dynamics are investigated through sub-picoseconds pump-probe transmission measurements. Carrier heating, two photon absorption (TPA) are observed and suggested to contribute to gain compression. The material related carrier heating relaxation time shows no observable difference between dilute nitride laser and its nitrogen free counterpart.

5.4 Study of carrier capture and escape processes

The carrier capture and escape times, τ_{cap}, τ_{esc}, are very important parameters that determine the static as well as the dynamic performance of quantum well lasers. In dynamic operating conditions the capture and escape times affect both the resonant frequency and the damping rate of the modulation response, and thus determine the lasers' modulation bandwidth.

Recently high performance InGaAsN/GaAs QW lasers have been demonstrated with high speed modulation bandwidth [19][20]. However, these benchmarks are still distanced from the high frequency bandwidth limit of that

theories predict [21][22]. Our nonlinear gain dynamics study described in the previous section has shown similar gain compression relaxation processes in both dilute nitride and nitrogen free laser diodes, suggesting that gain compression and its relaxation are not the main factor that limits the bandwidth of InGaAsN lasers. It has been recently pointed out that the limitation of bandwidth of current dilute nitride lasers are mainly due to thermal effects which reduce the effective differential gain and cause a rapid increase of the threshold current [4][7] . In addition, supportive theoretical calculations of carrier thermionic escape process have suggested the existence of an increased hole leakage that is attributed to the thermal problem [11]. However, no direct experimental evidence has been provided so far on this effect. These calculations have relied on the assumption of a smaller hole confinement in the InGaAsN QW lasers, an issue that is still relatively controversial. In this study we investigate τ_{cap} and τ_{esc}, of InGaAsN/GaAs QW lasers. As has been pointed in section 5.2, the single color pump-probe method has the limitations in investigating carrier escape processes, especially in the gain regime. Therefore, for these studies we have used a two-color pump-probe differential transmission measurements to study carrier escape in the absorption, transparency and gain regimes.

Generally, it is the ratio of capture and escape time constant ($R=\tau_{cap}/\tau_{esc}$) that determines the modulation response. Here the τ_{cap} is the sum of quantum capture time τ_{cap_qw} and the transport time from the edge of barrier to the QW, τ_{tr}. The risetime in pump-probe data indicates the quantum capture time, which is significantly shorter than the carriers transport time across the SCH region in QW

lasers. From the time-resolved PL data in chapter 4, we can estimate τ_{tr} that is ~10ps and dominant in τ_{cap}.

5.4.1 Two-Color pump-probe measurement technique

In the two-color pump-probe differential transmission experiment, we selected the wavelength of the pump pulse to be resonant with the unconfined states in the barrier, while the probe beam was tuned to be resonant with the lasing line inside the well. In this situation, the pump pulse is always in the absorption regime and induces an increase in the carrier density in the well. The probe, therefore, senses the increase of gain, and the subsequent decay due to carrier recombination and escape out of the well. The schematic relationship between the pump, the probe and the band structure is shown in Figure 5.6.

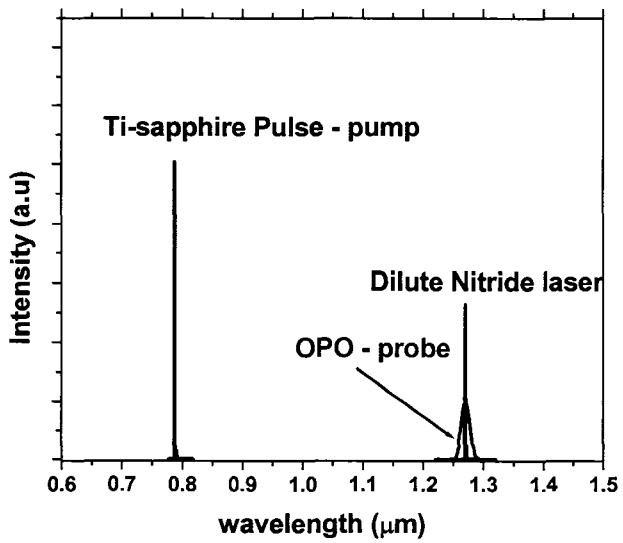

(a)

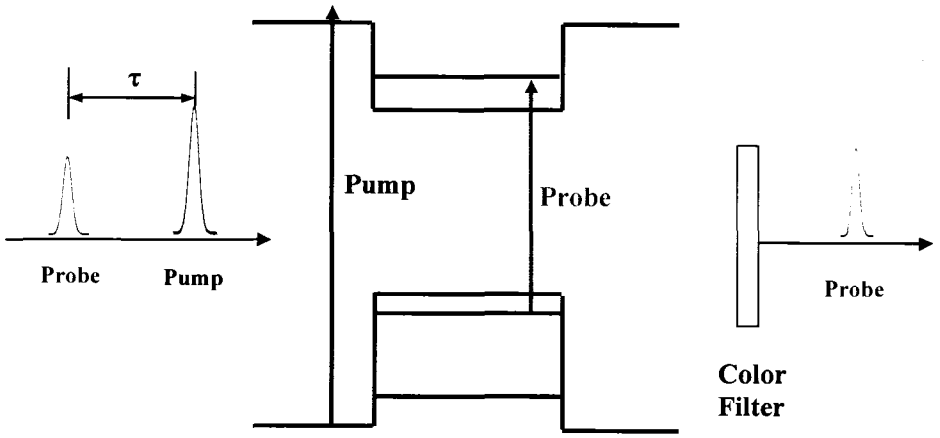

(b)

Figure 5.6 (a) Spectra of pump and probe pulses and their relationships with the lasing wavelength in the devices under investigation. (b) Schematic of the energy levels in the QW indicating the states that are accessed by the pump and probe pulses, respectively.

5.4.2 Results

Figure 5.7 shows the change of probe transmission, ΔT, induced by the pump pulse as function of pump-probe delay with different biasing conditions. An exponential decay following an instantaneous rise is observed for both lasers. With the pump beam exciting only the unconfined state outside of the QW and probing the ground state in the well, the risetime of ΔT reflects the carrier capture process into the well. The decay time can be ascribed to contribution of both carrier escape from the well and spontaneous carrier recombination. The latter, from the results of PL lifetime measurements in chapter 4 at room temperature, is on the order of 300-400 ps for InGaAsN and >2 ns for InGaAs lasers, respectively. Thus, the decay ΔT observed here, which is less than ~100 ps, mainly represents the carrier escape process. The decay time ΔT as a function of biasing is plotted in Figure 5.8.

A more significant decrease of the escape time with increased bias is observed for dilute nitride laser, compared with InGaAs laser. At a bias just below threshold, τ_{esc} is found to be more one order of magnitude less in InGaAsN laser compared to its nitrogen free sample. The smaller τ_{esc} influences the current injection efficiency as well as the high speed modulation ability of the dilute nitride lasers [23][24].

The following section analyzes in detail the origin of the significantly smaller τ_{esc} in dilute nitride lasers.

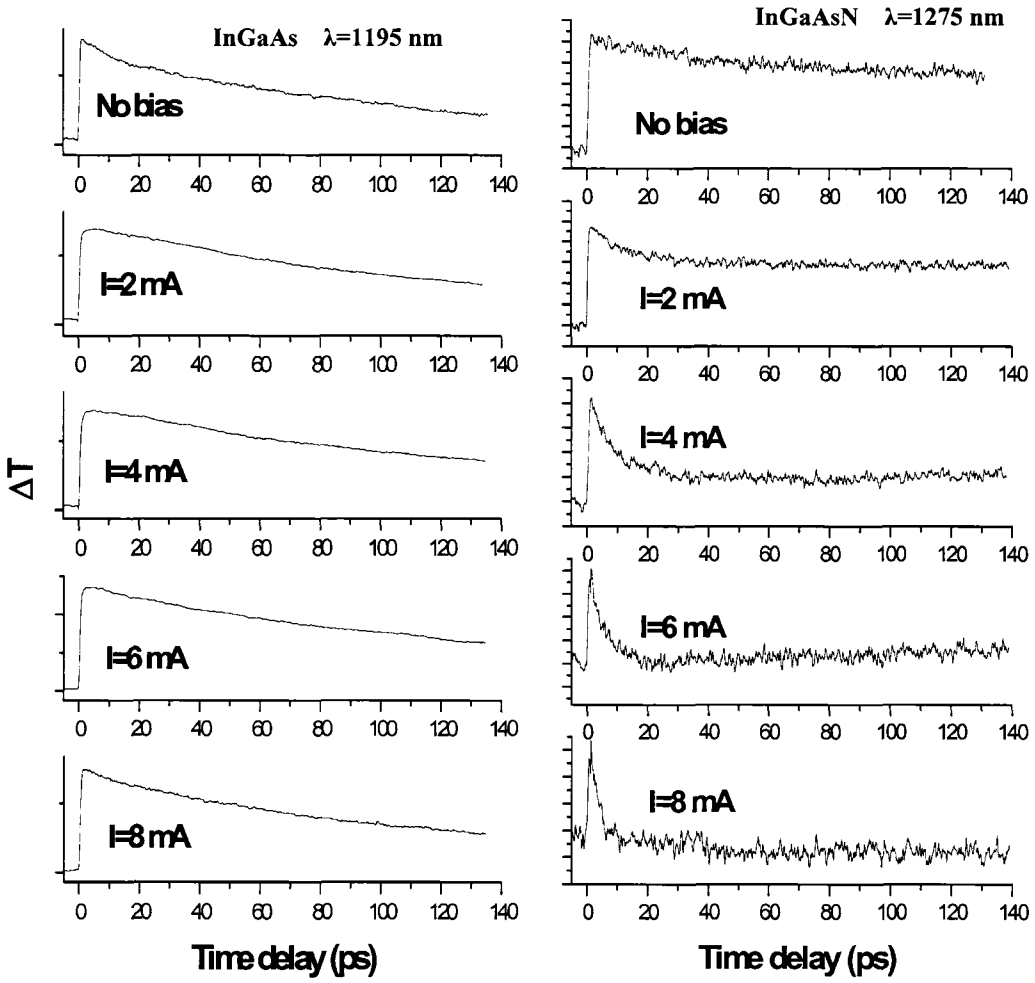

Figure 5.7 Relative changes in the probe transmission induced by the pump as a function of the pump-probe delay, for both InGaAs and InGaAsN RWG lasers. The biasing is varied below threshold. The traces are recorded at the wavelengths indicated in the figure.

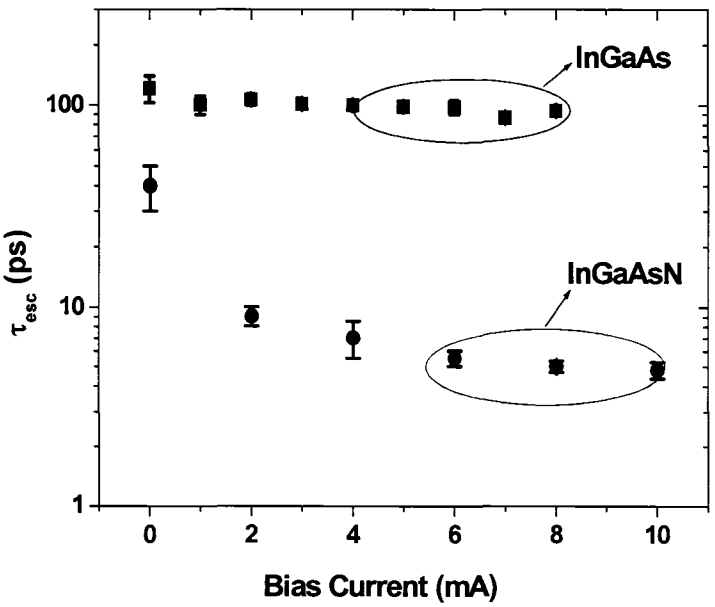

Figure 5. 8 Experimentally measured carrier escape time τ_{esc} as function bias current at room temperature.

5.4.3 Analysis of carrier dynamics in dilute nitride lasers

We ascribe the carrier escape from the QW state to the barrier to two processes: phonon-assisted direct tunneling through the triangular barrier induced by the built-in electric field and thermionic emission from the QW level to the barrier.

$$\frac{1}{\tau_{esc}} = \frac{1}{\tau_{therm}} + \frac{1}{\tau_{tunn}} \tag{5.14}$$

Generally it is believed that in a quantum well structure, the thermionic processes is dominant [11][25], and previous theoretical work on prediction of carrier escape time has been based on the thermionic assumption only. There has also been evidence that for shallow wells, tunneling of carrier from the well is not negligible [26]. In this section, we develop both thermionic and tunneling carrier escape models, which allow to quantitively interpret our measurement results and evaluate the origin of the increased rate of carrier escape in dilute nitride lasers.

To apply the model calculation, we first need to convert the measured escape time as function of current (I) into as function of carrier density (N). Knowledge of the I(N) relationship is the bridge that connects the experimental data and theoretical simulation. We achieve this by measuring the gain spectra g(E, I), as shown in Figure 5.3, fitting it with the analytical gain model g(E, N) described in chapter 3 and extracting relationship I(N), as shown in Figure 5.9.

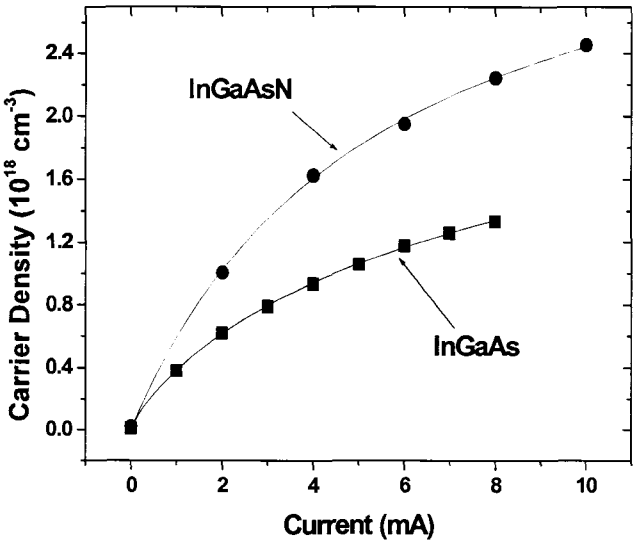

Figure 5. 9 Carrier density and current relation, N(I), for both InGaAsN and InGaAs QW lasers at room temperature.

The decay time as function of carrier densities is obtained and plotted in Figure 5.12. We first approach the simulation by treating the carrier escape process only as classical thermionic emission and considering state filling. In this case the functional dependence of thermal escape time τ_{therm} can be calculated using the following analytical equation[25][27]:

$$\tau_{therm\_e}(N) = \omega \frac{L_{qw}}{m_{e\_b}} \left(\frac{\pi\hbar^2 m_{e\_w}}{m_{e\_b} k_B T}\right)^{\frac{1}{2}} \frac{\exp\left(\frac{qV_e}{k_B T}\right)}{1+\exp\left(\frac{E_{fc}(N) - E_{e\_1}}{k_B T}\right)} \tag{5.15}$$

$$\tau_{therm\_hh}(N) = \omega \frac{L_{qw}}{m_{hh\_b}} \left(\frac{\pi\hbar^2 m_{hh\_w}}{m_{hh\_b} k_B T}\right)^{\frac{1}{2}} \frac{\exp\left(\frac{qV_{hh}}{k_B T}\right)}{1+\exp\left(\frac{E_{fv}(N) - E_{hh\_1}}{k_B T}\right)} \tag{5.16}$$

$$\frac{1}{\tau_{therm}(N)} = \frac{1}{\tau_{therm\_e}(N)} + \frac{1}{\tau_{therm\_hh}(N)} \tag{5.17}$$

In Eqs. (5.15) - (5.16), ω is a constant related to the escape rate from inside the well to the unconfined state in the barrier, in unit of $m^{-1} \cdot kg \cdot eV^{-1/2}$. We assume ω is the same for InGaAs and InGaAsN. L_{qw} is the width of the QW, m_{e_w} (m_{hh_w}) is the effective electron (heavy hole) mass in the well and m_{e_b} (m_{hh_b}) the electron (hole) mass of the barrier. qV_e and qV_{hh} are the energy difference between the first confined electron (heavy hole) state and the edge of barrier conduction and valence band, respectively. $E_{fc}(N)$ ($E_{fv}(N)$) is the electron (hole)

quasi-Fermi level for confined carriers, and $E_{e\_1}(E_{hh\_1})$ is the energy of the first confined level. For more than one confined energy level, the escape time is replaced by a summation over all energy levels involved. For the carrier densities of our interest (< 3×10^{18} cm^{-3}), the quasi-Fermi level is far below the second confined level for both electron and holes, thus the corresponding exponential term in the denominator is much less than 1 and hence it is ignored. Table 5.3 summarizes all the parameters used in this work.

Table 5. 3 Parameters for the calculation of carrier thermionic escape time.

	$In_{0.4}Ga_{0.6}As_{0.995}N_{0.005}/GaAs$	$In_{0.4}Ga_{0.6}As/GaAs$
Well depth Conduction band	431 meV	251 meV
Well depth Valence band	95 meV	177 meV
qV_e	360 meV	177 meV
qV_{hh}	85.6meV	163.5 meV
m_{e_w}	0.11 m_0	0.047 m_0
m_{e_b}	0.067 m_0	0.067 m_0
m_{hh_w}	0.465 m_0	0.465 m_0
m_{hh_b}	0.51 m_0	0.51 m_0

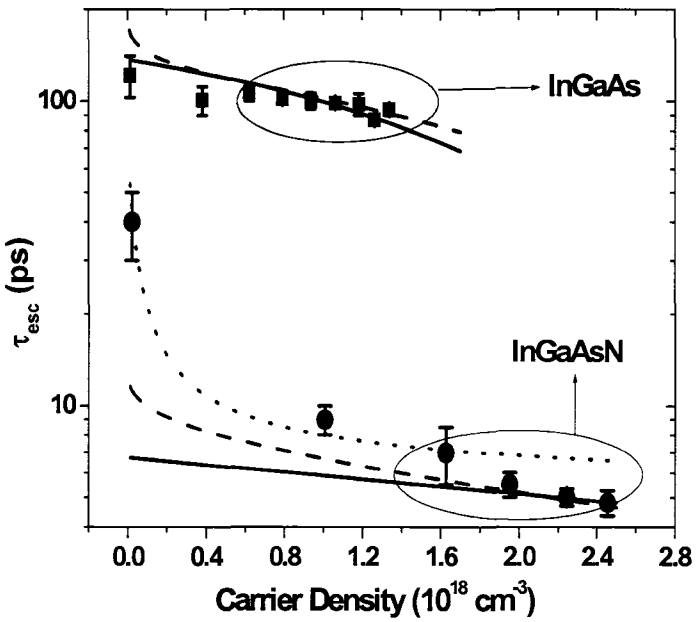

Figure 5.10 Experimental (points) and calculated carrier escape time as function of carrier density at room temperature. (free carrier case: solid lines; exciton: dashed lines, tunneling effect: dot line, InGaAsN only)

The calculation results of τ_{esc} are also plotted in Figure 5.10 together with the experimental measurements. The solid lines are the results for free carrier thermionic escape, where the differences between InGaAs and InGaAsN lasers in the calculation is only due to the electron effective mass and band offset ratio. The value of $\omega = 2.1\times10^{-21}$ $m^{-1}kg\,eV^{-1/2}$ is chosen for both materials. The escape time one order of magnitude less is obtained for InGaAsN, showing good agreement with other theoretical calculation on the same laser structures in other literatures [11]. Notice that while the calculation gives similar values of the

escape time due to free carriers at higher carrier density, the functional trend does not match experiments at low carrier density, especially for InGaAsN. On the contrary, InGaAs shows a good agreement between the thermionic calculation and the experimental results. We next considered the existence of excitons [28]. In this case, the expression of the quasi-Fermi level for heavy holes does not follow Fermi-Dirac statistics, but in stead follows the electron distribution and therefore increase the band filling effect of hole state, the escape time calculation is modified. The inclusion of exciton effect in InGaAsN lasers (dashed line in Figure 5.12) show a closer trend but not sufficient to explain the increase of τ_{esc} at low carrier density. In both free carrier and exciton cases, we take the same band offset ratio (81.9%), but $\omega = 5\times10^{-21}$ $m^{-1}\cdot kg\cdot eV^{-1/2}$ is adopted in the exciton calculation instead to get a good agreement at high carrier density.

The discrepancy between the measurements of τ_{esc} for InGaAsN laser and the results from the thermionic simulation indicates that there are other mechanisms dominant the carrier escape at low carrier density [29,30]. One such process is tunneling. Actually from the carrier tunneling rate expressions in Eq (5.18) and (5.19) [31], we see that carrier escape due to tunneling has a stronger dependence on carrier density, which shows a faster decay rate with increased carrier density (index of 3/2 in exponential term) would be expected, compared to the thermionic model of index of 1 for electrons and holes.

$$\tau_{tun\_e}(N) \sim \exp\left(\frac{4}{3}\frac{\sqrt{2m_e^*}}{e\hbar F(N)}(V_e - (E_{fc}(N) - E_{e\_1}))^{3/2}\right) \qquad (5.18)$$

$$\tau_{tun\_hh}(N) \sim \exp\left(\frac{4}{3}\frac{\sqrt{2m_{hh}^{*}}}{e\hbar F(N)}(V_e - (E_{fv}(N) - E_{hh\_1}))^{3/2}\right) \qquad (5.19)$$

In the above expressions, F(N) is the build-in field resulting from the biasing, which contributes to the decrease of escape time with carrier density. Assuming the impedance of the laser diode does not change with bias, the build-in field is proportional to the biasing current. Making use of the I(N) relationship obtained in Figure 5.9, the expression of F(N) can be obtained with an constant factor denoting the impedance.

The dotted line in Figure 5.10 is the simulation result only considering tunneling in the InGaAsN laser. All the parameters used in the fitting are the same as those in Table 5.3. The agreement at lower carrier density side is remarkable and explains the steep decay of τ_{esp} clearly showing the dominance of carrier escape through tunneling out of the well at that regime. As carrier density increases, both thermionic escape and tunneling become equally important.

Generally, it is not just the value of escape time but the ratio of capture and escape time constant ($R=\tau_{cap}/\tau_{esc}$) that determines the modulation response. Here the τ_{cap} is the sum of quantum capture time τ_{cap_qw} and the transport time from the edge of barrier to the QW, τ_{tr}. The risetime in our pump-probe data indicates the quantum capture time, τ_{cap_qw} is less than 1 ps for both InGaAsN and InGaAs QWs. While τ_{tr} was calculated by Yeh et al. [32] and found to be constant ~5.3ps in both InGaAsN and InGaAs lasers, we also determined the transport time to be ~10 ps from time resolved PL rise time. Thus we conclude that transport time is

dominant contribution to τ_{cap} in both lasers and that the introduction of nitrogen does not affect τ_{cap} significantly. This finding is consistent with general knowledge on QW lasers. In Figure 5.13, the ratio of capture and escape time constant $R=\tau_{cap}/\tau_{esc}$ versus N is plotted, where τ_{cap}= 5.3 ps [32] is utilized in the calculation. A result in the increase of R with carrier density N is significantly stronger than in the case of InGaAs. This result, to our best knowledge, is the first time measurement results for τ_{esc} and ratio R. Note that under pulsed pump-probe condition, R is appropriately defined as dynamic ac ratio, which is intrinsic in studying small signal analysis of laser response.

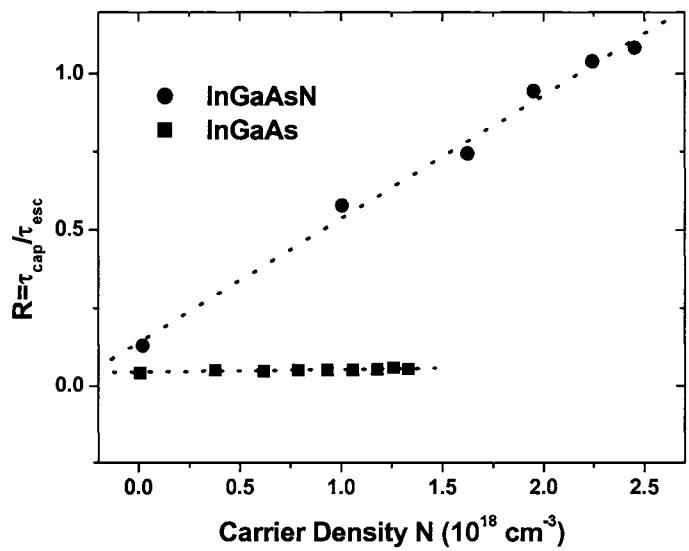

Figure 5. 11 Ratio of capture and escape time constant $R=\tau_{cap}/\tau_{esc}$ as function of carrier density N for InGaAs (circle) and InGaAsN (square) RWG lasers

5.5 Conclusion

In summary, an extensive study of the nonlinear gain dynamics and carrier capture and escape are discussed in this chapter. Through single color pump-probe experiments, carrier heating, two photon absorption (TPA) are found to be the two main factors contributing processes to the gain compression. In InGaAsN laser carrier heating has more significant effect on gain compression in the gain regime. The relaxation time constant associated with carrier heating in both InGaAs and InGaAsN lasers have similar values, 2-3 ps. These measurements are of significant importance considering their application of high-speed laser modulation.

We have also independably measured carrier escape times τ_{esc}, which are about an order of magnitude smaller in InGaAsN than in InGaAs laser diodes. We show that the dependence of τ_{esc} on carrier density in dilute nitrides is only explained if tunneling through the triangular biased quantum well is considered. This mechanism is most important at low carrier densities Provided smaller band offset ratio, InGaAs laser can be well explained only with thermionic model.. Exciton effects are also proven to be important in affecting the escape time. Together with time-resolved photoluminescence measurements, ratio of τ_{cap}/τ_{esc} of InGaAsN laser device is found to be significantly carrier density dependent in contrast to InGaAs.

Reference:

[1]. Y.Arakawa and T. Takahashi, "Effect of nonlinear gain on modulation dynamics in quantum well lasers," ELECTRONICS LETTERS, **25**: 169-170 (1989).

[2]. M. C. Tatham, I. F. Lealman, Colin P. Seltzer, L. D. Westbrook,and D. M. Cooper, "Resonance frequency, damping, and differential gain in 1.5 μm multiple quantum-well lasers," IEEE JOURNAL OF QUANTUM ELECTRONICS **28**: 408-414 (1992).

[3]. L.A.Coldren and S.W.Corzine, *Diode lasers and Photonic Integrated Circuits*: Wiley series in microwave and optical engineering, 1995

[4]. O. Anton, L.F. Xu, D. Patel, J. Y. Yeh, T. T. Van Roy, L.J. Mawst and N. Tansu, "The intrinsic frequency response of SQW-MOCVD 1.3μm InGaAsN lasers in the range T=10-80°C", IEEE PHOTONICS TECHNOLOGY LETTERS **18** (13-16): 1774-1776 (2006).

[5]. A.Thranhardt , S. Becker, C. Schlichenmaier, I. Kuznetsova, T. Meier, S.W. Koch, J. Hader, J.V. Moloney and W.W. Chow, "Nonequilibrium gain in optically pumped GaInNAs laser structures", APPLIED PHYSICS LETTERS **85** (23): 5526-5528 (2004).

[6]. N. Laurand, S. Calvez, M.D. Dawson and A.E. Kelly, "Index and gain dynamics of optically pumped GaInNAs vertical-cavity semiconductor optical amplifiers", APPLIED PHYSICS LETTERS **87** (23): Art. No. 231115 (2005).

[7]. Y.Q. Wei, J.S. Gustavsson, M. Sadeghi, S.M. Wang and A. Larsson, "Dynamics and temperature-dependence of 1.3-μm GaInNAs double quantum-well lasers", IEEE JOURNAL OF QUANTUM ELECTRONICS **42** (11-12): 1274-1280 (2006).

[8]. M.P. Kesler and E. P.Ippen , "Subpicosecond gain dynamics in GaAlAs laser-diodes", APPLIED PHYSICS LETTERS **51** (22): 1765-1767 (1987).

[9]. K.L.Hall, G.Lenz, E.P.Ippen and G.Raybon "Heterodyne pump probe technique for time-domain studies of optical nonlinearities in wave-guides", OPTICS LETTERS **17** (12): 874-876 JUN 15 (1992).

[10]. C.K.Sun, H.K.Choi, C.A.Wang, J.G.Fujimoto, " Studies of carrier heating in InGaAs/AlGaAs strained-layer quantum-well diode-lasers using a multiple wavelength pump probe technique", APPLIED PHYSICS LETTERS 62 (7): 747-749 FEB 15 (1993).

[11]. N. Tansu, L. J. Mawst, "The role of hole leakage in 1300-nm InGaAsN quantum-well lasers", APPLIED PHYSICS LETTERS **82** (10): 1500-1502 MAR (2003).

[12]. R.W. Schoenlein, W.Z. Lin, E.P. Ippen and J.G. Fujimoto, " Femtosecond hot-carrier energy relaxation in GaAs", APPLIED PHYSICS LETTERS **51**: 1442-1444 (1987).

[13]. F.R. Laughton, J.H. March and J.S. Robert, "Intuitive model to include the effect of free-carrier absorption in calculating the two-photon absorption coefficient," APPLIED PHYSICS LETTERS **60**: 166-168 (1992).

[14]. S.S. Kubakaddi and B.G. Mulimani, "Free carrier absorption in semiconducting quantum-well sires for nonpolar optical-phonon scattering," JOURNAL OF APPLIED PHYSICS **63**: 1799 (1988).

[15]. J.H. Bechtel and W.L. Smith, "Two-photon absorption in semiconductors with picosecond laser pulses", PHYSICAL REVIEW B **13**: 3515 (1979).

[16]. W.Z. Lin, R.W. Schoenlein, J.G. Fujimoto and E.P. Ippen, "Femtosecond absorption saturation studies of hot carriers in GaAs and AlGaAs", IEEE JOURNAL OF QUANTUM ELECTRONICS **24**: 267 (1988).

[17]. B.W. Hakki and T.L. Paoli, " Gain spectra in GaAs double heterostructure injection lasers", JOURNAL OF APPLIED PHYSICS **46** (3): 1299-1306 (1975).

[18]. K.L. Hall, Y. Lai, E.P. Ippen, G. Eisenstein, and U. Koren, "Femtosecond gain dynamics and saturation behavior in InGaAsP multiple Quantum-Well optical amplifier," APPLIED PHYSICS LETTERS **57** (27): 2888-2890 (1990).

[19]. D. Gollub, S. Moses, and A. Forchel, "1.3 μm double quantum well GaInNAs distributed feedback laser diode with 13.8 GHz small signal modulation bandwidth", ELECTRONICS LETTERS **40** (19): 1181-1182 (2004).

[20]. J.S. Gustavsson, Y.Q. Wei, M. Sadeghi, S.M. Wang, and A. Larsson, "10 Gbit/s modulation of 1.3 μm GaInNAs lasers up to 110 degrees C", ELECTRONICS LETTERS **42** (16): 925-926 (2006).

[21]. W. Shan, W. Walukiewicz , J.W. Ager, E.E. Haller , J.F. Geisz , D.J.Friedman, J.M. Olson, S.R. Kurtz , "Band anticrossing in GaInNAs alloys", PHYSICAL REVIEW LETTERS **82** (6): 1221-1224 (1999).

[22]. J. C. L. Yong, J. M. Rorison, M. Othman, H. D. Sun, M. D. Dawson, and K. A. Williams, "Simulation of gain and modulation bandwidths of 1300nm RWG InGaAsN lasers," IEE Proceedings-Optoelectronics, **150** : 80-82 (2003).

[23]. S.C.Kan, D. Vassilovski, T. C. Wu, K.Y. Lau , "Quantum capture and escape in quantum-well lasers – implications on direct modulation bandwidth limitation", IEEE PHOTONICS TECHNOLOGY LETTERS **4** (5): 428-431 (1992).

[24]. R. Nagarajan, M. Ishikawa, T. Fukushima, R. S. Geels, J.E. Bowers, " High speed quantum-well lasers and carrier transport effects", IEEE JOURNAL OF QUANTUM ELECTRONICS **28** (10): 1990-2008 (1992).

[25]. B. Romero, J. Arias, I. Esquivias, and M. Cada, "Simple model for calculating the ratio of the carrier capture and escape times in quantum-well lasers", APPLIED PHYSICS LETTERS **76** (12): 1504-1506 (2000).

[26]. J.Feldmann, K.W. Goossen, D.A.B. Miller, A.M. Fox, J.E. Cunningham and W.Y. Jan, "Fast escape of photocreated carriers out of shallow quantum-wells", APPLIED PHYSICS LETTERS 59 (1): 66-68 (1991).

[27]. H. Schneider, K. Vonklitzing, *Physical Review B* **38** (9): 6160-6165 (1988).

[28]. L. F. Xu, D. Patel and C.S.Menoni, J.Y. Yeh, L. J. Mawst, Nelson Tansu, *Applied Physics Letters* 89 (17): Art. No. 171112 OCT 23 (2006).

[29]. M. Grupen and K. Hess, *IEEE Journal of Quantum Electronics* 34 : 120 (1998).

[30]. C. Y. Tsai, Y. H. Lo, R. M. Spencer, and L. F. Eastman, *IEEE Journal of Selected Toptics in Quantum Electronics* **1**: 316 (1995).

[31]. G. Vincent, A. Chantre, and D. Bois, "Electric-field effect on the thermal emission of traps in semiconductor junctions" JOURNAL OF APPLIED PHYSICS **50** (8): 5484-5487 (1979)

[32]. J. Y. Yeh and L. J. Mawst, "Modelling of thermionic processes in 1.3μm InGaAsN/GaAsP/GaAs SQW laser heterostructures," University of Wisconsin, Madison 2004.

CHAPTER 6

Conclusions and future work

The main goal of this dissertation was to study the fundamental optical material properties of InGaAsN/GaAs quantum wells, specifically high indium content strain compensated dilute nitride laser diodes. We have investigated the carrier recombination dynamics, nonlinear gain dynamics and carrier capture and escape process of this novel material, which are relevant in understanding the effect of incorporation of nitrogen on both material quality and high-speed device performance. After these comprehensive studies, we have been able to answer the following questions: What processes affects the optical quality of InGaAsN QWs? What is the fundamental value of electron effective mass m_e^* and how the change of m_e^* after incorporation of nitrogen influences the performance of laser diodes? What is the carrier dynamics behavior, specifically nonlinear carrier heating and its relaxation, carrier capture into and escape out of the well and how these processes affect the nonlinear gain dynamics?

An analytical model based on the assumption of parabolic E-k dispersion relationship was built to provide guidelines on main modifications of the electronic structure of InGaAsN/GaAsP/GaAs quantum wells of high indium content. The model had been tested against the k*p simulation. The intrinsic differential gain dG/dN, transparency carrier density N_{tr} for both nitrogen and nitrogen free QW are retrieved through the analysis of the results from the model. The introduction of nitrogen into InGaAs leads to an increase of the transparency carrier density, $N_{tr,}$ by about 40%, and we ascribe this behavior to the enhancement of the electron effective mass m_e^*. While a

25% decrease in the material differential, dG/dN, is obtained from our model. This decrease is mainly accounted for the decrease in the momentum matrix element as the effect of m_e* increase on the quasi-Fermi level leads to a 30% enhancement in dG/dN in the InGaAsN/GaAs QW. This result differs from most predictions of current theoretical model based on k*p. Therefore, further efforts in the k*p theoretical modelings are needed. The analysis based on the gain model also allowed us to study and predict different aspects of InGaAsN material and the laser performance, such as excitonic and carrier heating effects. The former effects shows a positive effect on gain and differential gain, while the latter, compresses the gain.

The experiments comprise a comprehensive study of the spectrally and temporarily resolved photoluminescence (PL) in the temperature range of 10-300 K. The analysis of the results provides insight on carrier localization effects, the nature of the electron and hole states that participates in the emission and their recombination dynamics. It was found through the analysis of the photoluminescence (PL) spectrum obtained for high excitation conditions that two transitions compete at the early stages of carrier recombination. These two transitions are identified as the first quantized electron state to heavy-hole state (e1-hh1) and electron to light-hole state (e1-lh1) from the analysis of polarized photocurrent measurements. This discovery is different from negativity offset of light hole state predicted in k*p simulation. At longer time delays, the dilute nitride QWs exhibit carrier localization followed by nonradiative recombination. The former only exists at low temperature (T<100K) and exhibits a rather long lifetime. Instead, at higher temperatures, the lifetime decreases with temperature and the luminescence efficiency significantly deteriorates. This behavior contrasts with that of

the host InGaAs. The analysis of the photoluminescence spectra at temperatures above those where localization occurs allowed determining the exciton binding energy. This analysis coupled with a 2-D model enables the determination of the electron effective mass, m_e^*. This approach yielded $m_e^*=(0.049\pm0.007)m_0$ and $m_e^*=(0.11\pm0.015)m_0$ for InGaAs and InGaAsN. The excellent agreement obtained in me* for InGaAs verifies the validity of our approach, which in turn is more accurate as it is less sensitive to variations in the band offset ratio.

The nonlinear gain dynamics and carrier capture and escape processes of ridge waveguide (RWG) laser devices were also investigated. Through single color pump-probe experiments, carrier heating, and two photon absorption (TPA) are found to be the two main contributing processes to the gain compression. In InGaAsN lasers the amplitude of the carrier heating process is significantly larger than in InGaAs and has a more significant effect on gain compression in the gain regime. The relaxation time constant associated with carrier heating in both InGaAs and InGaAsN lasers have similar values, 2-3 ps. These measurements are of significant importance considering their application of high-speed laser modulation.

We have also independably measured the carrier escape time, τ_{esc}, which is about an order of magnitude smaller in InGaAsN than in InGaAs. We show that the dependence of τ_{esc} on carrier density in dilute nitrides is only explained if tunneling through the triangular biased quantum well is considered. This mechanism is most important at low carrier densities. Exciton effects are also proven to be important in affecting the escape time. Together with time-resolved photoluminescence measurements, the carrier transport is found to be dominant over the carrier capture process and no significant change has

been found for both InGaAs and InGaAsN lasers. This result is, to our best knowledge, the first time measurement of τ_{esc} on InGaAs(N) devices.

Through the study of carrier capture and escape dynamics, we discovered an increase of hole escape rate that can lead to reduction of the effective differential gain and cause a rapid increase of the threshold current. This aspect was found to be determined by the band line up, that is, a small valence band offset due to incorporation of nitrogen. Therefore, future work on this high indium content strain compensated dilute nitride lasers may require careful adjustment of the band structure, either by using super-lattice barriers or managing the strain to realize a better hole confinement.

APPENDIX

Analytical Gain Model

Analytical Gain Model

Unit of gain is cm^-1

Active region In0.4Ga0.6As0.995N0.005, Width 60A, so it's a QW.

parameters (right now don't consider the carrier affect on index of refraction, don't consider the effect of temperature on electron effective mass, but consider the effect of temperature on momentum matrix):
Don't consider valence band mixing

The composition of InxGa1-xAs1-yNy is x=0.4 y=0.005

Plank constant

$$h := 4.41 \cdot 10^{-15} \ ev \cdot s$$

Electron mass

$$m0 := 9.1095 \cdot 10^{-31} \ kg$$

Permitivity in vacuum

$$\varepsilon 0 := 8.8542 \cdot 10^{-12} \ \frac{F}{m}$$

Speed of light

$$c := 3 \cdot 10^{8} \ \frac{m}{s}$$

Index of refraction

$$ng := 3.69$$

β=1/kT, at room temperature T=300K β=1/25.8537meV

$$\beta(T) := \frac{1000}{25.8537} \cdot \frac{300}{T}$$

Free Electron charge

$$ee := 1.6 \cdot 10^{-19} \ C$$

spin off split energy

$$\Lambda := 0.356 \ ev$$

$$Lz := 6 \ nm$$

Effective dimension(see exciton binding energy caculation)

$$\alpha := 2.248$$

carrier induced band-gap shrinkage coefficient

$$\zeta := 0.97 \cdot 10^{-8} \ ev \cdot cm$$

Band gap vs Temperature obeys Varshni's equation

$$Eg(T) := 0.9409 - \frac{0.00047 \cdot T^2}{T + 253.72404} \qquad Eg(300) = 0.865 \text{ ev}$$

$$Ech(T) := 1.0279 - \frac{0.00047 \cdot T^2}{T + 253.72404} \qquad Ech(283) = 0.958 \text{ ev}$$

$$Eel(T) := (Ech(T) - Eg(T)) \cdot 0.8 \qquad Eel(300) = 0.07 \text{ ev}$$

$$Ehl(T) := (Ech(T) - Eg(T)) \cdot 0.2 \qquad Ehl(300) = 0.017 \text{ ev}$$

Half of the Band width

$$\gamma k := 9 \cdot 10^{-3} \text{ ev}$$

Effective Electron mass based on BAC model

$$me := 0.083 \cdot m0$$

Heavy hole mass

$$mhh := 0.465 \cdot m0$$

reduced effective mass

$$mr := \frac{1}{\frac{1}{me} + \frac{1}{mhh}}$$

The Ep for TE polarization, heavy hole of QW

$$Ep(T) := \frac{3}{2} \cdot \left(\frac{m0}{me} - 1\right) \cdot \frac{Eg(T) \cdot (Eg(T) + \Delta)}{\left(Eg(T) + \frac{2}{3} \cdot \Delta\right)}$$

Momentum Matrix element in QW

$$costheda(k,T) := \frac{Eel(T) + Ehl(T)}{Eel(T) + Ehl(T) + \frac{\left(\frac{h \cdot k}{2 \cdot \pi}\right)^2}{2 \cdot mr} \cdot 1.6 \cdot 10^{-19}}$$

$$M11(T,k) := \frac{3}{4} \cdot (1 + costheda(k,T)) \cdot \frac{m0}{6} \cdot Ep(T)$$

For QW active region, assuming that only the first level in QW is filled, the chemical potential is a function of carrier density and the relation is:

$$Fc(T,n) := Ech(T) + \frac{1}{\beta(T)} \cdot \ln\left[e^{\frac{\pi\cdot\left(\frac{h}{2\cdot\pi}\right)^2\cdot Lz\cdot\beta(T)\cdot\left(1.6\cdot10^{-22}\right)}{me}\cdot n} - 1\right]$$

$Ech(323) = 0.943$

$$Fv(T,n) := \frac{-1}{\beta(T)} \cdot \ln\left[e^{\frac{\pi\cdot\left(\frac{h}{2\cdot\pi}\right)^2\cdot Lz\cdot\beta(T)\cdot\left(1.6\cdot10^{-22}\right)}{mhh}\cdot n} - 1\right]$$

Seperation of Fermi level

$$\Delta\mu(T,n) := Fc(T,n) - Fv(T,n)$$

$Fc\left(310, 3.095\cdot 10^{18}\right) = 1.006$ ev

$Fv\left(310, 10^{18}\cdot 3.095\right) = 0.018$ ev

Energy seperation not taking into account the nonparabolicity

$$Ecv(T,n,k) := Ech(T) + \left[\frac{\left(\frac{h\cdot k}{2\cdot\pi}\right)^2}{2\cdot me} + \frac{\left(\frac{h\cdot k}{2\cdot\pi}\right)^2}{2\cdot mhh}\right]\cdot\left(1.6\cdot 10^{-19}\right)$$

$Ech(323) = 0.943$

$$E11(T,n) := Ech(T) - \zeta\cdot(n)^{\frac{1}{3}}$$

CONSIDER HEAVY HOLE ONLY

$$k1(E,T) := \frac{\sqrt{\frac{2\cdot mn(T)\cdot(E - Ech(T))}{1.6\cdot 10^{-19}}}}{\frac{h}{2\cdot\pi}}$$

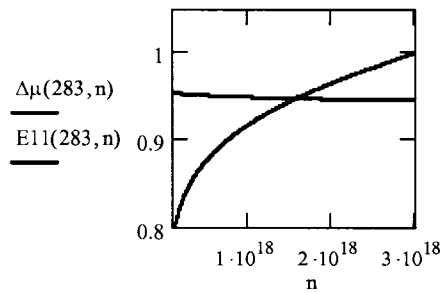

$$fc(T,n,k) := \frac{1}{1 + e^{\frac{Ech(T) + \frac{\left(\frac{h}{2\cdot\pi}\cdot k\right)^2\cdot 1.6\cdot10^{-19}}{2me} - Fc(T,n)}{\frac{1}{\beta(T)}}}}$$

$$fv(T,n,k) := \frac{1}{1 + e^{\frac{-\frac{\left(\frac{h}{2\cdot\pi}\cdot k\right)^2\cdot 1.6\cdot10^{-19}}{2\cdot mhh} - Fv(T,n)}{\frac{1}{\beta(T)}}}}$$

Expression for Gain of QW structure:

$$C0(E) := \frac{\pi \cdot ee^2 \cdot \frac{h}{2 \cdot \pi}}{ng \cdot c \cdot \varepsilon 0 \cdot m0^2 \cdot E}$$

$$g(T,n,E) := C0(E) \cdot 10^7 \cdot \frac{2}{Lz} \cdot \int_0^{5 \cdot 10^8} M11(T,k) \cdot \frac{\frac{\gamma k}{\pi}}{(Ecv(T,n,k) - E)^2 + \gamma k^2} \cdot (fc(T,n,k) - fv(T,n,k)) \cdot \frac{k}{\pi \cdot 2}\, dk$$

$N := 500$

$i := 0..N$

Using range variable

$$E_i := 0.92 + (1 - 0.92) \cdot \frac{i}{N}$$

$E_i =$

	0
0	0.92
1	0.92
2	0.92
3	0.92
4	0.921
5	0.921
6	0.921
7	0.921
8	0.921
9	0.921
10	0.922
11	0.922
12	0.922
13	0.922
14	0.922
15	0.922

$g\left(300, 2.4 \cdot 10^{18}, E_i\right) \cdot 1 =$

	0
0	-93.872
1	-94.012
2	-94.151
3	-94.29
4	-94.428
5	-94.565
6	-94.701
7	-94.836
8	-94.97
9	-95.103
10	-95.236
11	-95.367
12	-95.497
13	-95.626
14	-95.753
15	-95.88

$g\left(310, 3 \cdot 10^{18}, x\right)$